Observations and Models of Accretion in Saturn's F Ring

by

Bonnie Kathleen Meinke

B.A., University of California, Berkeley, 2005

M.S., University of Colorado, Boulder, 2008

A thesis submitted to the

Faculty of the Graduate School of the

University of Colorado in partial fulfillment

of the requirement for the degree of

Doctor of Philosophy

Department of Astrophysical and Planetary Sciences

2012

This thesis entitled:
Observations and Models of Accretion in Saturn's F Ring
written by Bonnie Kathleen Meinke
has been approved for the Department of Astrophysical and Planetary Sciences

_____
Dr. Larry W. Esposito

_____
Dr. Philip J. Armitage

_____
Dr. Frances Bagenal

_____
Dr. Daniel Scheeres

_____
Dr. Glen Stewart

Date_____

The final copy of this thesis has been examined by the signatories, and we
Find that both the content and the form meet acceptable presentation standards
Of scholarly work in the above mentioned discipline.

Meinke, Bonnie Kathleen (Ph.D., Astrophysical and Planetary Sciences)

Observations and Models of Accretion in Saturn's F Ring

Thesis directed by Professor Larry W. Esposito

Abstract

Saturn's F ring is the solar system's principal natural laboratory for direct observation of accretion and disruption processes. Among the structures contained in its meager ~10 km radial width are jets, strands, and moonlets over an azimuthally asymmetric span. The nearby moons Prometheus and Pandora stir up ring material and create observably changing structures on timescales of days to decades.

In addition to the observations over the last three decades, the Cassini Ultraviolet Imaging Spectrograph (UVIS) has detected 27 statistically significant features in 101 occultations by Saturn's F ring since July 2004. Visual classification of the shapes of these 27 features divides the data set into three classes: Moonlet, Icicle, and Core. Two features are classified as Moonlets because each is opaque in its occultation, which makes them candidates for solid objects. A majority of features are classified as Icicles, which partially block stellar signal for 22 m to just over 3.7 km along the radial expanse of the occultation. The density enhancements responsible for such signal attenuations are likely due to transient clumping of material, evidence that aggregations of material are ubiquitous in the F ring. Our lengthy observing campaign reveals that Icicles are likely transient clumps, moonlets are possible solid objects, and cores show the variety of F ring morphology. We suggest that Icicles may evolve into Moonlets, which are an order of magnitude less abundant. The locations of the Icicles and Moonlets are weakly correlated to the location of Prometheus.

Motivated by the observations and previous models, I develop a more rigorous model of the evolution of aggregates in Saturn's F ring via tidally-modified accretion. For the first time, I assess the multimodal distribution resultant of collisional models and diagnose the cause. I apply the model to the F ring for constant body densities; then I assess how the system evolves when compaction is allowed. I develop an additional production term describing enhanced accretion of larger bodies in high-density regions produced by Prometheus, which results in the modeled distribution evolving to a state consistent with observations. Finally, I discuss the model's applicability to other astrophysical collisional systems.

Dedication

I dedicate this dissertation to my grandpa Bernard J. Mahony, Sr. and my high school German teacher Doris Hayes.

Acknowledgements

I would like to thank my advisor Larry Esposito for his guidance over the last 6.5 years. Without his help and motivation, I would not have successfully completed this dissertation. In addition, I would like to acknowledge the contributions of the Colorado rings group members, past and present: Glen Stewart, Josh Colwell, Keiji Ohtsuki, Miodrag Sremcevic, Nicole Albers, Dimitri Veras, and Tyler Mitchell. I learned so much from Friday group meetings, from rings dynamics to punny jokes.

Carl Murray, Josh Colwell, and Mike Evans provided thoughtful comments and reviews of the UVIS observations discussed in Section2 of this dissertation. Candice Hansen helped me develop my search algorithm and tweak it for the Enceladus plume. Glen Stewart worked closely with me to develop the production term discussed in Section 3. Nicole Albers provided much needed support and patient explanations of the coagulation equation and numerical modeling. I would like to thank these people for their contributions to this dissertation.

This entire dissertation was supported by the Cassini Project.

I would like to acknowledge the contributions of my graduate student peers to this work. Monica Hoke and Raina Gough provided a larger context for my work with useful comments on the Introduction. I would especially like to thank Adrienne Dove, Raina Gough, Eric Moore, Leigh Palmer, Evan Salim, and Sarah Walter for providing places for me to stay while in Boulder over the last year. I literally could not have finished this work without their generosity.

Special thanks to my family for supporting me. My parents Colleen and John Meinke cultivated a love of learning, allowed me to travel far and wide for higher education, and

Table of Contents

List of Tables

List of Figures

1. Introduction

Planetary rings are astrophysical disks in our own backyard. We have access to four in our Solar system, one of which is so easily observed it was first spotted in 1610 by Galileo with a simple 20-power telescope. Since that observation of Saturn's rings, both ground- and space-based observations have revealed varied and complex rings systems around Jupiter, Saturn, Uranus, and Neptune. Spacecraft, such as Voyager 1 and 2, Galileo, and Cassini missions, have traveled to these planets for close-up looks at their rings. Most notably the Cassini mission, as a dedicated mission to the Saturn system spanning over seven years, has compiled a large catalog of observations of the rings at multiple wavelengths, phase angles, and seasons. This opportunity to observe a system in real time has increased our understanding of the structural and compositional evolution of the ring system.

None of these systems exists independent of moons. These are, in fact, ring-moon systems. Moons play a very large role in the dynamics, structure, and evolution of a ring system. Moons like Enceladus in Saturn's E ring are the sources of ring material, while other moons constrain the orbits of ring particles from afar through resonances. Large, distant moons (e.g. Titan) and small, nearby moons (e.g. Pan) both can create ring structures. The interplay of rings and moons creates systems much more complex than Huygens would ever have guessed from his "solid disk" model of Saturn's rings.

Section 1 of this introduction reviews rings by system, both known and speculated. Section 2 discusses the ring-moon dynamics that build ring structures and new moonlets. In Section 3, I discuss the F ring as a laboratory for accretion processes and the ring moon interplay that leads to the creation and destruction of aggregates. Finally, in Section 4, I

discuss how studies of accretion and fragmentation in the F ring can shed light on processes in other astrophysical disks.

1.1 Rings by system

Each of the four giant outer planets in the Solar system hosts a ring-moon system. Galileo first discovered Saturn's broad, dense rings through his 20-power telescope in 1610 (Drake 1995). The rings of Jupiter, Uranus, and Neptune were not discovered until centuries later and are much different than Saturn's. In this section, I briefly review each system.

1.1.1 Jupiter

Jupiter hosts a ring system comprised of tenuous, dusty rings. It is the least massive of those in the Solar system (Burns, et al. 2004). Because it contains no dense component, it is also the only ring system discovered by spacecraft observations. The first indications of the system came from Pioneer 11 charged particle detectors (Fillius et al. 1975; Acuna and Ness 1976; Burns et al. 2004). Later, Voyager 1 images captured the Main ring (Owen et al. 1979), and Voyager 2 images allowed for a description of the system's structure (Showalter et al. 1987).
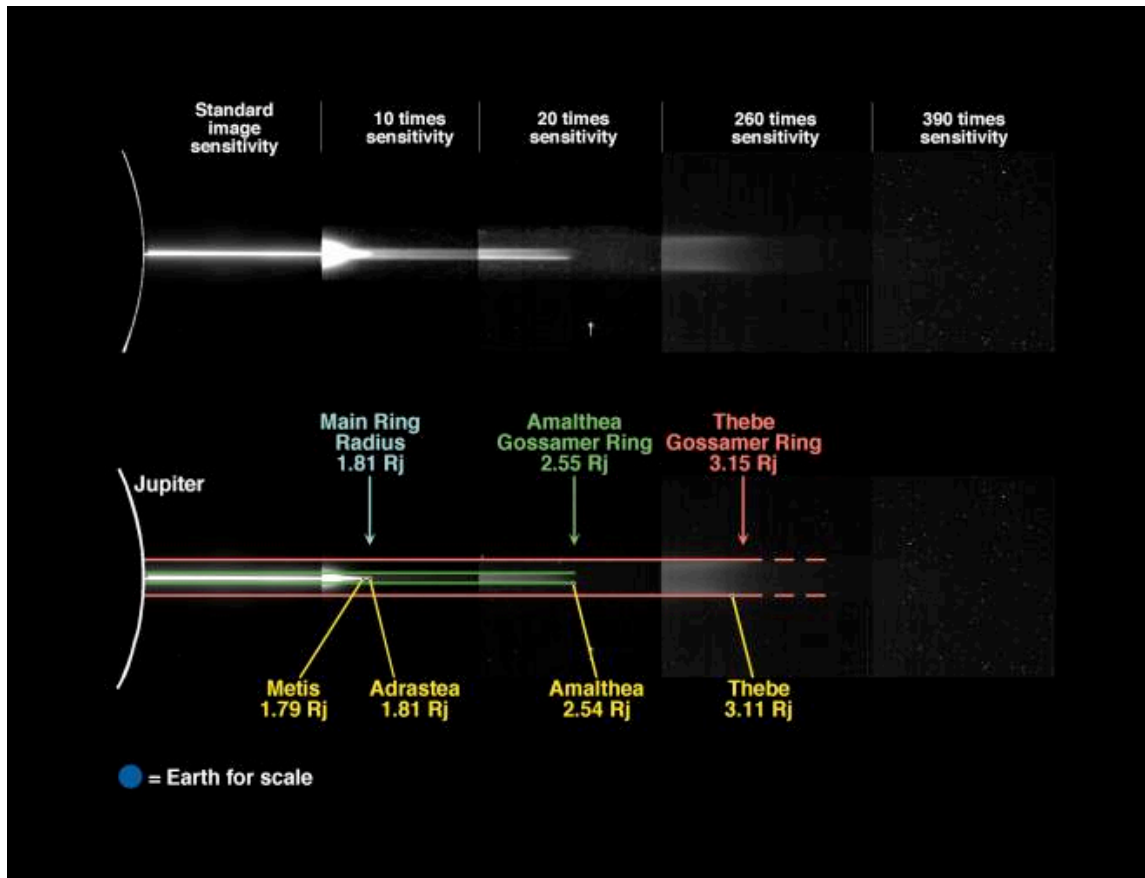
Figure 1. Image of Jupiter's rings with over laying schematic. Underlying image is near-edge-on Galileo mosaic of Jupiter's rings. Credit: http://photojournal.jpl.nasa.gov/catalog/PIA01623

There are four main components of the Jupiter ring system: the Halo ring, the Main ring, and two Gossamer rings. The Main and two Gossamer rings are centered on their embedded moons, which act as sources of ring material (Esposito 2002). Particles enter the rings by micrometeroid bombardment of those embedded moons (Burns, et al. 1999). The particles then spiral inward due to Poynting-Robertson drag. The Halo is a thick torus of material interior to the other rings. These rings have a significant vertical extent due to the source moons' vertical movement resulting from orbital inclination.

Because ring material moves inward, let's review the system this way as well. The two Gossamer rings are exterior to the Main ring and named for their source moons. The

inner ring is the Amalthea Gossamer ring; the outer is the Thebe Gossamer ring. The moon

Adrastea bounds the Main ring, which is relatively thin (6500 km), with an optical depth of

5.0×10^{-6} (Ockert-Bell 1999). Between the orbits of Metis and Adrastea exists a region of

cm-sized and larger particles rather than dust. This region appears bright at low phase

angles because it contains larger particles and is composed of several ringlets. Showalter,

et al. (2007) find no moons >0.5 km in this region in New Horizons images, but they do find

azimuthally-extended clumps in a ringlet interior to the orbit of Adrastea, which may be

related to Metis. Thus, the Main ring may be the remnant of a population of smaller moons

(Esposito 2002).

The Halo ring arises as material from the Main rain reaches the 3:2 Lorentz

resonance (Burns et al. 1985) between its orbital period and the rotation period of Jupiter's

magnetic field. Inward of this resonant location, the vertical extent of the ring increases to

over 1.2×10^4 km, although the radial extent of the torus is $\sim 3 \times 10^4$ km and much of the

material is in the central few hundred km thereof (Burns et al., 2004).

For the interested reader, Burns, et al. (2004) provides a comprehensive review of

the Jupiter ring system.

1.1.2 **Saturn**

Saturn hosts the most recognizable ring system. It is the most massive, most

diverse, and, until the last century, the only known ring system. The main part of the rings

consists of a broad, dense disk (Figure 2) composed of bright water ice divided into the A

and B rings by the Cassini Division (A exterior). The Cassini Division is not a gap, but a

region of lower surface density. The C and D ring are interior to the B ring, while the F, G, E,

4

and Phoebe rings are exterior to the A ring. Naming is a historical convention, not alphabetical by distance from the planet (Figure 2).
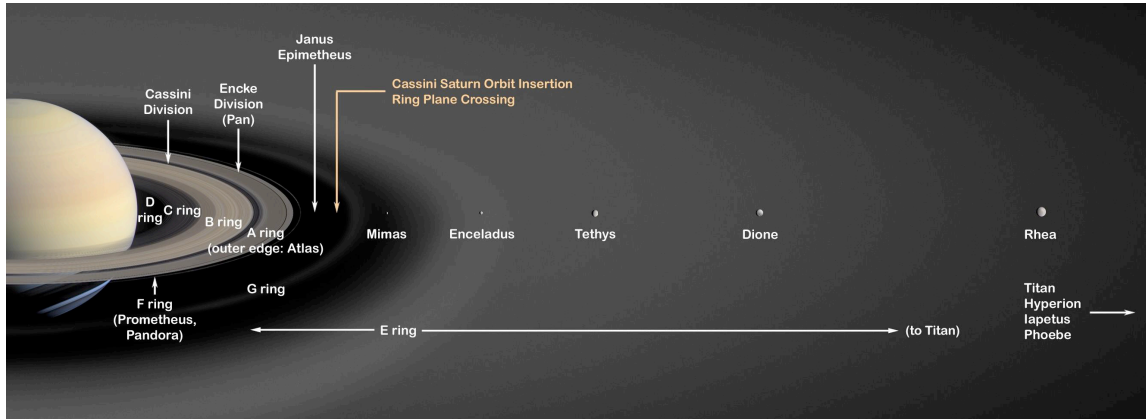
Figure 2. Image of Saturn's ring-moon system. Credit: NASA/JPL

Few true gaps exist in the system. There are some within the C ring and the Cassini Division and two (Encke and Keeler) in the outer A ring. All of them have sharp edges. The C ring's Colombo gap is held open by the Titan resonance. The two in the A ring are opened by moons in the gaps. The rest are not yet well explained, although some are speculated to be related to moon resonances (e.g. Mimas 2:1; Hedman et al. 2010a; Spitale and Porco 2010). I discuss these in more depth in Section 1.2.2. Many of these gaps contain ringlets, some diffuse and others sharply-constrained.

Saturn's rings include several dusty components, specifically the D, F, G, and E. The D, G, and E rings are diffuse dusty rings, but the F ring is dense and narrow (~10 km radial extent). These dusty rings share many properties with rings in other systems. The dedicated studies of these allow us to learn more about the varied rings around lesser-observed planets (Section 1.4)

The ongoing Cassini mission has provided a great wealth of new insight into rings. Several review articles are Cuzzi et al. (2010) and Esposito (2010). A comprehensive

review is available in five very specific parts: the rings' structure (Colwell et al. 2009b), dynamics (Schmidt et al. 2009), particle sizes and composition (Cuzzi et al. 2009), diffuse rings (Horanyi et al. 2009), and origins (Charnoz et al. 2009a).

1.1.3 **Uranus**

The definitive discovery of Uranus's rings was by Elliot, et al (1977). They discovered four inner rings, which they named with the first four lower case letters of the Greek alphabet (α, β, γ, δ). Later analysis led to the discovery of the ε ring, a dusty inner ring ζ, and rings 4, 5, and 6 (Millis et al. 1977). Voyager 2 images then revealed two new faint rings, η and λ (Smith et al. 1986). Using Hubble Space Telescope (HST) images, Showalter and Lissauer (2006) found two outer rings, which brings the total to 13 rings: 9 narrow main rings, 2 dusty rings, and 2 outer rings (Figure 3). All have azimuthal brightness variations. Unlike the relatively bright water-ice composition of the Saturnian ring system, the Uranian ring system is composed of dark (2% Bond albedo), dusty material (Ockert 1987, Karkoshka 1997).

Twelve small moons orbit exterior to the main rings, and Cordelia orbits just interior to the ε ring. The "Portia group" of eight moons orbits within an annulus from 59,100 to 76,500 km from Uranus' center. This group of moons is dynamically unstable on timescales of 10^6 to 10^8 years (Duncan and Lissauer 1997; Showalter and Lissauer 2006). Between two of these moons, Rosalind and Portia, is the dusty ν ring. This ring could be the debris from a recent catastrophic disruption of a moon or it could be the continual recycling of ring material, via competing accretion and fragmentation in the Roche zone, into small moonlets as proposed in Saturn's F ring (Section 3; Showalter and Lissauer

2006; French and Showalter 2011). Beyond the Portia group, the µ ring is centered on the

orbit of Mab (Showalter and Lissauer 2006).

A two-part comprehensive review of the Uranian ring-moon system discusses rings'

structure (French et al. 1991) and particle properties (Esposito et al. 1991).
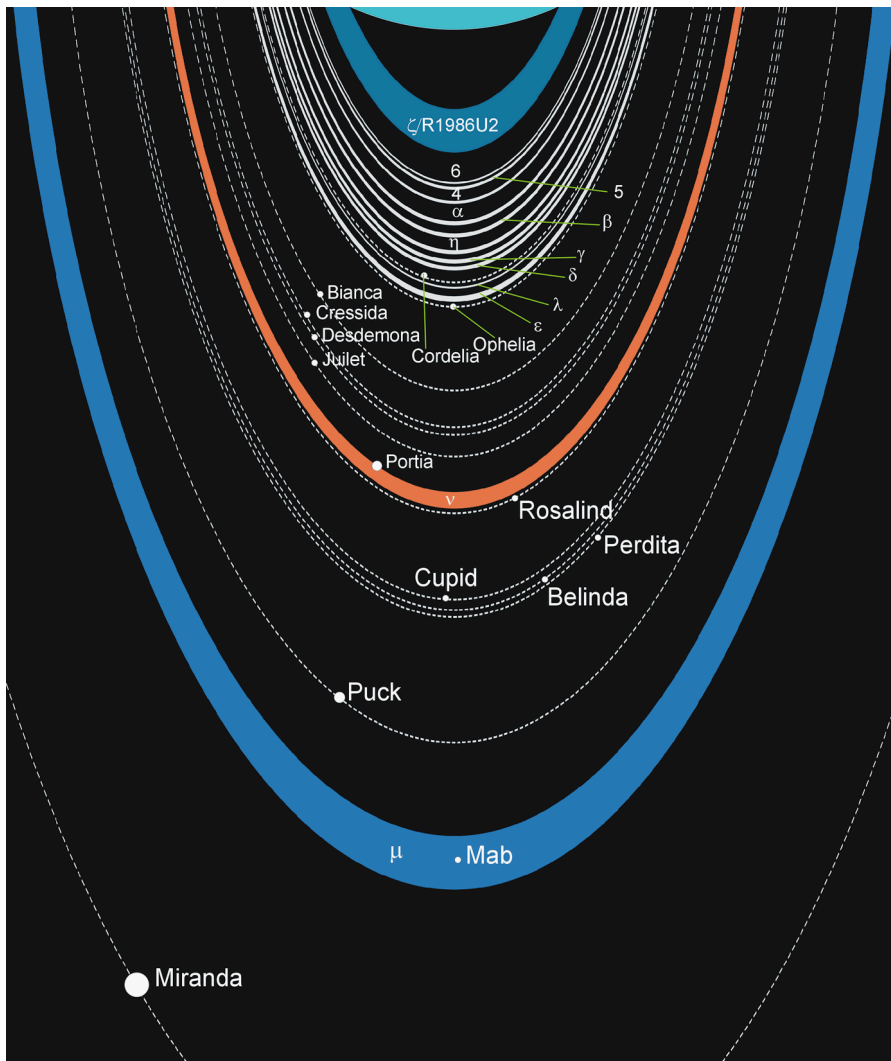
Figure 3. The scheme of Uranus's ring-moon system. Solid lines denote rings; dashed lines denote orbits of moons. Credit: Wikipedia

1.1.4 **Neptune**

Voyager 2 first imaged the rings of Neptune in 1989 (Miner et al 2007). These rings are

similar to those of Uranus. They are made of dark material, probably organics (Smith et al.,

1989), in the form of mostly micrometer-sized dust. However, the rings around Neptune are more diffuse and at larger semi-major axes than those of Uranus. Figure 4 displays the locations of the rings, which are named for the discoverers of Neptune. The Le Verrier, Arago, and Adams rings are narrow. The Galle and Lassell rings are tenuous dust sheets. The Adams ring contains a series of ring arcs, which were the first of their kind discovered.

Moons play a significant role in the Neptune system. The moons are interspersed between rings (Figure 4), causing interesting dynamics we do not observe in other systems, like the ring arcs. Galatea is an inner shepherd moon to the Adams ring (Porco 1991), like Prometheus is to Saturn's F ring. The ring arcs are the densest components of Neptune's ring system (with τ_{normal} =0.1). There are five arcs that extend over ~20° out of a ~40° span of longitude. The three main arcs were named for the French revolutionary slogan: Liberté, Egalité, and Fraternité. Then Egalité was divided in two upon closer inspection and a dimmer fourth arc was named Courage. Section 1.2 discusses formation mechanisms of ring arcs more in depth.

For the interested reader, Porco et al. (1995) give a comprehensive review of the Neptunian rings.
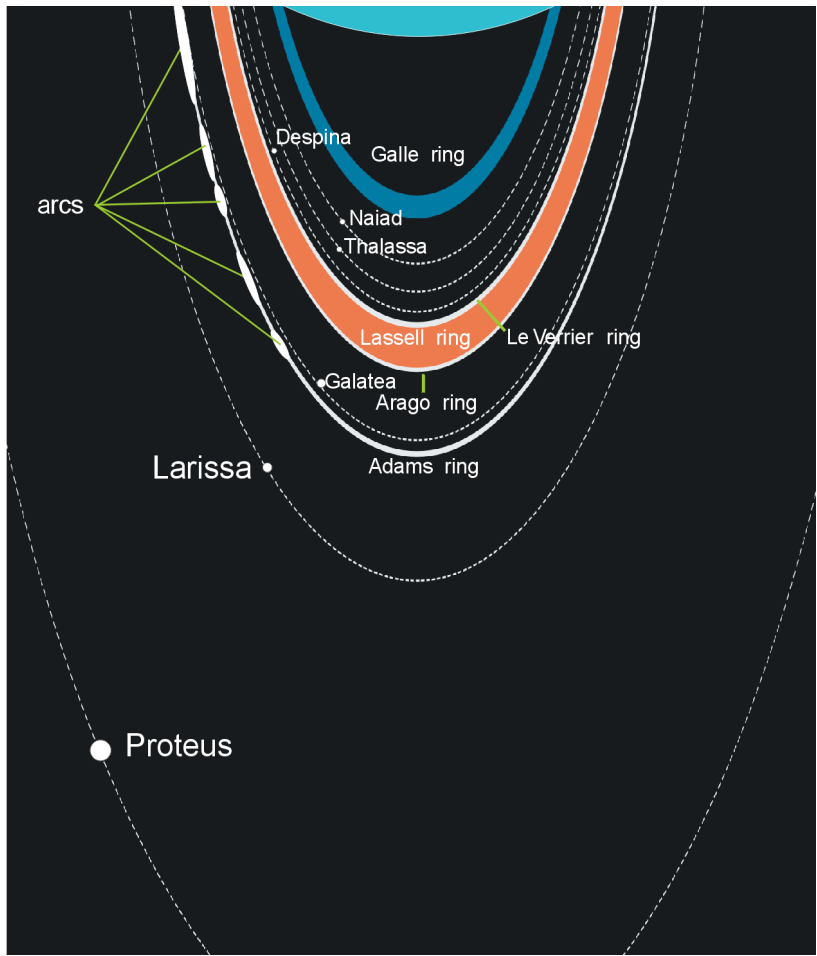
Figure 4. The scheme of Neptune's ring system. Solid lines denote rings; dashed lines denote orbits of moons. Credit: Wikipedia

1.2 **Ring dynamics that build clumping structures**

The rings host a variety of structures: embedded moons, self-gravity wakes, ring edges, arcs, and propellers. All of these structures are related to moons. A moon perturbs ring particle orbits to create a new structure, or those structures themselves create the conditions that allow aggregates to accrete.

1.2.1 **Roche Limit/Zone/Critical density**

The Roche limit is the distance from a planet within which the planet's tides can tear apart a body held together by its own self-gravity. Rings should arise interior to the Roche limit, while any disk of material outside the limit could be expected to accrete into a moon(s). The Roche limit is the location where tidal forces from a central mass (the difference in gravitational force on the near and far sides of a satellite) balance the self-gravity of the satellite. For a rigid, spherical body, Murray and Dermott (1999) (their Eq. 4.131) derive

$$a_{Roche} = \left(2\frac{\rho_p}{\rho_s} \right)^{1/3} R_p$$

Equation 1

where R_p is the radius of the central planet, ρ_s is the internal density of the satellite, and ρ_p is the internal density of the central planet. Thus, the Roche limit is not strictly one value, rather it is dependent on the internal density of the satellite. A denser, more compact object may exist closer to the central planet than a "fluffy" aggregate can. Internal strength of the satellite comes into play as well. Satellites held together by more than just self-gravity, like spacecraft, can orbit well inside the classical Roche limit.

In the context of planetary ring-moon systems, it is more useful to define a critical density rather than a critical orbital distance. At any given distance a from the central planet, the critical density ρ_{Roche} at which the moon's size entirely fills its "Roche lobe" or volume of gravitational dominance. I rearrange Equation 1 to obtain

$$\rho_{Roche} = \frac{2M_p}{\gamma a^3}$$

<div align="right">**Equation 2**</div>

where M_p is the mass of the central planet and $\gamma = 4\pi/3$ for a sphere and $\gamma \approx 1.6$ for an aggregate filling its Roche lobe (Porco, et al. 2007). If $\rho < \rho_{Roche}$, we can expect no bodies to coalesce and a ring to persist. Saturn's rings extend so far from the planet that ρ_{Roche} reaches values as low as ~0.4 g cm^{-3}, which is much lower than the density of solid water ice. In a region like the F ring, where accretion and disruption are in balance (c.f. Section 1.3), a low critical density indicates a high degree of porosity.

1.2.2 **Gap edges and moonlet wakes**

As discussed in Section 1.1.2, there are few truly empty gaps in Saturn's rings. Saturn's main rings contain 14 named gaps: 4 in the C ring, 8 in the Cassini Division, and 2 in the A ring. Some of the gaps in the C ring coincide with Lindblad resonances, others are unexplained, and the A ring gaps are opened by moons within them. This section focuses on the gaps containing moons.

The A ring gaps, Keeler and Encke, each contain a moon, Daphnis and Pan respectively, that exerts a torque on neighboring ring material, thus clearing and maintaining the gap. When a ring particle passes through conjunction with a nearby moon, the moon's gravity "kicks" the particle, which increases both the particle's eccentricity and

the separation in semi-major axis from the moon. On this new orbit, a ring particle interior to the moon will now orbit faster; likewise an outer particle will orbit slower. In the moon's reference frame, the particle's separation distance in one orbital period will be $3\pi\Delta a$. This is the characteristic length of gap moon phenomena. It is the wavelength of the wave structure that forms at the gap edges. Streamlines at the gap edge also have that wavelength; therefore, streamlines farther from the gap edge have larger Δa and larger wavelengths. In turn, the separations of the streamlines create a pattern called "moonlet wakes" (Figure 5). Thus, moonlet wakes are kinematic phenomena caused by a gap moon organizing the orbital properties of the ring material around it into streamlines. Because streamline spacing is related to surface density (higher densities where streamlines crowd), the wakes create a structure that enhances the local surface density encountered by individual ring particles on their individual orbits. The pattern speed of the moonlet wakes is equal to the orbital speed of the gap moon, while the individual ring particles maintain their individual orbital speeds and local dispersion velocity. Moonlet wakes are not restricted to gaps. Prometheus creates a similar phenomenon in Saturn's F ring (c.f. Section 2.6 and 3.1.5).
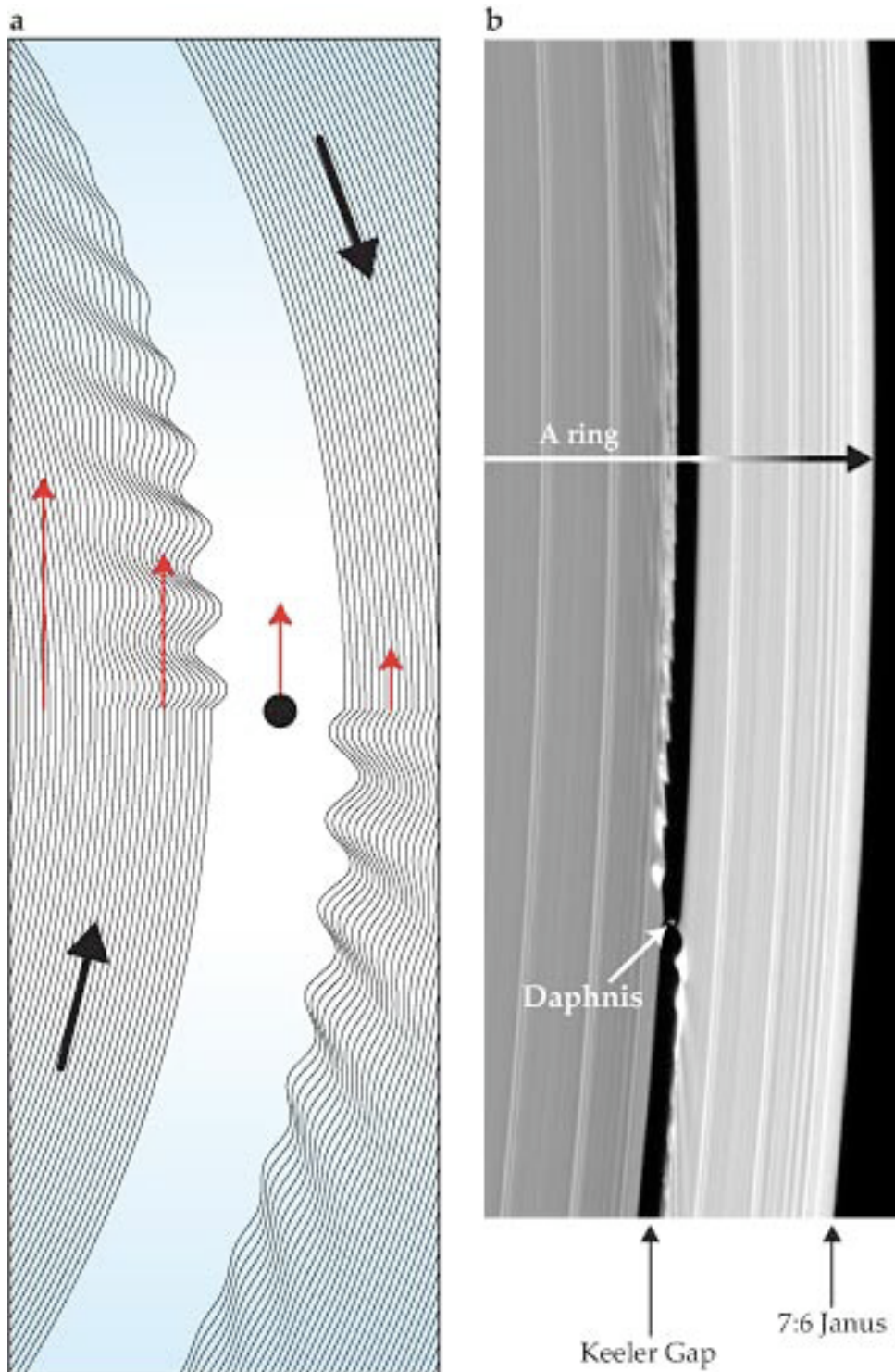
Figure 5. From Murray 2007. a) Streamline diagram showing 3πΔa wavelength set up as ring material passes a gap moon. This establishes the moonlet wake pattern observed in the Keeler Gap in panel (b). Panel (a) is in the gap moon's reference frame. Ring material moves faster with decreasing orbital semi major axis (red arrows), which results in the

moon experiencing inner material moving forward, outer material moving backward (black arrows). b) *Cassini* image courtesy of NASA/JPL/Space Science Institute.

Before the gap moons had been discovered, the moonlet wakes were tracked. For example, Cuzzi and Scargle (1985) and Showalter et al. (1986) tracked the Encke Gap moonlet wakes. This analysis allowed Showalter (1991) to discover Pan in archival Voyager images using the description of the wake pattern discussed above.

1.2.3 **Self-gravity wakes**

As discussed in Section 1.2.1, no sharp boundary exists between the region where accretion dominates and the region where disruption dominates. In the transition region called the "Roche Zone," clumping caused by gravitational instabilities or satellite perturbations can be torn apart on orbital timescales by tides or more satellite perturbations. A particular phenomenon arises when gravitational instabilities are disrupted by tides, which is known as self-gravity wakes (SGWs) (Figure 6). Toomre's Q parameter characterizes this balance:

$$Q_{Toomre} = \frac{c_s \kappa}{\pi G \Sigma}$$

Equation 3

where c_s is the radial velocity dispersion, Σ is the local surface density, and $\kappa = \Omega$ for a Keplerian disk. If $Q_{Toomre} > 1$, then the disk is stable to gravitational collapse and unstable otherwise. In practice, gravitational instabilities will occur if Q_{Toomre} is near unity, which can happen as the surface density increases and random velocities are damped. SGWs occur near $Q_{Toomre} \sim 2$, and are seen over a wide radial region in the A ring (Tiscareno, et al., 2007).

The SWGs are elongated in a direction of a few degrees to tens of degrees from the azimuth. They are spaced perpendicular to the elongation direction by a distance described by the Toomre wavelength:

$$\lambda_{Toomre} = \frac{4\pi^2 G\sigma}{\kappa^2}$$

Equation 4

SGW have many implications for Saturn's rings. Colombo, et al. (1976) suggest that SGWs are responsible for the azimuthal brightness asymmetry. Further, stellar occultations from Cassini UVIS (Colwell, et al. 2006, 2007) and VIMS (Hedman, et al. 2007a; Nicholson and Hedman 2010) show that the distribution of optical depths in SGWs is bimodal, with the wake as near opaque and space between at a much lower optical depth. Additionally, numerical simulations by Robbins, et al (2010) indicate that SGWs can "hide" mass because increased surface density adds more mass to the already-opaque wakes but weakly increases the overall optical depth. They estimate a mass for the B ring that could be ten times higher than Voyager-era estimates. SGW are structures that allow for clumping in regions of competing accretion and disruption processes.
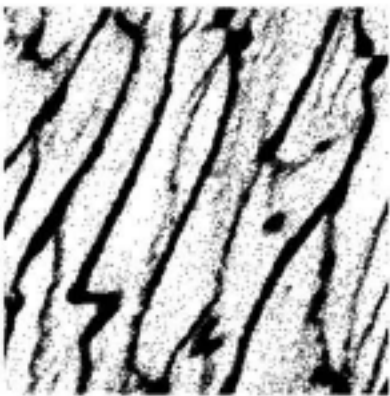
Figure 6. From Robbins, et al. (2010), Figure 2. This is a simulated self-gravity wake for a density of 0.45 g cm^{-3} and particle size R=1 m. Optical depth is 0.707.

1.2.4   **Ring Shepherds**

Saturn's F ring and Uranus' ε ring are the only two narrow rings to have known "shepherd" moons orbiting on either side of them. Despite the title "shepherd," there is no conclusive evidence that either Prometheus or Pandora actually constrain Saturn's F ring in its place. Rather, they seem to stir things up more than they constrain (Section 1.3.1 and 2.6). Closer and more massive, the interior moon Prometheus dips near the F ring periodically and creates a subsequent streamer channel. This streamer channel then moves downstream via Keplerian shear (Fig. 24, Murray et al. 2005). Likewise, Cordelia and Ophelia orbit interior and exterior to Uranus's brightest ring, the ε ring (Smith, et al. 1986). Other than location, there is really no indication that these moons perform any shepherding of that ring.

Alternatively, Salo and Hanninen (1998) show that Galatea may be a shepherd of Neptune's Adams ring. The moon is in 42:43 resonance with the ring arcs, so it may be responsible for their maintenance (Namouni and Porco, 2002). No outer shepherd for the Adams ring has yet been observed, however.

1.2.5   **Propellers**

In the case that a moon is too small to open a circumferential gap in the rings, it creates a local disturbance known as a "propeller." Keplerian motion of ring material results in disturbed material interior (exterior) to the moon orbiting faster (slower) and moving forward (backward) from the moon's reference frame. This creates a structure that resembles propeller blades, hence the name.

Propellers had been predicted and modeled (Spahn and Sremcevic 2000; Sremcevic, et al. 2002; Seiβ, et al. 2005) before their discovery in Cassini observations (Tiscareno, et al.

2006; Sremcevic, et al. 2007; Tiscareno, et al. 2008, 2010). The propeller structure itself is the observed object, as the central moon is below the detection threshold. Three propeller belts in the A ring have been identified to date between 127,000 and 132,000 km. These contain many small propellers with radial extents of 0.3 to 1.4 km and azimuthal lengths of several km (Tiscareno, et al. 2008). In the outer (trans-Encke) A ring, a belt of "Giant Propellers" has been found. These are outward of the Encke Gap (133,700 km), with radial widths upwards of 6 km and azimuthal extent of up to several thousand km (Tiscareno, et al. 2010). Cassini UVIS occultations have recorded several propeller-created gaps in the B ring, one of which also appears in ISS images (Sremcevic, private communication).

As with moonlet wakes, propellers contain surface density enhancements and depletions. The actual structure of these regions is still under debate. The smaller propeller belts contain numerous structures, each with an inferred moonlet. These moonlets and the density enhancements they induce appear to be transient (Tiscareno, et al. 2010), much like the moonlet and aggregate belts of other ring regions where accretion and disruption compete.

1.3 F ring as a laboratory for accretion processes

The F ring is by far the best-studied narrow dusty ring. Initially detected in 1979 by the Pioneer 11 imaging team (Gehrels, et al. 1980), the ring now has over three decades of observations by instruments including: HST, Voyager 1, and Cassini. It lies approximately 3000 km outside the A ring in a region where accretion and disruption continuously compete. Among the structures contained in it's meager ~10 km radial width are jets, strands, and moonlets over an azimuthally asymmetric span. In addition, the nearby moons Prometheus and Pandora stir up ring material and create an observably changing structure on timescales of days to decades. The well-observed, transient phenomena occurring in it make the F ring the solar system's principal natural laboratory for direct observation of accretion and disruption processes.

1.3.1 Introduction to F ring properties

The F ring has been called an "enigma" (Barbara and Esposito 2002), but the general properties of the ring are thoroughly known. The F ring sits at 140,221.3 km from Saturn's center (Albers, et al. 2012), which is a few thousand kilometers from the outer edge of Saturn's A ring. The F ring has both a vertical thickness and inclination of approximately 10 km, which is larger than that of the main rings. While this frustrates any attempt to study the main rings edge on, it allows for excellent ring plane crossing studies of the F ring itself.

Variations in the core's internal structure and in the surrounding dust have taken place between the Voyager and Cassini spacecraft visits (Colwell, et al. 2009). However, despite being notorious for the transient structures it hosts, the F ring core maintains over decadal

timescales the shape of a freely precessing eccentric inclined ellipse; the orbital solution

formulated to account for Voyager and other pre-Cassini data (Bosh, et al. 2002) remains a

good predictor of the core's position through the Cassini mission (updates in Murray, et al.

2008; Albers, et al. 2012).

1.3.2 **Studies of the F ring**

Cuzzi and Burns (1988) interpreted Pioneer 11 depletions in magnetospheric

particles in the region, which they attribute to small moonlets (<10km). Later, Voyager

observations revealed broad strands and burst events that showed the F ring as variable on

short time scales and over azimuthal distances (e.g. Lane, et al. 1982; Smith, et al. 1982;

Murray 1992; Murray, et al. 1997; Showalter 2004). Kolvoord, et al. (1990) found periodic

brightness enhancements in Voyager images of the F ring that are consistent with

Prometheus apoapse passages. During the 1995 ring plane crossing, edge-on observations

identified small bodies (Bosh and Rivkin 1996; Nicholson, et al. 1996). These observations

show the F ring is a mix of large and small particles with significant spatial and temporal

variability. This large-scale variability is apparent in imaging of both the F ring core

including kinks, knots, braids, and clumps (Smith, et al. 1981,1982; Showalter 1998; Poulet,

et al. 2000; Murray, et al. 2005, 2008) and the F ring strands in the form of a kinematic

spiral (Charnoz, et al. 2005).

The search has been on for an unseen belt of km-size moonlets since the Cuzzi and

Burns (1988) prediction. "Fan" structures such moonlets create in surrounding dust

(Murray, et al. 2008; Beurle, et al. 2010), direct detection by occultations (Meinke, et al.

2012; Esposito, et al. 2008; Hedman, et al. 2010b), and shadows cast during the 2009

Saturnian equinox (Beurle, et al. 2010) all indicate such a moonlet belt does exist.

Since the Cassini spacecraft reached Saturn, the F ring has been a target for study of small body formation and ring evolution. Esposito, et al. (2008) report 1-10 km bodies, double core regions, and temporal variability from UVIS stellar occultation observations. VIMS (e.g. Hedman, et al. 2007) co-observed at least one of these features. ISS images show kinks, knots, braids, strands, clumps, and spirals in the F ring (Charnoz, et al. 2005 ; Murray, et al. 2005, 2008; Showalter 2004; Poulet, et al. 2000). Murray, et al. (2008) observe structures created by Prometheus in ISS images. Beurle, et al. (2010) show that Prometheus makes it possible for "distended, yet long-lived, gravitationally coherent clumps" to form.

The 2009 Saturnian equinox serendipitously coincided with the 19 year alignment of Prometheus' apoapse with the F ring's periapse. This allowed observation of moonlet shadows. These inferred moonlets have a clear correlation of abundance with longitude relative to Prometheus (Beurle, et al. 2010). Similarly, Esposito, et al. (2012) find evidence from UVIS occultations that clumping in the F ring is correlated to the location of Prometheus, indicating that accretion of small bodies in the F ring may be triggered by the moon's influence.

Models have attempted to explain the distribution of small bodies in the F ring as the equilibrium between accretion and fragmentation. Barbara and Esposito (2002) (hereafter BE02) predict that the F ring evolves to a bimodal distribution of bodies that has a large population of dust as well as few km-sized bodies. In addition, numerical and semi-analytical works have predicted clumping in narrow rings (Longaretti 1989) and rings in a planet's Roche zone (Ohtsuki 1993; Salo 1995; Karjalainen and Salo 2004). N-body simulations of the A and B rings show short-lived clumping of material that could also

occur in the F ring (Lewis and Stewart 2009). Thus, the F ring is an interesting place of exploration as a testing ground to compare to clumping processes elsewhere in the rings (e.g., A ring propeller belt or B ring edge).

1.4 Applications beyond the F ring

Studies of ring systems in our Solar system can provide insight into other astrophysical disks, both far away and long ago. For example, the number of extrasolar planets observed has grown from a handful to over 700 in the last decade (Schneider 2011). A large fraction of those planets are gas or ice giants and probably host ring systems. Furthermore, observations of the protoplanetary disks from which they form are of increasing resolution and number. Synergy among these studies of flattened orbital systems can tell us about moon and planet formation, collisional fragmentation, disk structures, and the like. This in turn can tell us about the history of our own Solar system with studies of the asteroid belt and Kuiper belt's collisional evolution.

2.   Observations
2.1   Introduction

Since its discovery (Gehrels et al., 1980), the F ring of Saturn has been the focus of

many observations and revealed new insights into ring dynamics and evolution. Cuzzi and

Burns (1988) interpreted Pioneer 11 depletions in magnetospheric particles in the region,

which they attribute to small moonlets (<10km). Later, Voyager observations revealed

broad strands and burst events that showed the F ring as variable on short time scales and

over azimuthal distances (e.g. Lane et al., 1982; Smith et al., 1982; Murray, 1992; Murray et

al., 1997; Showalter, 2004). Kolvoord et al. (1990) found periodic brightness

enhancements in Voyager images of the F ring that are consistent with Prometheus

apoapse passages. During the 1995 ring plane crossing, edge-on observations identified

small bodies (Bosh and Rivkin, 1996; Nicholson et al., 1996). These observations show the

F ring is a mix of large and small particles with significant spatial and temporal variability.

This large-scale variability is apparent in imaging of both the F ring core including kinks,

knots, braids, and clumps (Smith et al. 1981,1982; Showalter 1998; Poulet et al. 2000;

Murray et al. 2005, 2008) and the F ring strands in the form of a kinematic spiral (Charnoz

et al., 2005).

Since the Cassini spacecraft reached Saturn, the F ring has been a target for study of

small body formation and ring evolution. Esposito et al. (2008) report 1-10 km bodies,

double core regions, and temporal variability from UVIS stellar occultation observations.

VIMS (e.g. Hedman et al., 2007) co-observed at least one of these features. ISS images show

kinks, knots, braids, strands, clumps, and spirals in the F ring (Charnoz et al. 2005 ; Murray

et al. 2005, 2008; Showalter 2004; Poulet et al. 2000). Murray et al. (2008) observe

structures created by Prometheus in ISS images. Beurle et al. (2010) show that

Prometheus makes it possible for "distended, yet long-lived, gravitationally coherent clumps" to form. Esposito et al. (2011) find evidence that clumping is correlated to the location of Prometheus, indicating that accretion of small bodies in the F ring may be triggered by the moon's influence.

Models have attempted to explain the distribution of small bodies in the F ring as the equilibrium between accretion and fragmentation. Barbara and Esposito (2002) (hereafter BE02) predict that the F ring evolves to a bimodal distribution of bodies that has a large population of dust as well as few km-sized bodies. In addition, numerical and semi-analytical works have predicted clumping in narrow rings (Longaretti, 1989) and rings in a planet's Roche zone (Ohtsuki, 1993; Salo, 1995; Karjalainen and Salo, 2004). N-body simulations of the A and B rings show short-lived clumping of material that could also occur in the F ring (Lewis and Stewart, 2009). Thus, the F ring is an interesting place of exploration as a testing ground to compare to clumping processes elsewhere in the rings (e.g., A ring propeller belt or B ring edge). Additionally, UVIS affords us the opportunity to detect aggregates tens of meters to a few kilometers in size. UVIS has much better spatial resolution than the cameras, which have achieved 500m/pixel thus far in the F ring (Porco et al., 2005, Murray et al., 2008), so we can probe deeper to understand the processes occurring at scales as small as tens of meters.

2.2 Ring Observations

The Cassini Ultraviolet Imaging Spectrograph (UVIS) has a High Speed Photometer (HSP) channel designed to observe stellar occultations (Esposito et al., 1998, 2004, 2005). The effective wavelength for this channel is about 1500 Å. As of September 22, 2010, UVIS

has observed 101 stellar occultations by the F ring. We identify individual occultations in this dissertation by the occulted star and the "rev" number during which the F ring occulted it, where "rev" refers to a Cassini orbit (apoapse to apoapse), which are numbered sequentially (0,A,B,C,3,4,5…). These data are available on the PDS, arranged by instrument, year, and day of year. Occultation data file names start with HSP.

The geometry of each occultation is calculated based on the positions of the star and the position of the spacecraft derived from the appropriate SPICE kernels. The individual reconstructed Cassini spacecraft trajectory SPICE kernels that have coverage of the occultations were used (all reconstructed kernels except for '090415BP_SCPSE_09105_09115.bsp', '101222BP_SCPSE_10353_11015.bsp', and '101229AP_SCPSE_10363_11015.bsp'). These are available via anonymous ftp at ftp://naif.jpl.nasa.gov/pub/naif/CASSINI/kernels/spk. This information was used to predict the position (radius and inertial longitude) of the star in Saturn's ring plane as a function of time, listed as radial position and longitudes in Table 1. The Saturn pole direction used was from 'cpck17Dec2010.tpc'.

These observations allow us to measure the F ring's opacity at various times, longitudes, and angles (Colwell et al., 2006, 2007, 2010), from which we identify individual structures throughout the ring. In addition to observing long-lived features consistent with "strands" (Albers et al. 2009,2012), we also identify smaller, non-repeatable structures in isolated occultation profiles. With occultations, follow-up observations are extremely difficult if not impossible, so we use optical depth of such small features as an estimator of longevity as did Esposito et al. (2008). The higher a feature's optical depth, the longer it

takes to diffuse apart, so it will be a longer-lived (meaning surviving multiple orbits) object

(Shu and Stewart, 1985).

2.3 **Search Method**

      The method used to identify significant attenuations in the stellar signal during

occultations is adapted from the search method described in Esposito et al. (2008). The

search method consists of two parts: a test for statistical significance and a subsequent

persistence test. We have improved the method presented by Esposito et al. (2008) by

searching over a uniform radial range of distance from Saturn, probing different bin sizes,

and requiring features to be of greater statistical significance than they did.

      First, we considered a feature that was independently verified by VIMS. The feature,

nicknamed "Pywacket," was simultaneously observed by VIMS and UVIS during the

occultation of α Sco rev 13 (Esposito et al. 2008). Both instruments observed a significant

increase in opacity ~600 m in radial width. Since this detection is in both UV (~1500 Å)

and near IR (2.92 μm), it assures this event was not a statistical fluctuation but a real event.

Figure 7 shows the two observations. We used this confirmed detection to refine our

search algorithm for similar features in the UVIS data.
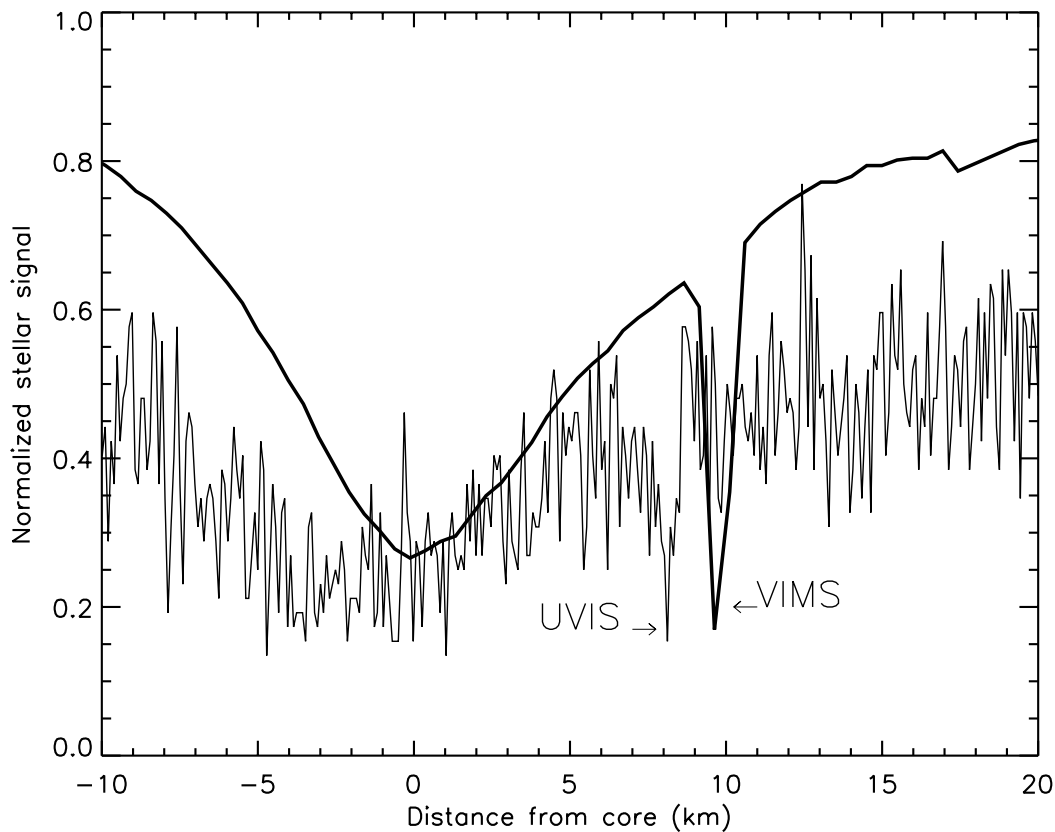
Figure 7. VIMS (solid, smooth curve) and UVIS (thinner curve) α Sco egress, rev 13 occultation data overplotted. The UVIS curve is scaled to match the VIMS unocculted stellar flux (outside the plotted range). The two instruments have different spatial resolutions, but both clearly detect Pywacket outside the F ring core. UVIS identifies the clump at ~8 km, VIMS at ~10 km because the instruments sample different inertial longitudes of the ring; while separately observing each of the stars comprising the double star α Sco. This situation allows for the observation of an offset that is indicative of an elongated clump.

The search algorithm has two completely automated parts. The first searches for statistically significant attenuations in the stellar signal, while the second requires a feature to have a minimum optical depth.

1)   For each occultation, the data in the radial range 139,000 km to 141,000 km are binned at a given radial size.   The number of integrations per bin varies among occultations as the geometry and thus resolution varies; therefore, we choose a fixed radial bin size and sample over a fixed radial range in order to make this test more consistent

26

than Esposito et al. (2008). Then, we offset the start of binning, creating N different occultation profiles for a bin size of N time integrations for every possible distinct binning of the data. Next, we determine a smoothed baseline value for the F ring opacity. To do so we take a running mean from approximately 5 km of stellar signal, or number of photons detected, surrounding and including each bin. This definition for the baseline was compared to alternatives, including medians, polynomial fits, splines, and various other radial ranges for the running mean; however, we select this method because the Pywacket feature is most statistically significant using this particular baseline (specifically, a running mean of 81 bins of 5 integrations surrounding and including the center bin).

Assuming the HSP signal is described by a Poisson distribution, well-satisfied for our data and confirmed by observations of blank regions, where μ corresponds to the baseline value and C is the binned stellar signal at a particular bin, the probability of measuring a value of exactly C is given by

$$P(\mu,C) = \frac{e^{-\mu}\mu^{C}}{C!}$$
Equation 5

To find the probability that the stellar signal would be less that or equal to C at that bin, we sum the distribution over all signal values less than C:

$$P(\mu,\leq C) = \sum_{j=0}^{C} \frac{e^{-\mu}\mu^{j}}{j!}$$
Equation 6

We perform this calculation for each bin, i, in the data set to find $P_i = P(\mu_i, \leq C_i))$. We then multiply P_i by the number of tested bins in the data set, v. This gives $m = vP_i$ (Colwell et al., 1990). Events with $m < m_{significant}$ are statistically significant because it is unlikely that such an event would occur by chance in the profile. Mathematically, the critical m value $m_{significant}$ is 1 and used for most occultations; however, for a handful of observations of

bright stars when raw stellar signal exceeds 128 counts the value is set at a more

conservative 0.1. This is due to compression of the UVIS data (square root nine

compression, see Esposito et al. 2004) that reduces the transmitted data to 8 bits, which

can produce spuriously low counts. The value $m_{significant}$=0.1 was estimated from testing a

number of surrogate Poisson processes after compression was applied. This is a new

requirement beyond that reported in Esposito et al. (2008).

If a feature is flagged in at least one of N different starting point binnings, we count

in exactly how many different binnings it is flagged. This number K is then compared to

$|N$-$W|$, the difference in bin size N and feature size W, where W is full width at half

maximum (FWHM) in unbinned data. For a feature of width W, just barely detected by our

method, $|N$-$W|$ is the expected number of arbitrary starting points where it passes the

statistical test (for $W{\leq}2N$). For a feature to be significant, K (the number of configurations

in which the feature was flagged) must be greater than $|N$-$W|$. This procedure is repeated

for six different radial bin sizes: 25 m, 100 m, 250 m, 500 m, 1 km, and 2 km. We impose a

more rigorous requirement than Esposito et al. (2008); only if a feature is significant in at

least two different bin sizes will it be reported and flagged for the next test, the

"persistence" test.

2)   In the "persistence" test, each flagged event is examined to determine its width and

peak opacity at the radial bin size in which it was significant. To be included in our list, the

maximum binned normal optical depth ($\tau_{\perp}$= $\tau_{observed}\,sinB$) of the feature must be at least as

large as Pywacket (τ_{max} = 0.4 when binned to 500 m).   It should be noted that since we use

a statistical test, it is possible that some spurious events are recorded and that some real

features are missed. The largest uncertainty of this test is the unknown F ring background model (without features) with which to compare our possible features.

The radial width is the full width at half maximum of the consecutive integration periods that are part of the feature in an unbinned profile. Peak normal optical depth is the maximum value for the feature from the binned data. Because of the optical depth requirement, $\tau_{max}>0.4$, the ring particles in such aggregations collide multiple times each orbit (Shu and Stewart, 1985). The collision rate is proportional to the observed optical depth τ, and the number of collisions for a particle to escape the clump is proportional to τ^2. The clump lifetime is estimated by the ratio of the number of collision required for particle escape to the collision rate, τ^2/τ, thus it scales as the clump optical depth. An aggregate will diffuse apart as it suffers more collisions and eventually will break apart entirely. This means that more opaque structures will persist for multiple orbits.

Our search method introduces two qualifications to the characteristics of found features. First, star brightness varies from occultation to occultation. The Poisson statistics of a weak star are noisier than those of a bright star. Because peak normal optical depth is a feature-selection criterion, the brightness of a star may have some effect on selection; however, the persistence test requires a minimum optical depth that is derived from a confirmed feature (obviously not a statistical fluctuation), so we probably do not exclude any real features based purely on low statistical significance from dimmer stars. Another characteristic of our search method is a bias toward azimuthally elongated features in the F ring. An occultation that slices through the F ring has a higher probability of the occultation path intersecting a clump if the clump is elongated in azimuth. It follows from this bias that the features detected in this study may be elongated in longitude.

Simulations of ring material (Lewis and Stewart, 2009) and observed propeller structures (Tiscareno et al., 2008) have shown how ring material shears out over azimuth, thus elongating clumps. UVIS HSP occultations cut the ring almost radially from an inertial reference frame. The radial speed of the occultation is typically a few km/s, but ring material orbits beneath the occultation track at ~17 km/s; therefore, the occultation cuts are typically very slanted in the corotating frame providing some azimuthal component to the observed ring structure. We account for the elongation and corotation biases in the size distribution of features reported later in this section (2.5). We report only the apparent radial width of features here, but such features likely are not spherical and may have different widths in other dimensions.

2.4 **Data Analysis**

We apply this search algorithm to all 101 occultation profiles of the F ring. This yields 27 events, distributed in radial width from 22m to 3.7 km (see Table 1). We performed the same search for each of the 101 occultations in the region 138,000 ± 1,000 km, where we expect unattenuated stellar signal. As expected, we found no features that pass our search criteria in this region; therefore, we conclude the features we find in the F ring region almost certainly represent real structures in the F ring.

Seven of the 13 features (Events 3,6, and 9-13) reported in Esposito et al. (2008) were not found by this new search method. All seven are excluded because they do not pass our stricter statistical test; the set bin size of the Esposito et al. (2008) search algorithm was coincidently optimized for these features, but because they are not statistically significant at different bin sizes they do not pass our more conservative test. The six features from Esposito et al. (2008) that pass the new stricter test are reported as Events 1

through 6 in Table 1 in this dissertation. We find the 21 other features in occultations not searched in Esposito et al. (2008).

2.4.1 **Classification**

With 27 features detected over the course of 101 observed occultations by the F ring (Table 1, Figure 8), the authors have found it useful to develop a classification scheme. Three categories are apparent: Moonlet, Icicle, and Core (Table 2). These names describe the shape of the feature as seen in signal attenuation in the occultation profile. As such, the names are not intended to exactly identify the physical object obstructing stellar signal, as different types of objects may be associated with one type of observed occultation feature (and vice versa) because they are indistinguishable in the one-dimensional occultation profile. Each class has defining characteristics that distinguish it from the others. Two of the classes, Cores and Icicles, are broken down into sub-classes due to variations in the morphology of constituent members. The number of features in each class is listed in Table 2. This system of classification seeks to order the types of features within the F ring.
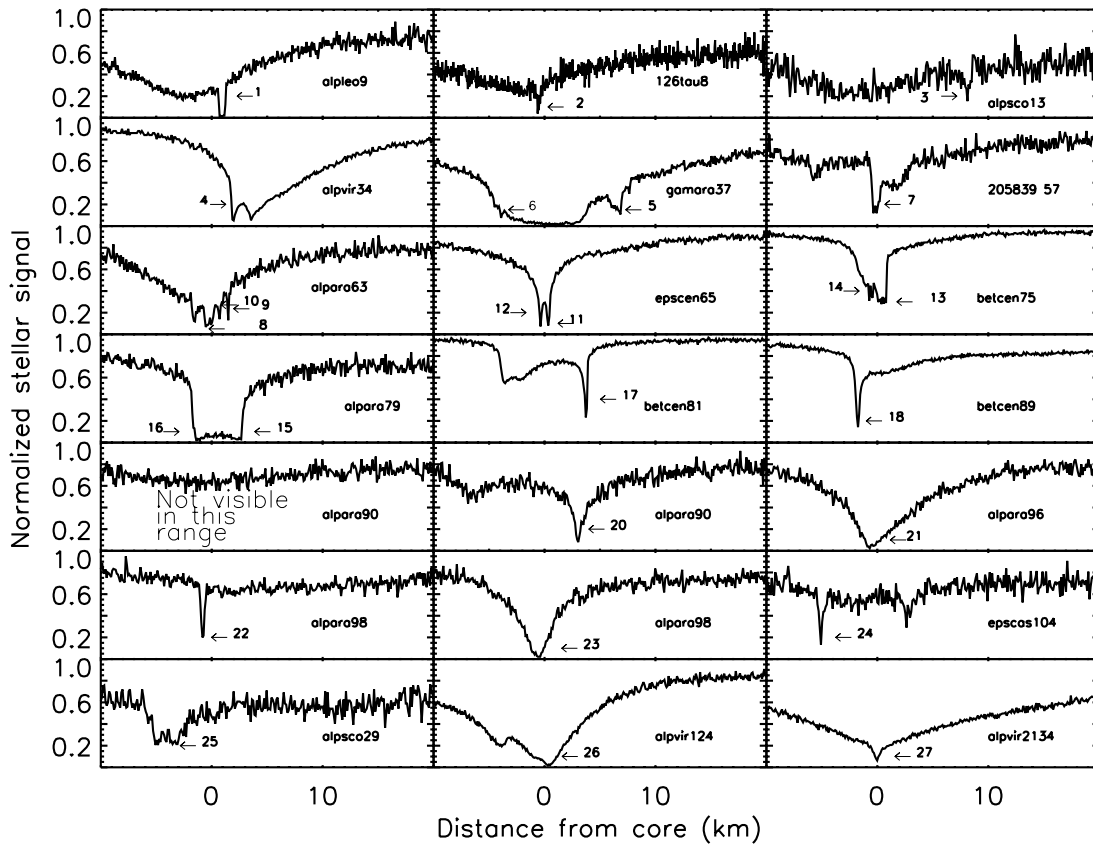
Figure 8. All 27 of the occultations where significant features were observed. Each is labeled with the type of feature observed and the star name and rev number of the occultation. The occultations are named with the rev number during which an observation was made and include "I" or "E" to denote "ingress" or "egress," respectively, for observations that included both segments. Each feature is labeled with an arrow and the event number from **Table 1**. All plots are over the same radial range, which is why α Ara, rev 90, Ingress is labeled "Not in range" because the Moonlet appears in the core-like inner strand region (Figure 9b). Longitudes and reference radii were computed using the eccentric, inclined F ring model of Albers et al. (2011). "Distance to core" is the radial position of the feature relative to the observed F ring core reference radius, which is defined by the visually-determined point of greatest attenuation. The F ring "core" is the region of greatest attenuation in an occultation, coincident with the highest density region of the ring. All occultations have signal binned to 100 m.

32

Event #	Nickname	Occ (Rev)	m value	Radial Width (km)	UTC	Peak norm OD	Radial Distance (km)	Longitude	Distance to core (km)	category	total mass (sphere) (kg)
*1	Mittens	Alp Leo 9	7.15E-08	0.594	2005-159T05:06:35.057	0.564	139915.04	350.52	2.702	moonlet	2.53E+14
*2	Tiger	126 Tau 8	2.50E-02	0.022	2005-139T14:17:09.019	1.096	140067.33	227.21	1.722	multi-icicle	3.40E+11
*3	Pywacket	Alp Sco 13 E	1.71E-01	0.763	2005-232T14:17:45.714	0.401	140550.43	10.04	9.756	simple-icicle	4.17E+14
*4	Butterball	Alp Vir 34 E	1.31E-06	3.739	2006-337T04:05:24.518	0.434	140170.80	89.88	1.853	W-core	
*5	Snowball 2	Gam Ara 37 I	8.11E-11	0.211	2007-022T01:40:20.764	2.415	140289.69	248.44	6.235	multi-icicle	3.19E+13
*6	Schmutz		2.35E-02	0.105	2007-022T01:40:23.828	2.483	140278.89	248.44	-4.567	simple-icicle	7.90E+12
7	Garfield	205839 57	2.80E-02	0.531	2008-026T14:54:07.986	0.597	140400.06	186.88	0.597	multi-icicle	2.02E+14
8	Heathcliff 1	Alp Ara 63	6.48E-06	0.531	2008-092T12:09:48.285	2.460	140501.12	26.12	-1.331	multi-icicle	2.02E+14
9	Heathcliff 2		2.81E-01	0.097	2008-092T12:09:48.581	1.800	140503.51	26.12	0.894	simple-icicle	6.70E+12
10	Heathcliff 3		1.72E-05	0.774	2008-092T12:09:48.409	2.286	140502.12	26.12	-0.230	multi-icicle	4.30E+14
11	Fang 1	Eps Cen 65	1.01E-08	0.129	2008-110T10:16:33.513	1.809	140216.90	202.92	0.636	W-core	
12	Fang 2		5.18E-04	0.090	2008-110T10:16:33.657	1.652	140216.18	202.92	-0.081	W-core	
13	Whiskers 1	Bet Cen 75	3.78E-02	0.093	2008-188T20:49:32.052	1.208	139945.52	173.03	1.176	multi-icicle	6.13E+12
14	Whiskers 2		1.08E-01	0.046	2008-188T20:49:32.211	1.494	139944.29	173.03	-0.053	simple-icicle	1.53E+12
15		Alp Ara 79	3.16E-03	0.574	2008-217T03:25:05.953	3.404	140146.11	138.32	2.293	W-core	
16			5.04E-01	0.469	2008-217T03:25:06.373	2.879	140142.46	138.31	-1.364	W-core	
17	Mohrle	Bet Cen 81	8.80E-05	0.194	2008-231T11:39:21.682	1.786	140205.54	168.48	3.454	simple-icicle	2.69E+13
18	Vasska	Bet Cen 89	2.89E-06	0.251	2008-290T09:01:32.589	1.433	140333.58	167.80	-1.578	simple-icicle	4.50E+13
19	Sylvester	Alp Ara 90 I	1.17E-12	0.107	2008-298T01:39:13.119	2.518	139932.76	139.06	-127.592	moonlet	8.23E+12
20		Alp Ara 90 E	1.31E-04	0.553	2008-298T06:32:57.584	2.378	139960.08	37.36	3.403	W-core	
21		Alp Ara 96 E	2.16E-04	0.663	2008-344T09:59:12.483	2.684	140504.56	50.65	-0.411	V-core	
22	Tabby	Alp Ara 98 I	2.31E-01	0.213	2008-360T06:24:18.408	1.304	140322.79	134.53	-1.603	simple-icicle	3.25E+13
23	Socks	Alp Ara 98 E	1.59E-06	1.168	2008-360T11:55:46.407	3.405	140526.72	57.38	-0.035	multi-icicle	9.77E+14
24		Eps Cas 104 E	4.15E-08	0.122	2009-058T17:39:08.413	1.682	140180.95	137.34	-4.342	W-core	
25	Felix	Alp Sco 29	2.61E-01	2.167	2006-269T06:35:35.921	0.658	139923.21	201.68	-11.427	multi-icicle	3.37E+15
26		Alp Vir 124	1.96E-02	0.852	2010-011T13:37:01.113	0.995	140331.91	306.20	0.000	W-core	
27		Alp Vir 134	8.13E-03	0.030	2010-186T09:05:04.125	0.725	140558.10	136.70	0.000	V-core	

Table 1. Characteristics of each significant feature found in 101 UVIS F ring occultation profiles. The occultations are named with the rev number during which an observation was made and include "I" or "E" to denote "ingress" or "egress," respectively, for observations that included both segments. Icicles and Moonlets are nicknamed because they are likely associated with specific objects in the ring, while Cores are not because they are varying shapes of the ring. Longitudes and reference radii were computed using the eccentric, inclined F ring model of Albers et al. (2011). "Distance to core" is the radial position of the feature relative to the observed F ring core reference radius, which is determined by visually selecting the position of greatest attenuation. The F ring "core" is the region of greatest attenuation in an occultation, coincident with the highest density region of the ring. Note that the two opaque features, 1 Mittens and 19 Sylvester, are listed with a finite optical depth because those values are the maximum optical depth values for those particular occultations. Features noted with an "*" (Events 1-6) are also reported in Esposito et al. (2008) as Events 1, 2, 4, 5, 7, and 8; however, the other seven features reported in Esposito et al. (2008) did not pass the stricter test presented here. No new features were found in previously searched occultations. The geometric values given here are calculated using the individual reconstructed Cassini spacecraft trajectory SPICE kernels that have coverage of the occultations used. These are available via anonymous ftp at ftp://naif.jpl.nasa.gov/pub/naif.CASSINI/kernels/spk/ . For the geometry in this study, 'cpck17Dec2010.tpc' was used.

Class	Number in Class
Moonlet	2
Icicle	15
Core	10

Table 2. This table lists the number of significant features in each class.

2.4.1.1 **Moonlets**

These features are quite distinct from any other features yet observed. Members of this class attenuate stellar signal to background levels, so we interpret them as opaque features. This indicates that the objects causing these observed opaque features may be solid objects, rather than completely loose aggregations of material that are capable of letting light pass through their porous interiors.   Unlike an atmosphereless-moon occultation with vertical drop-offs in signal, the edges of these features exhibit a steep but sloped decrease in signal, indicative of a thin, loosely-aggregated surface layer around a solid object. Thus far, two Moonlets have been observed. One of the features, nicknamed 'Mittens,' observed during the occultation of α Leo during rev 9, blocks all stellar signal for a radial distance of 594 m, with small transition regions of attenuation in signal on both sides (Figure 9a). The other feature in this class, nicknamed 'Sylvester,' is observed in the occultation of α Ara, Ingress, rev 90. This feature is interesting because it is the only one that lies in the core-like inner strand of the F ring (Albers et al. 2012), while all of the other 26 observed significant features lie in or near the core of the F ring. Although smaller in width (107 m) than the other Moonlet, Sylvester also exhibits steep drop-offs in stellar signal to the background level (Figure 9b).

Alp Leo R09 (in) [Mittens]

a=250m
b=500m
c=250m
h=200m

Alp Ara R90 (in) [Silvester]

a=60m
b=120m
c=60m
h=150m
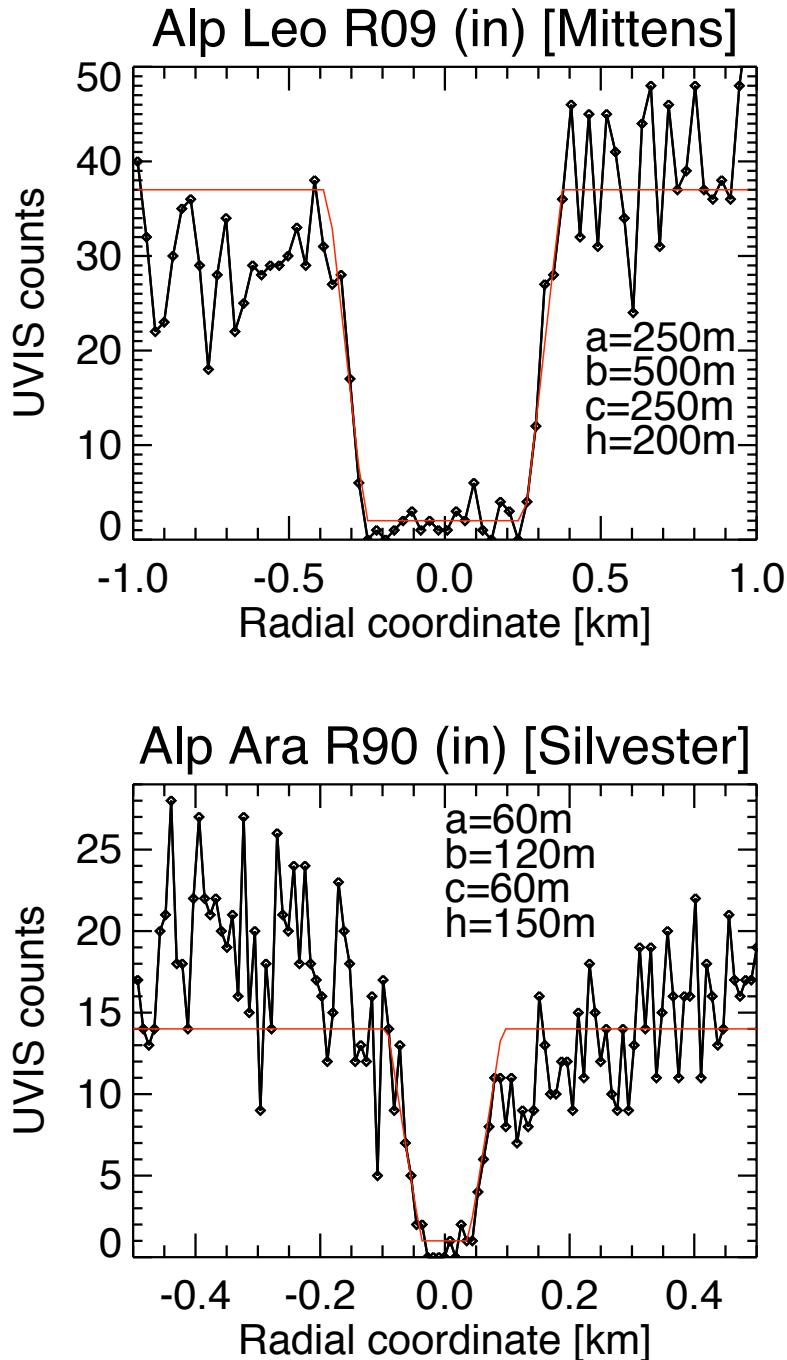
Figure 9. The two features classified as Moonlets because both have sharp edges and attenuate stellar signal to the background level. Our simple model demonstrates that a realistic triaxial ellipsoidal body with a semi-transparent surface layer matches the data from the two occultations in this figure. Since in both geometries the body is essentially viewed from the side (B(α Leo, rev 9) = 9° and B(α Ara, Ingress, rev 90) =-54°), the radial and vertical dimensions are unconstrained. The thickness *h* directly gives the transition

from the background to the ring level, which does not warrant a sophisticated model and we simply employed a linear function.

a) Occultation profile of α Leo rev. 9 in raw counts. The feature at 139917 km is "Mittens." Fits of the occultation constrain the azimuthal body axis b to be 500m and unconsolidated layer width h=200m.

b) Occultation of α Ara rev 90 in raw counts. The Moonlet nicknamed "Sylvester" is at 139930 km. The dimensions b=120m and h=150m are constrained by the fits for this occultation.

2.4.1.2 **Icicles**

The Icicle class of F ring features has the largest number of members at 15. This class is so named because the abrupt drop in stellar signal resembles an icicle hanging from eaves. Members of this group are smaller formations, usually under a kilometer in radial width (Figure 10), and can be divided into two subclasses. The Icicle nicknamed Pywacket in Esposito et al. (2008) is an example of a simple Icicle, or one that is alone in a region. The other subclass of Icicles is the multi-icicle, which occurs when several simple-icicles cluster in a confined region. An example of this can be seen in α Ara rev 63 (Figure 10c), with the inner, wider feature being a multi-icicle and the outer, smaller feature a simple-icicle. Eight multi-icicle significant features are too many to be created by randomly located independent events and demonstrate the tendency of multiple features to occur together.
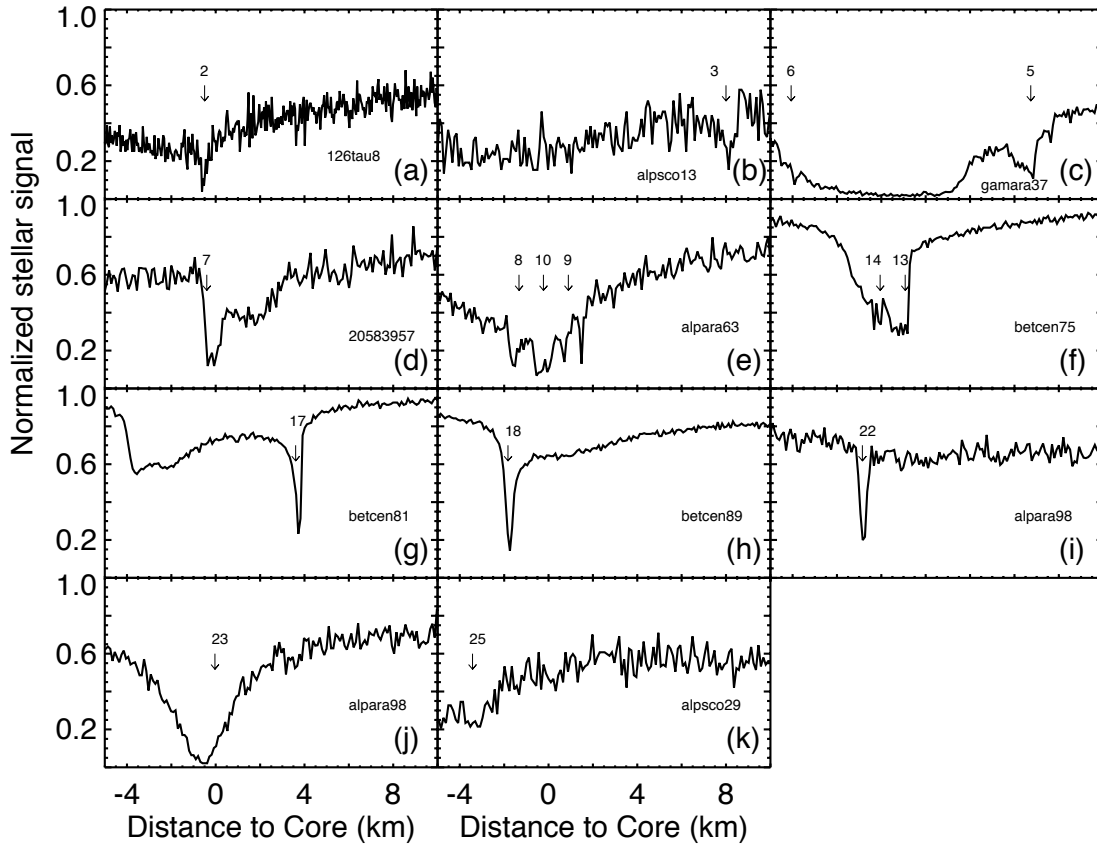
Figure 10. Members of the Icicles class. Features are labeled with an arrow and their "Event number" from **Table 1**. Occultations are identified by the star occulted and the rev number during which the observation occurred.

2.4.1.3 **Cores**

Another class of observed features is Cores. The F ring typically has one central core region that is "U"-shaped and approximately 10 km wide. We identify two other variations in core region shape: "V" and "W". These designations describe the signal attenuation along the radial direction of the ring in an occultation profile. The "V"-shaped core is likely a concentration of material in a dense, ~500 m-wide stream surrounded by a linear decrease in optical depth on both sides, as pictured in the α Ara, rev 96 egress occultation profile in Figure 11e. Of the ten features included in the "cores" class there are two significant "V"-cores seen (other "V"-shaped cores appear within the scope of this study, but those are not

included in our list because they do not qualify as statistically-significant features).

Another common F ring core shape is the "W." A possible explanation for the "W"-shaped

core could be that described by Brophy et al. (1990). They discuss such a configuration due

to particle-size segregation, leading to an inner region of low optical depth flanked by

roughly equal-sized regions of higher opacity, like the ε Cen, rev 65 occultation profile in

Figure 11b (nicknamed Fang 1, 2). We identify a total of eight significant "W"-core features

over the specified observing campaign.
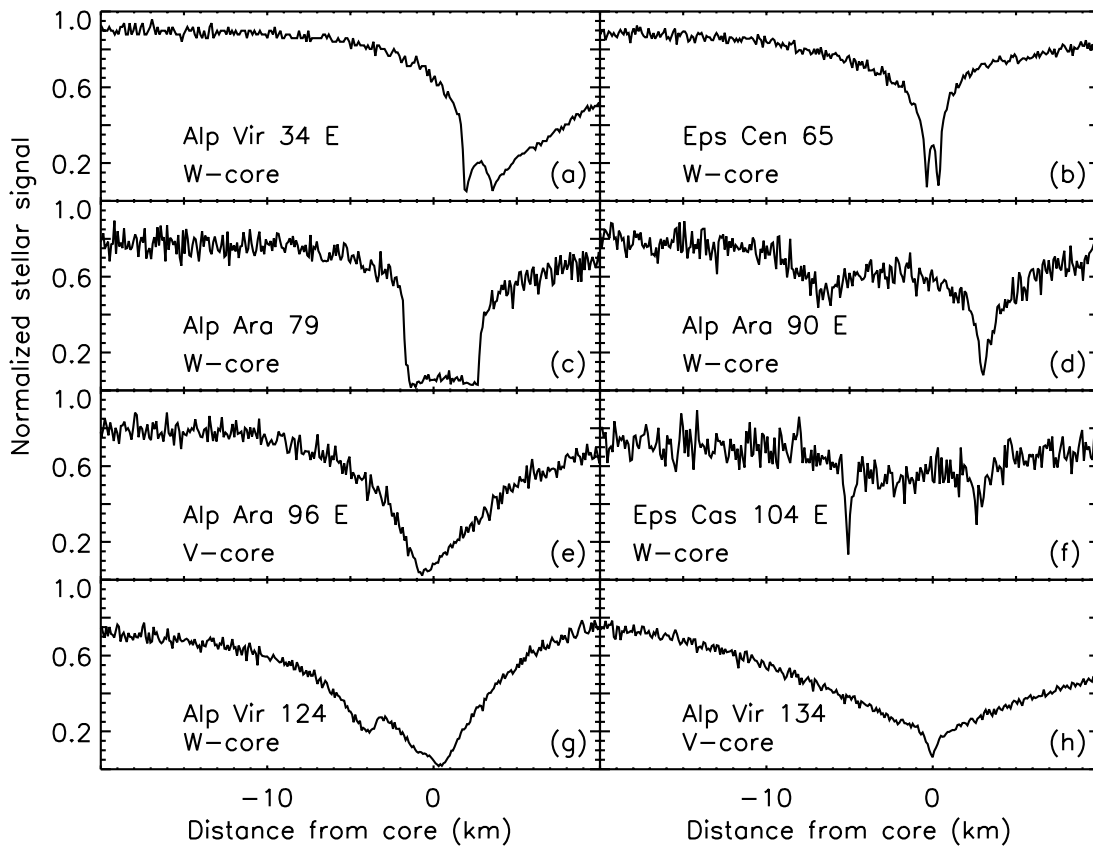
Figure 11. Statistically-significant core regions. **a.** Occultation of α Ara rev 34 egress. We classify this feature, nicknamed Butterball, as a W-core. **b.** Occultation of ε Cen rev 65. Example of W-core, nicknamed Fang 1 and Fang 2. **c.** Occultation of α Ara 79 shows W-core structure. **d.** Occultation profile of α Ara 90 egress. We classify this as W-core structure. **e.** Occultation profile of α Ara 96 egress. This is a V-core. **f.** Occultation profile of ε Cas 104 egress shows another W-core. **g.** Occultation profile of α Vir 124 shows another W-core. **h.** Occultation profile of α Vir 134 shows another V-core.

2.5 **Discussion**

Table 1 lists our features, showing the broad range of size, shape, and optical depth of the significant features we observe in the F ring. The table gives the location of each feature with respect to the F ring core, the location of which is defined by the visually-determined point of greatest attenuation. Features are seen inside, outside, and at the F ring core location. From our sample of significant features, there is only one major outlier from the ring core, the Moonlet nicknamed Sylvester, which is also the only feature found in the core-like inner strand (Albers et al., 2011) region. The classification of this large number of F ring events by morphology reveals the prevalence of certain shapes, sizes, and opacities. Although these classes are based on the shape of the signal attenuation in the occultation profile, we may associate them with different types of objects embedded in the ring. Cassini UVIS occultations have certainly revealed that the F ring core takes many different shapes and is not azimuthally symmetric. Certain longitudes experience a narrowing of the core resulting in a "V"-shaped core (Esposito et al., 2008). Meanwhile, particle size segregation may result in the "W"-shaped cores in other regions (Brophy, et al., 1990; Lewis and Stewart, 2009). Icicles are density enhancements that we conclude indicate elongated clumps of ring particles (Lewis and Stewart, 2009). It is important to remember here that each occultation feature classification does not necessarily correspond to one type of object in the ring. For example, the multi-icicle "Whiskers" is also consistent with moonlet wakes (Albers et al., 2012). We interpret the Icicles as temporary aggregates that we call "clumps" and the Moonlets as possible solid bodies.

The two Moonlet-class features lead us to assess the type of object responsible for such signal attenuations. As the name suggests, these objects may be solid objects

embedded in the F ring; however, their edges in occultations are not perfectly sharp (as obtained in moon occultations, e.g. Hansen et al. 2006) but have a gradient. Works of Porco et al. (2007) and Charnoz et al. (2007) have established that solid bodies within rings accrete the material until their Roche lobe is filled. Further mass increase requires some additional physical process, such as compaction. Thus, at any point the moonlets within the F ring have roughly filled their Roche lobes, and, while their gravity still attracts the ring particles, they are not bound to the moonlet. The attracted particles probably form a "skirt" of loose material around the moonlets. In order to model this we envision the moonlet as a triaxial solid body with axes (a in azimuthal, b in radial, and c in vertical dimensions) and a "skirt" of loose material of width h. The attenuation of star light by loose material is modeled as a linear decrease of transparency t=exp(-τ/|sin(B)|) from opaque solid core to the ring background. In this equation, τ is optical depth and B is the elevation angle of the occulation, which is 9° for the α Leo, rev 9 occultation with Mittens and -54° for α Ara, Ingress, rev 90 with Sylvester. Miodrag Sremcevic (Meinke et al, 2012) simulates an occultation cut across the center of the Moonlet in the moonlet corotating frame. In both cases of Mittens and Silvester the geometry is such that the moonlet is seen from the side, making fits sensitive only to the azimuthal extent of the moonlet (*a*,*h*). The radial axis *b* and vertical axis *c* are unconstrained. The azimuthal size of the body (*a*) gives the largest contribution to the width of the opaque part. While the width itself is well constrained from the data, the contribution from radial (*b*) and vertical (*c*) axes are not zero, thus giving significant uncertainty for *a*. Thus, Sremcevic deems that a chi-squared minimization is not warranted, and instead he present a possible solution for *a* and *h* that was found by visually inspecting plots with varying values for *a* and *h* in increments of about 5% (Meinke, et al.,

2012). A typical successful fit to UVIS data is shown in Fig 9a,b. Test fits with different

aspect ratios yield nearly the same body azimuthal axis of about *a=500m (120m*), and loose

material of width *h=200m (150m*) for Mittens (Silvester). Comparing the various plots we

can estimate that the uncertainty in a and h is at least 20%. In addition, UVIS and VIMS

observed features coincidently on two different occasions: simple-icicle Pywacket in α Sco

rev 13 egress and multi-icicle "Felix" in α Sco rev 29. We infer that the objects responsible

for the signal attenuation in these observations are elongated in the azimuth. α Sco is a

double star whose member stars can individually be observed in IR and UV, respectively.

Thus, an angular separation of the two observations during the rev 13 occultation means

that Pywacket was actually observed at two different inertial longitudes, first by UVIS and

then after 1.18s by VIMS, which is why the two observations are at different distances from

the core in Fig 7. Taking into account the projected speed of the occultation track and the

orbital motion of the body between two observations we obtain the actual azimuthal

separation of about 1.2 km, as compared to the 763 m radial width of the feature. This is

further evidence that such clumps of material are azimuthally elongated.

     We compare these opaque features to models of moonlet belts in Saturn's rings.

Cuzzi and Burns (1988) predict a moonlet belt surrounding the F ring, but none of the

opaque features occurred outside of the immediate region surrounding the core or

secondary-core region. BE02 predict a bimodal size distribution of moonlets in the F ring,

but the observed number (2) is inconsistent with the number of such objects predicted

from their models (cf. Figure 12). From the one measurement of the 594 m feature,

classified as Moonlet Mittens, in one of 101 independent occultation profiles, we estimate

1.5×10^4 Mittens-sized bodies in the F ring.   From Esposito, et al. (2008), we have for spherical objects

$$N_{Fring} = \frac{n_{obs}}{n_{occ}} \frac{2\pi R}{W_{obs}}$$

Equation 7

and from that we find the total mass of such objects in the F ring to be

$$M_{total \atop clumps} = \sum_{W_{obs}} \frac{\pi}{6} \rho_{clump} W_{obs}^3 N_{Fring}$$

Equation 8

where n_{obs} is the number of observed features (n_{obs}=1 for each individual feature), n_{occ} is the number of occultation profiles (n_{occ}=101), W_{obs} is the observed FWHM feature width, R is the Saturnocentric distance of the F ring (R=140221.3 km), and ρ_{clump}=0.235 g cm^{-3} is half the density of Prometheus. Likewise, 8.2 x 10^4 Sylvester-sized objects may exist in the ring, as compared to ~100 such features in the BE02 model. We estimate the total mass of Moonlets and Icicles derived from observations using Equation 7 and 8 to be 6.1 x 10^{15} kg. Such additional mass would accelerate (e.g. Null et al., 1980) the precession rate of Prometheus by 2.76 × 10^{-5} degrees per day, which would have been observable (French et al., 2003, 2006). Furthermore, that mass equates to a surface density of 800 g cm^{-2}, a 20-fold increase over the A ring. As we do not observe such a precession or surface density, we reexamine our calculation. One thing to notice is that the few largest features in the distribution contribute the most mass to the total. Table 1 lists the mass contribution from each size of object. The largest feature, number 25 Felix, accounts for 56.1% of the total extrapolated mass of spherical clumps in the F ring.   The observation of a single large Icicle may not represent the entire population of similarly-sized features in the F ring, which

contributes to an overestimate of the total mass of clumps in the ring. This large mass

estimate supports that the features are likely not spherical, rather they are elongated

clumps more like triaxial ellipsoids, as suggested by the occultation geometries earlier in

the dissertation. The features are probably flattened and have a radial width about one

tenth that of the azimuthal length, an axial ratio typical of gravitational wakes and

propeller structures in the A ring (Colwell et al., 2007; Lewis and Stewart, 2009; Salo and

Schmidt, 2010; Tiscareno, et al., 2010).

For elongated objects, W_{obs} may significantly underestimate the length of the

feature, leading to an overestimate of N_{Fring}. Since the orientation of the occultation cuts is

not random in the ring plane, and aggregations are likely more azimuthally elongated than

radial, N_{Fring} must be considered an upper limit. We generalize Equation 9 as an upper limit

of the number of bodies of a certain size in the F ring, accounting for a triaxial ellipsoid by

including a factor $\rho_{axes}=a/b=b/c$ to account for the ratio of the azimuthal length of the body

to the radial width and radial width to vertical thickness.

$$N_{Fring} \leq \frac{n_{obs}}{n_{occ}} \frac{2\pi R}{\rho_{axes} W_{obs}}$$

Equation 9

$$M_{total \atop clumps} = \sum_{W_{obs}} \frac{\pi}{6} \rho_{clump} W_{obs}^3 N_{Fring}$$

Equation 10

Equation 9 reduces to equation 7 for a sphere ($\rho_{axes}=1$). Figure 12 includes this upper limit

for $\rho_{axes}=10$. Assuming $\rho_{axes}=10$, we can now extrapolate the total mass of vertically-

flattened, ellipsoidal clumps in the F ring from this number. Using Equation 10, we find a

total mass of 6.1×10^{14} kg, equivalent to a moon of Prometheus's density with radius of 6.8

km. Assuming the radial width of the F ring is ~6 km, this mass equates to a surface density of 11.7g cm^{-2}, and would cause a change in Prometheus' precession rate of 2.76 x 10^{-6} degrees per day, which is below the detection threshold. Since the features we see are likely elongated, this resolves the mass problem we found previously for spherical clumps because there are fewer elongated clumps although each is as massive.

We report the cumulative size distribution of the number of features in the F ring, calculated using Equation 9 and the 9 features reported as Moonlets and Simple Icicles. We consider only the Moonlets and Simple Icicles because those are the feature classes that are identified with individual triaxial clumps, whereas the core class is instead identified with core-shape dynamics and the multi-icicles are likely composed of multiple simple icicles. This observed cumulative size distribution is compared to simulations of aggregation and disaggregation in the F ring by BE02 in Fig 12. BE02 simulated the evolution of the F ring including tidally-modified accretion. This led to a predicted bimodal differential distribution of bodies in the F ring, with a peak in the size at a few kilometers. It is obvious that we do not observe the bimodal distribution predicted by BE02, but rather a continuous power law n∝r^{-Q} that is best fit by cumulative power law index Q = 1.5, which is equivalent to a differential power law index of $q=Q+1=2.5$ (see the next paragraph for another method of Q-value determination). In variables we defined in this dissertation, $N_{Fring}(>w_{obs}/2) \propto (w_{obs}/2)^{-Q}$. At sizes under one kilometer, the BE02 prediction of the number of bodies is much larger than the observed distribution; however, for an azimuthal axis to radial axis ratio of 10, we only have a 0.57 chance of observing a feature in 101 occultations that would match BE02's larger size mode (width = 1-10 km), so we cannot yet compare our observations to the BE02 distribution at sizes above a kilometer. The two distributions

may be different for several reasons. First, BE02 simulate the equilibrium distribution of a model of solid, spherical moonlets in the F ring, but not loose-packed, probably-elongated aggregates of material as is indicated by Cassini observations. Also, BE02 include only tidally-modified accretion. If other processes like melting, sticking, sorting, or compaction are important, this would most likely modify the predicted distribution. Additionally, BE02 assumed a sharp threshold for accretion. If the ratio of colliding bodies' masses is large enough they fragment 100%, otherwise they accrete 100%. In Fig 12, one can see the BE02 model (solid curve) does not match the observed cumulative size distribution of our features. In fact, for the lower end of the size range sampled, BE02 predictions are significantly larger than the number UVIS detects.
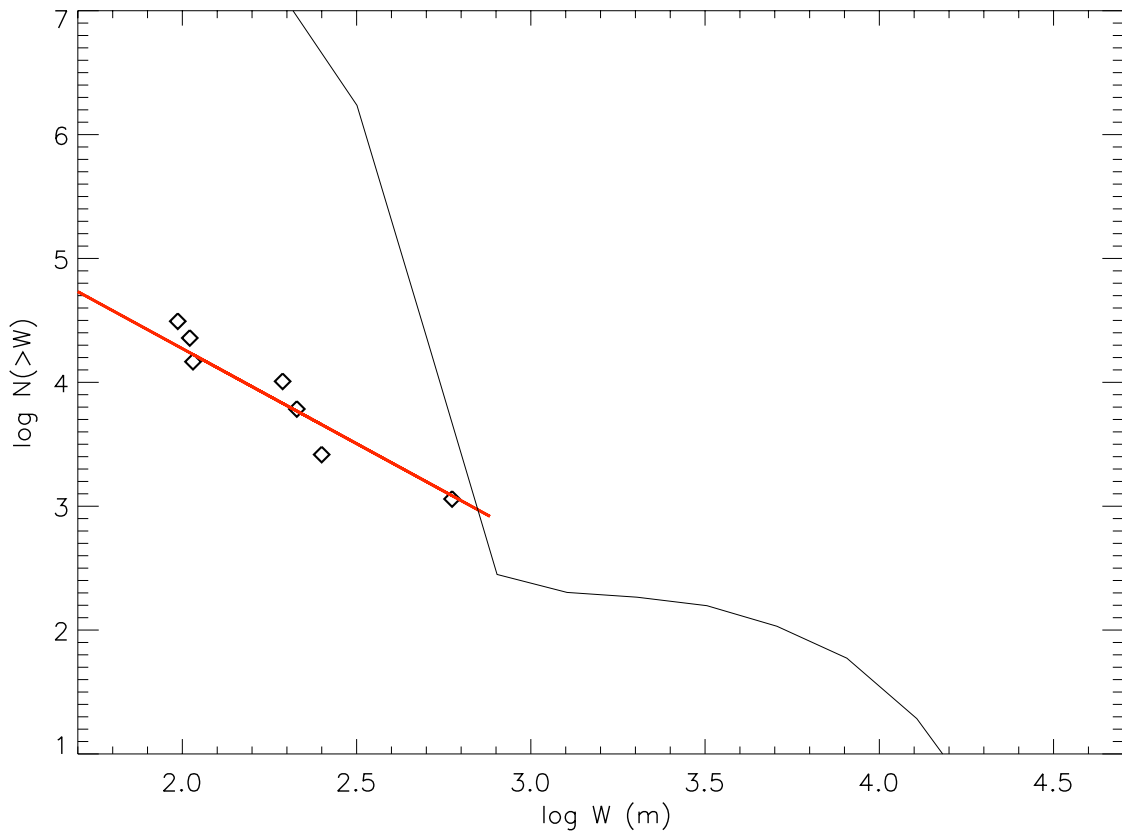
Figure 12. Cumulative size distribution of significant features in the Moonlet and Simple Icicle classes extrapolated from UVIS observations reported in this dissertation (black diamonds) and predicted by BE02 (solid line). We do not include the core class of features in this distribution because they are not comparable to the objects described by BE02. We also exclude the multi-icicles from this analysis because we describe them as accumulations of simple icicles rather than one triaxial object. The black diamonds plotted are calculated upper limits on the number of ellipsoidal clumps in the F ring (**Equation 9** for ρ_{axes} =10), accounting for observational biases due to clump elongation. The observed distribution, with a fitted cumulative power law index of Q=1.5 (overplotted in red) does not match the bimodal distribution predicted by BE02 for sizes smaller than a kilometer; however, for ρ_{axes} =10, we only have a 0.57 chance of observing a feature in 101 occultations that would match BE02's larger size mode, so we cannot yet compare our observations to the BE02 distribution at larger sizes.

We use another method to obtain the most likely differential slope q of the distribution, which was developed by Sremcevic (Meinke, et al., 2012). He first examines the raw data presented in Table 1 and then corrects the (size-dependent) correction factor due to observational biases (see below) present in equations 7 and 9. The small number of data points presents the major challenge, and he uses a simple surrogate model of power-law random numbers with the differential slope q_{raw} and sizes between *[s1,s2]* to match the data. Drawing random numbers to represent the observed distribution mimics what UVIS does; that is to say, randomly observe occultation cuts through the F ring at random longitudes and times. Numerical experiments indicate that distributions with slope *q_{raw}>2* are ruled out for two reasons. First, the distribution does not meet the data points at smaller sizes, while in the numerical experiments it is exactly the more numerous smaller sizes that are the most indicative of the underlying distribution as seen in Figure 13. Second, the drawn random numbers cluster at the smallest sizes, while if we look at Table 1 we see that sizes are almost equally distributed between smallest and largest. In Fig 13, one can see that by far the better fit is obtained with distributions with *1<q_{raw}<1.5*. This conclusion stands in both cases if we consider all data (including multi-icicles) or only the

sub-selection of moonlets and simple icicles. The shallow distributions with $q_{raw}<1.5$ are also sensitive to the upper size cut-off *s2* (contrary to $q_{raw}>2$). While it is tempting to conclude that there is indeed an upper cut-off, or at least a knee between 1 and 10km, it is best to refrain due to the scarcity of the data. The last step is to consider the bias in the detected sizes. UVIS occultations are only one-dimensional cuts across the F ring and provided that the features scale roughly the same in all three dimensions, the smallest features are hardest to detect, since the potential target is proportional to the feature size. Thus the simplest model is to consider a factor of $1/s$ that links the real F ring distribution and the actually observed UVIS data (as in eqs 7 and 9). In other words, even if there was the same number of 100 m and 1km objects in the F ring, UVIS experiment is 10 times more likely to detect 1 km objects. Therefore, we conclude that the true differential slope of the size distribution of F ring features is $2<q<2.5$, which is consistent with the simple power-law fit to the cumulative distribution in Fig 12.

Model (red):
q=2.00000
s1=0.0300000
s2=1.50000
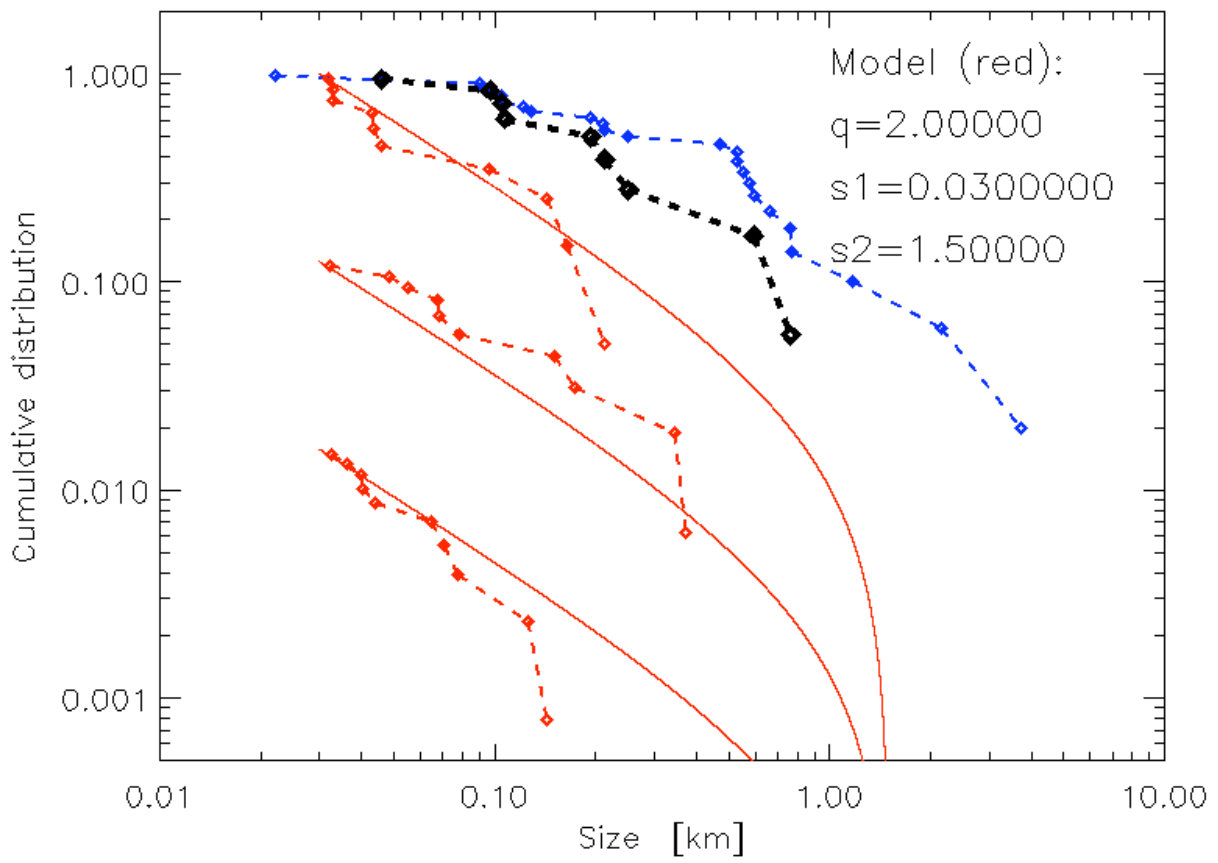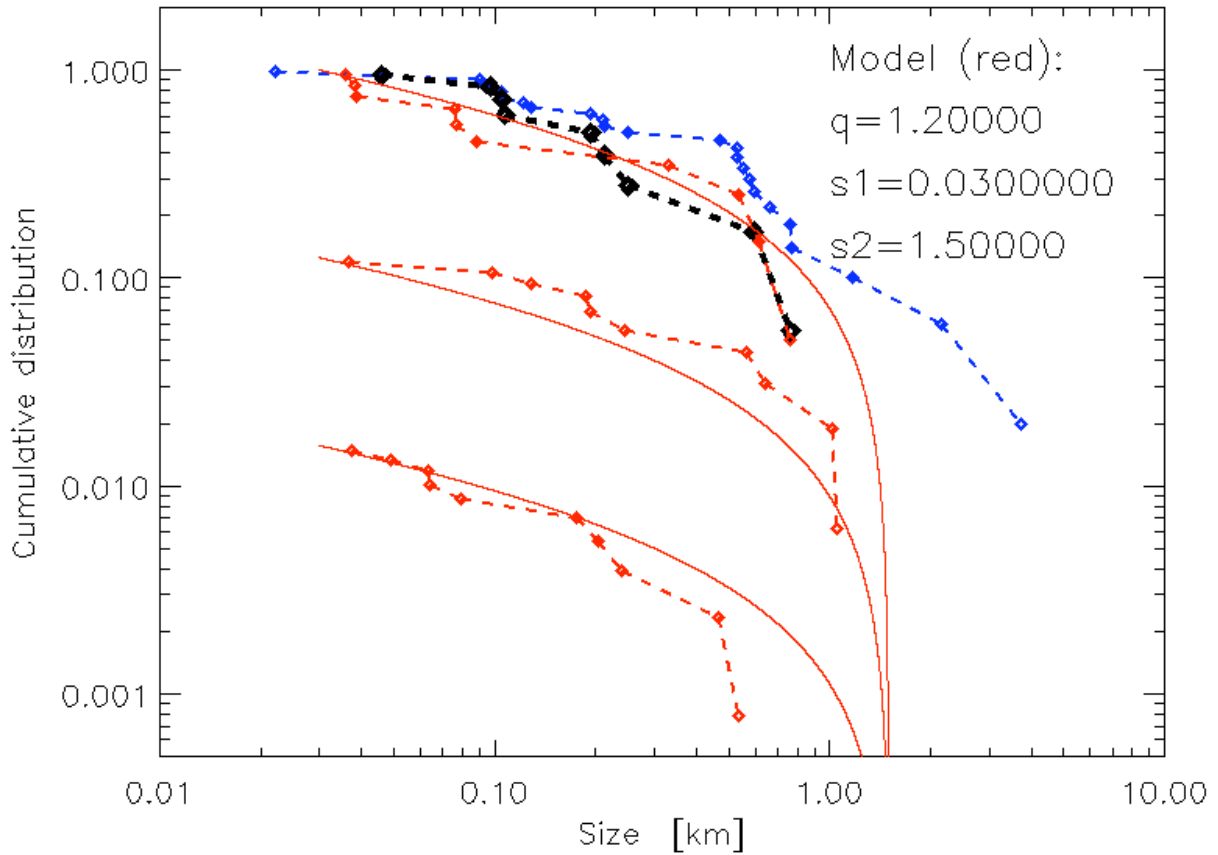
Figure 13. Comparison of observed and surrogate cumulative size distributions. Black is used for UVIS data, which includes only moonlets and simple icicles, and blue for all UVIS data (excluding Cores), while red represents the surrogate random number distribution. UVIS data points are the raw data from **Table 1**, without correcting for the *1/s* bias (eq 7). Since the cumulative distribution is insensitive to the possible binning (by the definition) we choose the bins to correspond to actual data points (UVIS or surrogate). We display three different random number realizations (from top to bottom: seeds are -7, -8, -9), each normalized to 1 and offset for ease of viewing.

A) Top panel shows surrogate random number distributions for q_{raw}=2

B) Bottom panel shows surrogate random number distributions for q_{raw}=1.2.

The sample of significant features in the Icicles and Moonlets classes sheds some light on the evolution of clumps. The largest class by far is that of Icicles. It is natural to imagine Moonlets as a possible future stage of the Icicle. Optical depth indicates clumping

because more densely aggregated material blocks more light. Thus, if looser clumps of

material (Icicles) compact into denser, less porous aggregates they may be observed as an

opaque Moonlet in an occultation. Since the Moonlet class is the smallest class with only

two observed members, it seems that this compaction state is rare. We note that when

Icicle and Moonlet optical depths are compared to the relative position of Prometheus

optical depths are largest for features located near the antipode of Prometheus's orbit

(separated from Prometheus in longitude by 180°) (Esposito et al., 2012). This rarity of

opaque Moonlets compared to clumps is consistent with Esposito's proposal that

Prometheus triggers a cycle of aggregation and disaggregation that only infrequently

results in formation of a coherent object.

2.6 **Correlation of Feature and Prometheus location**

Esposito et al (2012) propose a predator-prey system to describe the behavior of ring particles. In their model, the mean aggregate size is the prey, and the velocity dispersion is the predator. As mean aggregate size increases, so does the velocity dispersion. However, as dispersion increases, it breaks up the aggregates. Esposito et al (2012) argue that "[m]oons may trigger clumping by streamline crowding, which reduces the relative velocity, leading to more aggregation and more clumping" (see Section 3.1.5). Conversely, collisions or tidal shedding leads to disaggregation as the clumps stir the relative velocity. UVIS observations motivate and support their predator-prey model. The significant F ring features reported in Section 2.4 are among the evidence that supports the model, specifically the correlation between feature location and Prometheus' location. They conclude "that the agitation by the moons in the F ring and at the B ring outer edge drives aggregation and disaggregation in the forcing frame." Furthermore, this "agitation" by Prometheus may allow for the occasional formation of solid objects (e.g. Moonlets) from the temporary clumps (e.g. Icicles). As a result, Esposito et al (2012) predict the formation of clumps and some more permanent objects at the other perturbed regions in the rings. In this section, I review how the significant F ring features discussed previously and in Meinke et al (2012) indicate stimulated clumping by Prometheus and support the Esposito et al (2012) model.

Prometheus is the inner shepherding satellite of Saturn's F ring. Because it has a smaller semi-major axis than the F ring, it orbits at a faster speed around Saturn and encounters a specific patch of F ring material once per its synodic period of ~68 days (with respect to the center of the F ring, semi-major axis from Bosh (1996) model). Figure 14

displays the orientation of the ring and moon and defines where "leading" and "trailing" features lie with respect to Prometheus' orbital position.
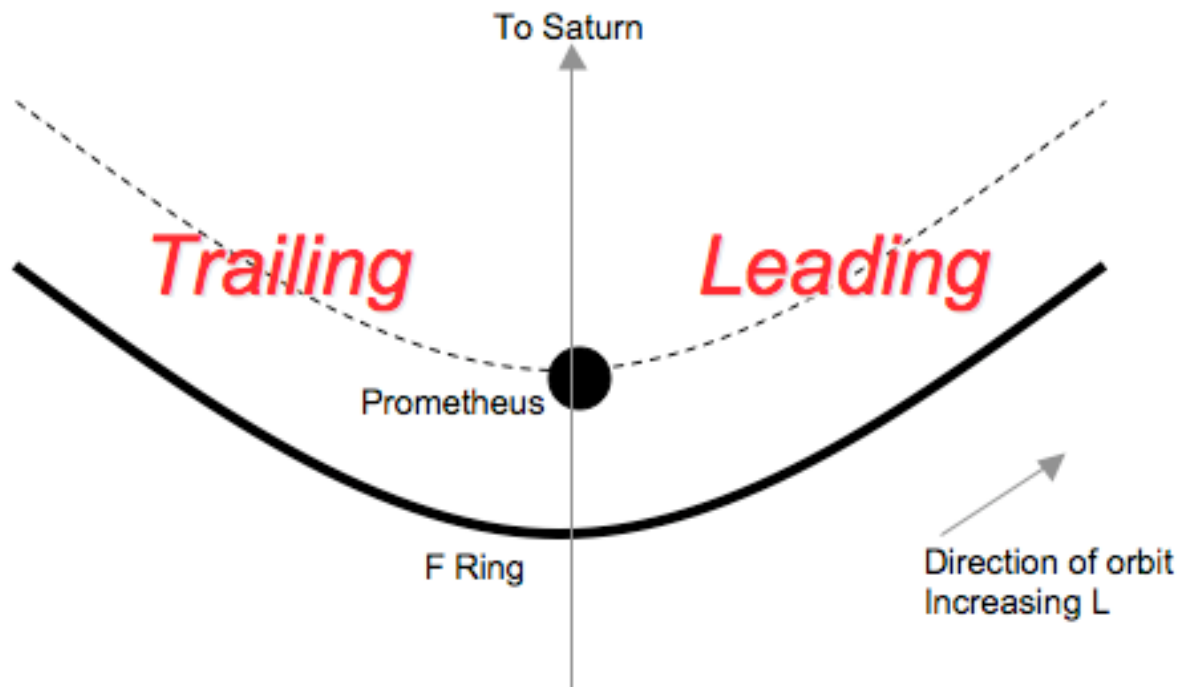
Figure 14. Schematic of F ring and Prometheus' orbits. A leading feature has not encountered Prometheus in over 34 days (half a synodic period), whereas trailing features have very recently encountered Prometheus.

A leading feature has not encountered Prometheus in over one half of a synodic period (>34 days), whereas trailing features have very recently encountered Prometheus.

Esposito et al. (2008) identified 13 statistically significant features in the first UVIS occultations. They interpreted these as temporary clumps and a possible moonlet, "Mittens", which is opaque and has sharp edges in the occultation profile. At least one of the features, nicknamed "Pywacket", was simultaneously observed by a VIMS occultation. Comparing the double star results for Pywacket, Esposito et al. concluded that it was likely elongated. The sharp edges indicate it is also significantly flattened. Meinke et al. (2012) (and Section 2.4 of this dissertation) now catalog and classify 27 features found in the first

101 stellar occultations by the F ring. Two features are opaque and candidates for solid objects: Mittens and a new feature, Sylvester. Both features's occultation profiles are consistent with a solid object surrounded by a skirt of loose material (Meinke et al., 2012). Fifteen other statistically-significant features ("Icicles") have been observed in Cassini UVIS occultations that are associated with loosely accumulated aggregates (Meinke et al., 2012). These 17 features that represent aggregations, classified as "Icicles" and "Moonlets" by Meinke et al., show significant variation in optical depths based on their location relative to Prometheus.

Optical depth is a measure of the density of material, thus we can use optical depth as a proxy for clumping. A higher optical depth indicates more clumping. Thus, we interpret higher optical depths at certain longitudinal separations from Prometheus as evidence that the moon perturbs ring material as it passes by, which in turn leads to clumping later in the synodic period.

All features are plotted versus Prometheus-relative longitude in Figure 15 along with the quadrant average optical depth, indicated with its standard deviation. In Fig 15, 0 to 180 degrees indicates leading features, whereas the other half of the range, 180 to 360 degrees relative longitude, indicates trailing features. Both the number and optical depth are enhanced at the point opposite Prometheus (antipode). Of 17 features, nine have longitude relative to Prometheus of $\Delta\lambda$= 189° ± 20. The maximum feature optical depth is found at $\Delta\lambda$= 161°. A sinusoidal fit gives a peak optical depth at $\Delta\lambda$ = 191°, but with Pearson correlation only r^2 = 0.1. With r^2 so low, there is a significant probability (p = 0.25, Taylor, 1997) that this correlation could occur purely by chance. We note that Hedman et al. (2011), using a different method to detect clumps in the F ring, find no significant

correlation with Prometheus longitude. This disagreement with our result shows the F

ring features correlation with Prometheus should be treated with caution. Even if the result

we propose here is real, then other phenomena like the eccentric Prometheus orbit which

brings it repeatedly close to the F ring may also contribute to observable structures (Beurle

et al., 2010).
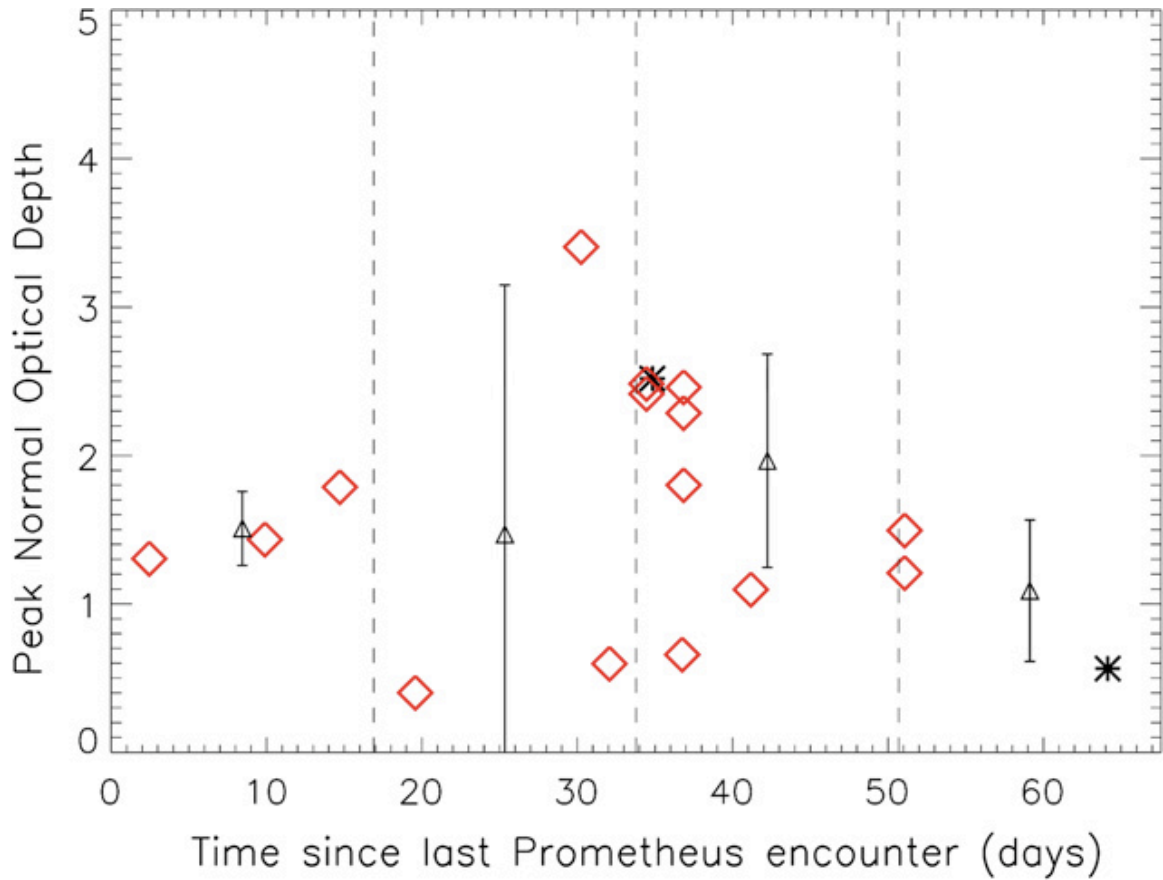
Figure 15. Optical depth of icicles and moonlets (Meinke et al., 2011) versus the time since the feature last encountered Prometheus. The synodic period (_68 days) is divided into quadrants and the mean of optical depth for each quadrant is denoted by triangles with standard deviations. Stars: moonlets. Diamonds: icicles. The measured peak optical depth is plotted. The time on the ordinate shows one complete synodic period.
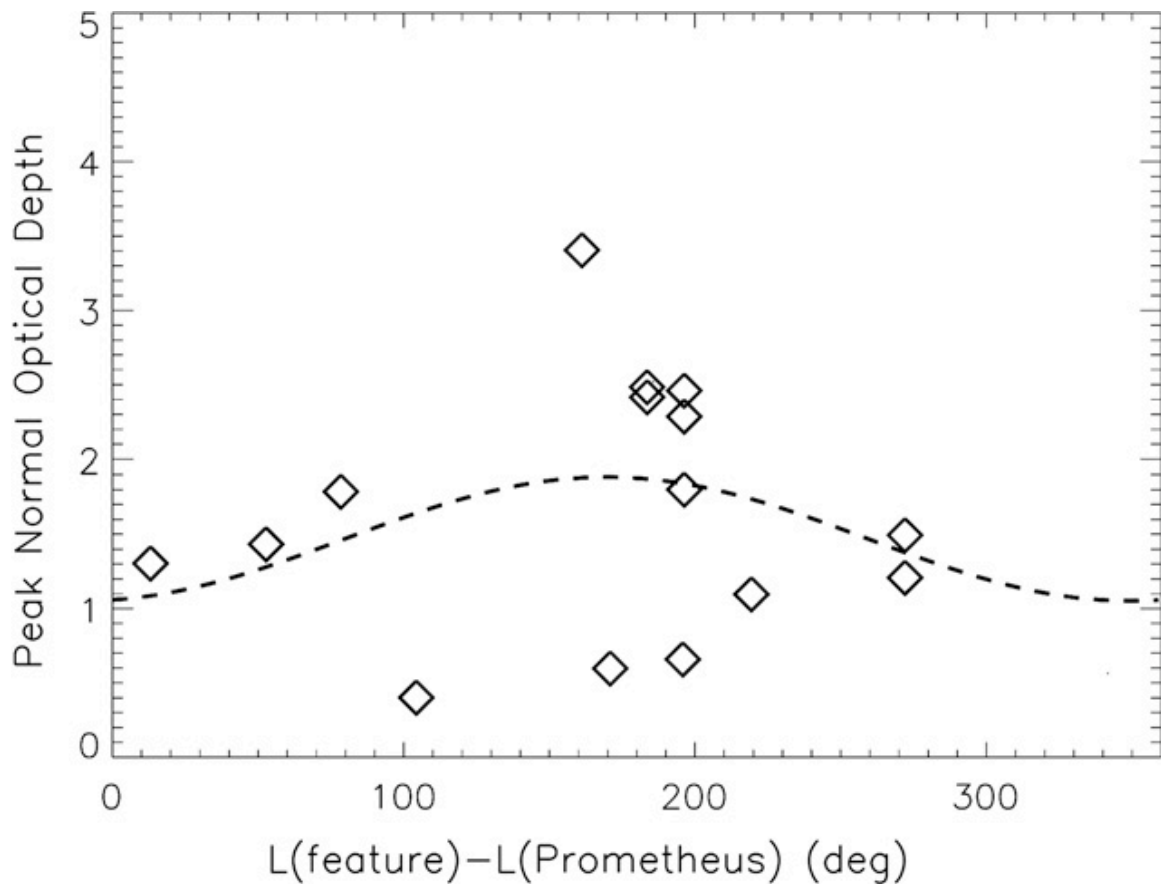
Figure 16. Optical depth of icicles as a function of their separation in longitude from Prometheus. Icicles are those reported in Meinke et al. (2011). Dashed line is the sinusoidal fit of optical depth as a function of longitudinal separation from Prometheus. The fit gives a maximum optical depth at 191° separation from Prometheus.

2.7 **Conclusion**

Stellar occultations show features in Saturn's F ring that indicate azimuthally-elongated clumping of ring material. Classification of such significant features demonstrates that while clumping may be a common process, consolidation into an opaque object, like a Moonlet, is not. The location of clumps is correlated to their relative distance from Prometheus, indicating that perturbations from Prometheus may stimulate clumping.

3. Models

3.1 Model of Accretion and Fragmentation in Saturn's F ring

Cassini UVIS has observed 17 statistically-significant features in the F ring that are associated with aggregates of ring material. Cassini Imaging has also observed larger (~few km) bodies that "disappeared" after a few orbits (Porco, et al, 2005; Charnoz, 2009). Location in the Roche zone and perturbations from Prometheus allow fragmentation to compete with accretion in the construction of aggregates on time scales of days to months. Observations and previous models motivate a more rigorous model of the evolution of aggregates in Saturn's F ring. In this section, I introduce the method for modeling the evolution of the size distribution of a collisional system, assess the resulting multimodal shape of such models, apply it to the F ring for constant and varying body densities, and discuss the model's applicability to other astrophysical collisional systems.

3.1.1 Analytical confirmation of numerical implementation

The Smoluchowski coagulation equation describes the evolution of a system of particles undergoing accretion (Smoluchowski 1916). As a general equation it can be used in many fields, and I employ it to describe tidally-modified accretion of ring material in Saturn's F ring. Given two particles of masses m_1 and m_2, the time evolution of the differential size distribution of particles, n(m,t), is:

$$\frac{\partial n(m_1,t)}{\partial t} = \frac{1}{2}\int_0^{m_1} n(m_2,t)n(m_1-m_2,t)K(m_1-m_2,m_2)\,dm_2 - n(m_1,t)\int_0^\infty n(m_2,t)K(m_1,m_2)\,dm_2$$

Equation 11

In this case, *n(m, t)* describes the differential distribution of the number density of F ring particles between *m* and *m+dm* at time *t*. The kernel, *K*, is specific to each application of the

coagulation equation because it includes the appropriate physics of the problem. In this case, I consider collisions between masses in a particle-in-a-box (PIAB) approximation. Thus, K is related to the collision frequency of the two aforementioned masses as:

$$K(m_1, m_2) = \sigma(m_1, m_2)v_{rel} = \pi(r_1 + r_2)^2 v_{rel}$$

Equation 12

For specificity, I assume v_{rel} =5 m/s because it is in the range of values representative of velocities achieved by excitation from Prometheus and Pandora (Cuzzi and Burns 1988). I also assume that the collisional cross section is simply the geometrical cross section.

In order to treat the coagulation equation numerically, I discretize it. I use a differential approach to this model rather than the incremental approach used in similar models (Canup and Esposito (1995), Barbara and Esposito (2002)). As such, I calculate the kernel corresponding to each mass pairing $K_{i,j}$. I consider $n(m,t)$ as a continuous distribution, but m_i is a discretization such that m is a vector of mass values of particles. In the following equations, $n(m_i, t) = n_i$, and i_{max} or j_{max} are the total number of bins in the mass vector. Also, I include the bin sizes Δm_j in the summation:

$$\partial_t n_i = \frac{1}{2}\sum_{j=0}^{i} n_{i-j}n_j K_{i-j,j}\Delta m_j - n_i\sum_{j=0}^{i} n_j K_{i,j}\Delta m_j$$

Equation 13

To further demonstrate n(m, t), I calculate N and M here, which are the total number density of particles in the system and the total mass density in the system, respectively.

$$N = \sum_{i=0}^{i_{max}} n_i \Delta m_i$$

$$M = \sum_{i=0}^{i_{max}} n_i m_i \Delta m_i$$

Equation 14

Solving Equation 13 in successive, variable time steps (see later description), I model the

evolution of the size distribution as a function of time:

$$n_i(t) = n_i(0) + \int_0^t \left(A_{Gain} + A_{Loss} + F_{Gain} + F_{Loss} \right) ds$$

Equation 15

The preceding equations yield $\dfrac{d \left(\sum_{i=0}^{i_{max}} n_i m_i \Delta m_i \right)}{dt} = 0$. That is to say, system mass is conserved,

as should be the case because I assume no sources or sinks of ring material.

The numerical method undertaken here benefits from a variable time step in order

to accurately track the evolution of the equation. I accomplish this by setting a threshold on

the amount by which *n(m,t)* is allowed to change over one time step. As I found in checking

my numerical solutions against the analytical solutions (see below), I balance run time with

allowed evolution by choosing a threshold of 1%. If the threshold is larger than about 5%,

a small perturbation in the initial distribution may suddenly evolve to a larger depletion or

addition than it realistically would, yielding an unrealistic final size distribution. On the

other hand, if the threshold is too small, evolution speed is hampered and the computing

time becomes prohibitive. The only real difference between time steps computed using a

1% threshold and a .0001% threshold is run time.

In order to confirm that my method is sound mathematically and numerically, I perform a check on my numerical model of the coagulation equation. Such a check gives me confidence in my results and helps improve my accuracy (or how well the numerical model solves the coagulation equation) and mass conservation through a tune on the parameters governing the variable time step.

Silk and Takahashi (1979) (ST79 from here on) use the coagulation equation to model the stages of fragmentation of a collapsing molecular cloud. As tests they solve the coagulation equation to find exact or approximate analytical solutions that exist for certain kernels in the equation. I use their "approximate solution to the velocity-averaged coagulation equation"(Eq 11) for three different kernel types: one is constant, the other two are particle-mass dependent. Their analytical solutions to the equation serve as a preliminary check on the accretion portion of my numerical implementation. The "testing process" I employ consists of three steps. First, I compare the analytic solutions given in ST79 using the same initial conditions and scaling for the size distribution of particles. Examples of my replications of figures from the papers are shown below (Figure 17 and 18). Next, I apply my own binning scheme for the mass range appropriate to my investigation. By producing the analytical solution to my parameters, I determine the shape, evolution, and scale of the numerical solution to be expected. Lastly, I run my model to numerically solve for my parameters using the analytically solvable kernel and initial mass distribution function condition. Comparing this numerical solution to the analytical solution, I verify the efficacy of my code.

The first analytically solvable kernel for the coagulation equation is a constant, $K(m_1,$
$m_2)=K_0 = 1$. ST79 derive the solution for a continuous mass function by Laplace transform
technique and an initial value of $n(m,0) = N_0 \delta(m - m_0)$ to find a solution of the form

$n(m,t) = \dfrac{N_0}{m_0} g(t)[f(t)]^{\frac{m}{m_0}-1}$, where

$a \equiv \dfrac{1}{2}K_0 N_0$

$g(t) = (1+at)^{-2}$ **Equation 16**

$f(t) = 1-(1+at)^{-1}$

 ST79 set $N_0=10^5$ (the initial total number density of particles), $K_0=1$, m_0 is the smallest

mass bin ($m_0=1$ kg in ST79 and $m_0=2 \times 10^9$ kg in my model, but since it's plotted in terms of

mass ratios on a log scale, this value is not important), and t is time. Here, $g(t)$ and $f(t)$ are

factors defined by ST79 to simplify the equation for $\overline{n}(s,t)$, the Laplace transform of $n(m,t)$,

before applying the inverse transform to find the solution of the coagulation equation,

$n(m,t)$. Figure 17b demonstrates my reproduction of this analytical result with the

parameters I use in my model. That is to say, I have only plotted the analytical solution

ST79 reports in order to assure that it matches and that it is available to compare to my

numerical solution. I have repeated this process with two other analytical solutions.

Time Relaxation of Mass Function, My Parameters

$K=1$, $N_o = \delta(m-m_o)$

61
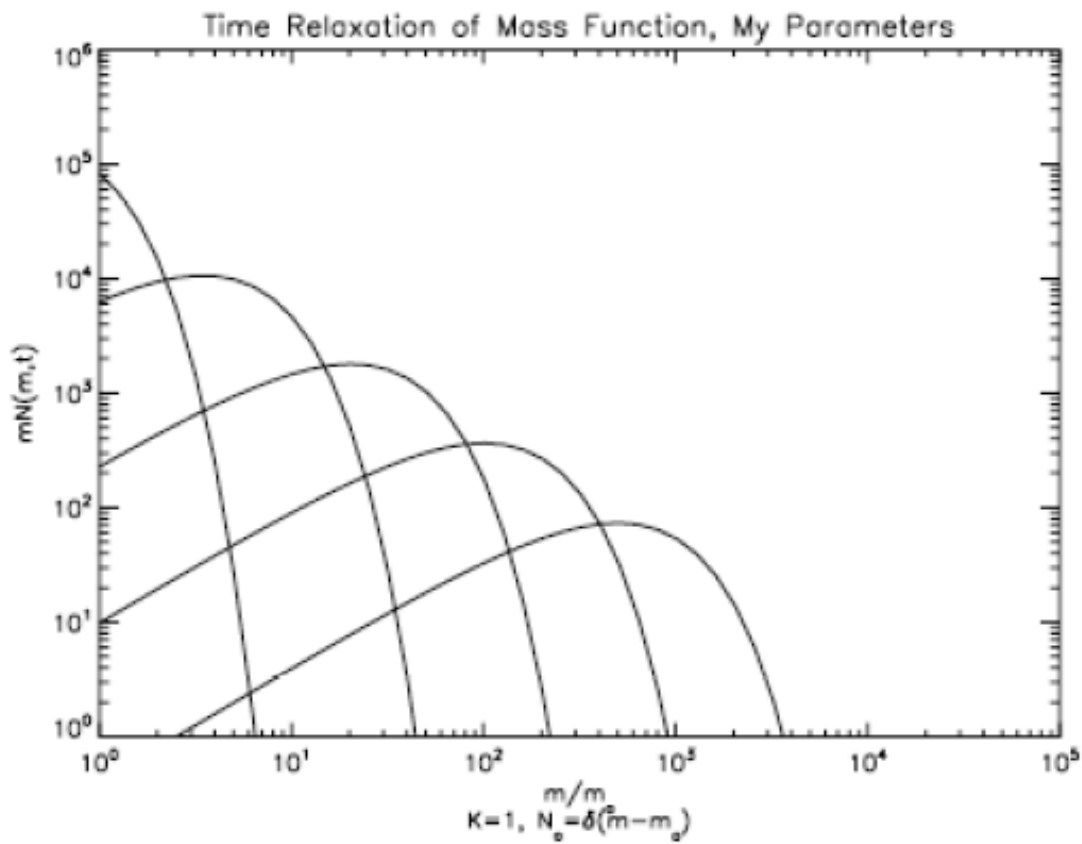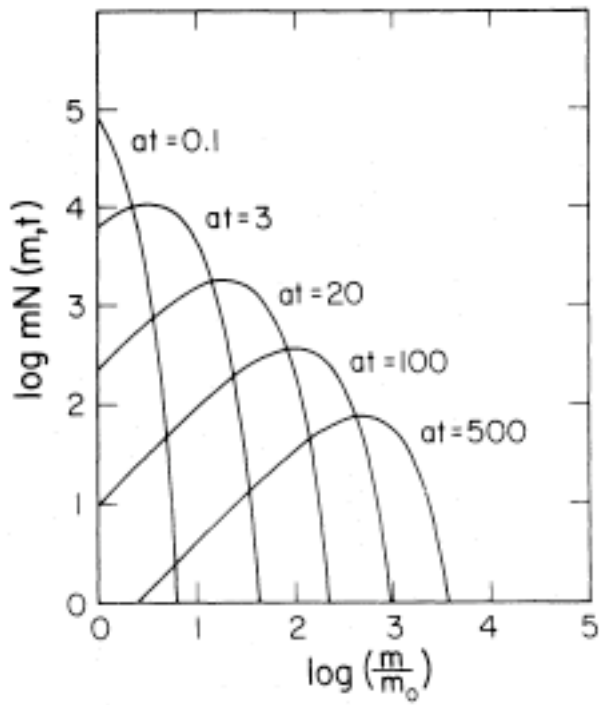
Figure 17 a) from Silk and Takahashi (1979), Figure 1a. The analytical solution to the coagulation equation with a mass-independent constant-valued kernel for various values of the product a * t. Mass function relaxation plotted when $K_0=1$ and $N_0=10^5$. b) This investigation's reproduction of the analytically derived mass function using the mass range and parameters of this investigation (and BE02). It is evident that the two figures are identical because the plots scale with mass ratio.

The second analytically solvable kernel for the coagulation equation is additively mass dependent, $K(m_1, m_2) = K_0(m_1 + m_2)$. Again, ST79 take the Laplace transform of the coagulation equation to derive the solution for a continuous mass function. In this case, the initial value of the size distribution was $n(m,0) = N_0 \delta(m - m_0)$ and the long-time limit is

found to be $n(m,t) \sim C(t) m_0^{1/2} m^{-3/2} \exp\left[-\frac{m}{m_0} \frac{C^2(t)}{2N_0^2} \right]$, where

$$C(t) = N_0 e^{-K_0 M t}$$

$$M \equiv \int_0^\infty m n(m,t) \, dm$$

Equation 17

In this case, $N_0 = 10^5$, $K_0 = 1$, $C(t)$ is the total number density of particles at time t, and M is the total mass density of the system. The analytical and numerical solutions of this case are plotted in Figs 18 and 20.

Test 2: Time Relaxation of Mass Function, My Parameters

$K=(mass)^{\lambda}$, $N_o^o = \delta(m-m_o)$
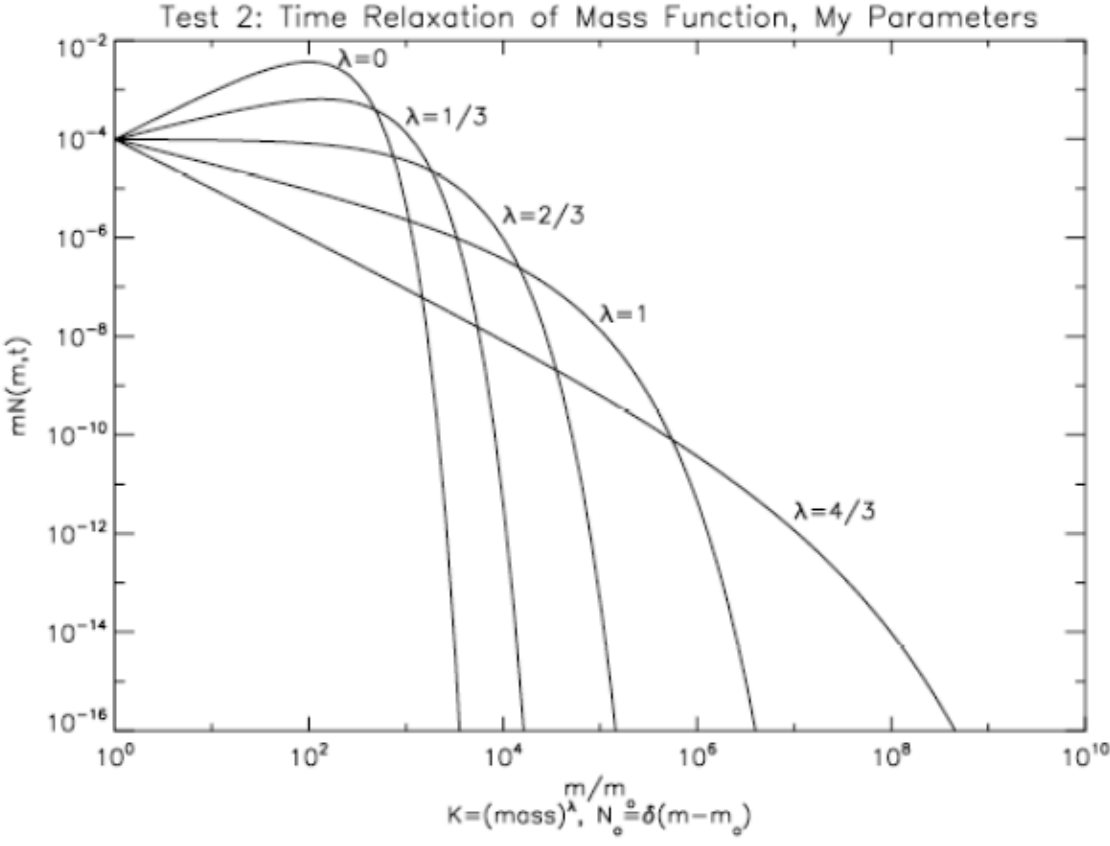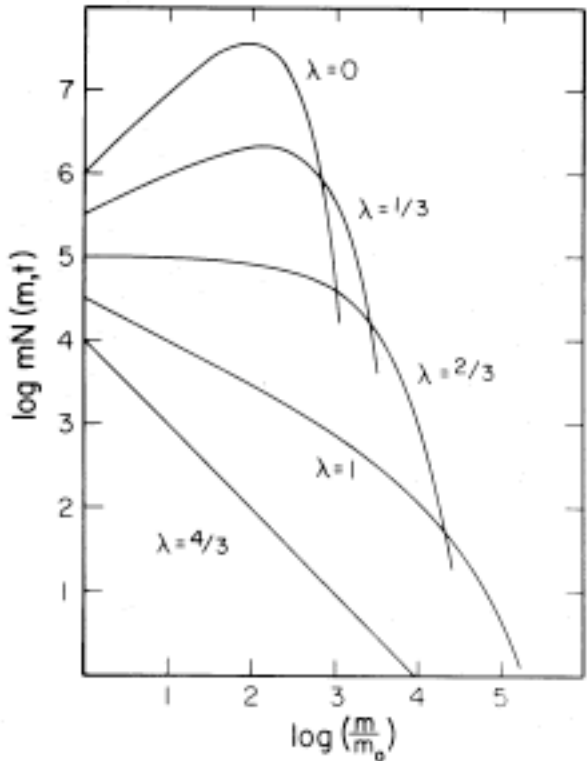
Figure 18 a) from Silk and Takahashi (1979), Figure 2. The analytical solution to the coagulation equation with a power-law mass-dependent kernel for various values of the exponential power. Mass function relaxation plotted when $K \propto (\text{mass})\lambda$ and $N_o = 10^5$. b) This investigation's calculation of the analytically derived mass function for the mass range and parameters of this investigation. I have normalized the total mass density of the system in a different way (such that the total optical depth of the F ring is 0.1), which is why they are not of the same scale as a).

The third analytically solvable kernel for the coagulation equation has a power law mass-dependence, $K(m_1, m_2) = K_0(mass)^\lambda$. Again, ST79 set the initial distribution to be a delta function, $n(m,0) = N_0 \delta(m - m_0)$, and find

$$n(m,t) \approx \frac{N_1}{m_0}\left(\frac{m}{m_0}\right)^{-\lambda/2} g\left[\left(\frac{m}{m_0}\right)^{\lambda/2} t\right]\left\{f\left[\left(\frac{m}{m_0}\right)^{\lambda/2} t\right]\right\}^{\frac{m}{m_0}-1}, \text{ where the definition of } a \text{ in } g(t) \text{ and } f(t)$$

in the previous case is replaced by $a_1 \equiv \frac{1}{2} N_1 m_0^\lambda K_0$. Figure 18 displays the resulting mass functions for different values of λ and my reproductions of those analytical solutions. This case is most relevant to my investigation because the kernel in my model reflects the collision frequency of particles and is thus dependent on the cross section of interaction. Cross section is proportional to r^2, or $m^{2/3}$; therefore, $\lambda=2/3$ is the appropriate check of my numerical solutions.

The analytical results using my model's parameters are consistent with the ST79 results; therefore, the next step in assessing the efficacy of my numerical model is a comparison of the analytical and numerical solutions. Figure 19a, b, and c display the comparison for each test. For a quantitative comparison, I compare the

mean mass ($\langle m \rangle = \frac{M}{N} = \frac{\int_0^\infty mn(m,t)\,dm}{\int_0^\infty n(m,t)\,dm}$) of the numerical and analytical number density

64

distributions at the same time step. In the case of a constant kernel (Figure 19a), the

$\frac{\langle m \rangle_{num}}{\langle m \rangle_{ana}} = 0.945$. A ~5% difference is a close match for these purposes (see discussion

below). For the case of an additive kernel (m_1+m_2), $\frac{\langle m \rangle_{num}}{\langle m \rangle_{ana}} = 0.567$. This case is not as good

of a match as I would like (Figure 19 b), but in the ST79 approximation, the analytical

solution given is actually a long-time limit, so although this comparison was done at ~ 1 yr,

the fact that the numerical does not match the analytical by a factor of 2 is not surprising.

The test most relevant to my purposes in the F ring model is the power-law solutions (Fig

19c), specifically when $\lambda=2/3$. At a time step threshold of 1% (that is, $n(m,t)$ not allowed to

vary by more than 1% per time step), the numerical solution's mean mass is 1.24 times that

of the analytical solution. I believe this agreement to be good enough to continue on to

apply the numerical technique to my problem. I define "good agreement" under a couple of

conditions. First, I consider this a "good agreement" because of the effects of having such

steep initial and final distributions. Such a steep distribution allows orders of magnitude

difference between the two results at the same mass even though they appear to be

narrowly separated in the plot. This could result in the mean mass of the numerical

solution being a considerable fraction larger than the analytical solution, so any numerical

technique being 25% larger still matches the analytical solution well. Also, the "good

agreement" assessment comes from the implementation of the initial conditions. For all

three analytical solutions, the initial distribution is a delta function. Several ways exist to

numerically simulate a delta function, including a narrow Gaussian or one bin filled with N_o

particles, surrounded by several bins with a small fraction (say 1%) that of the central bin.

After experimenting with such options, I chose to simply fill the first mass bin with N_o particles. I believe this also contributes to a non-exact match because as you can see, the m_o bin of the numerical size distribution solution remains slightly spiked. Furthermore, ST79 cannot solve analytically for a power-law kernel; rather, they approximate by expansion of

$$\left(m_1^{1/3} + m_2^{1/3}\right)^2 = m_1^{1/3}m_2^{1/3}\left[2 + \left(\frac{m_2}{m_1}\right)^{1/3} + \left(\frac{m_1}{m_2}\right)^{1/3}\right] \approx m_1^{1/3}m_2^{1/3}$$

Equation 18

Evaluating the appropriate kernel numerically will result in a difference. Finally, from private communication with N. Albers, it seems that it is not unusual for the numerical solution to "outrun" the analytical solution. This is probably due to the factors discussed above.

In addition to matching the analytical solution, the numerical solution should also conserve total mass density, which all cases do to better than .005% per time step. However, it is interesting to note that the numerical solution does seem to overtake the analytical solution and slightly gains overall system mass as it evolves. This is experienced in other such numerical comparisons (N. Albers, private communication). Figure 20 displays the numerical solution (solid lines) and analytical solution (dashed lines) for the $m^{\lambda=2/3}$ case at different times in the evolution.

Comparison of Analytic to Numerical Solution

Test 1

Comparison of Analytic to Numerical Solution

Test 3

67

Comparison of Analytic Solution to Numerical Solution

Mass/Mo
for Test 2, λ=2/3
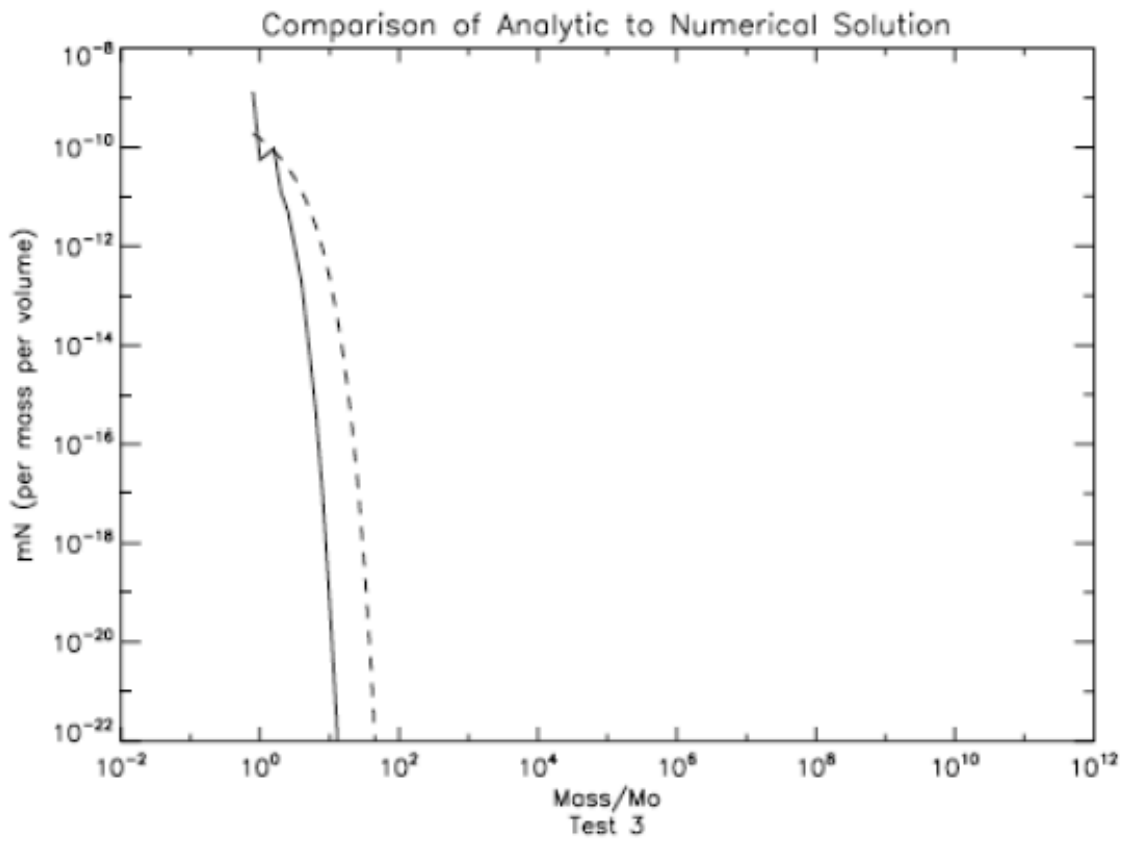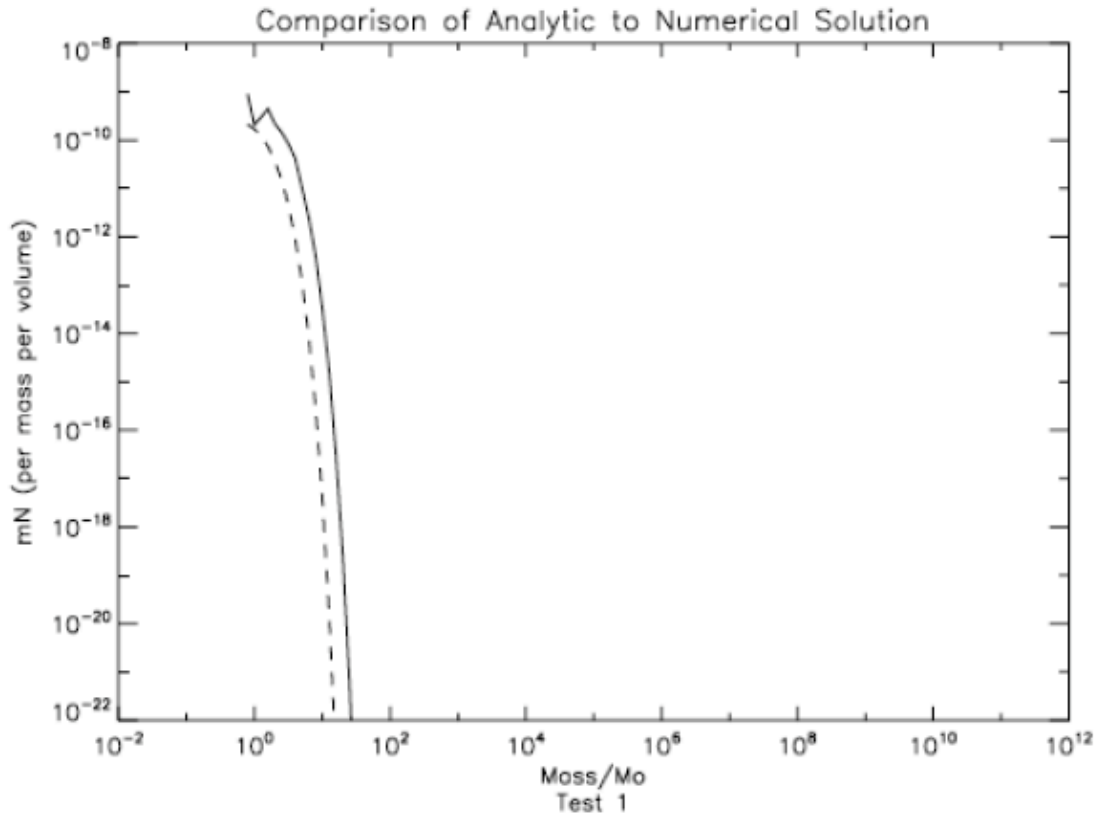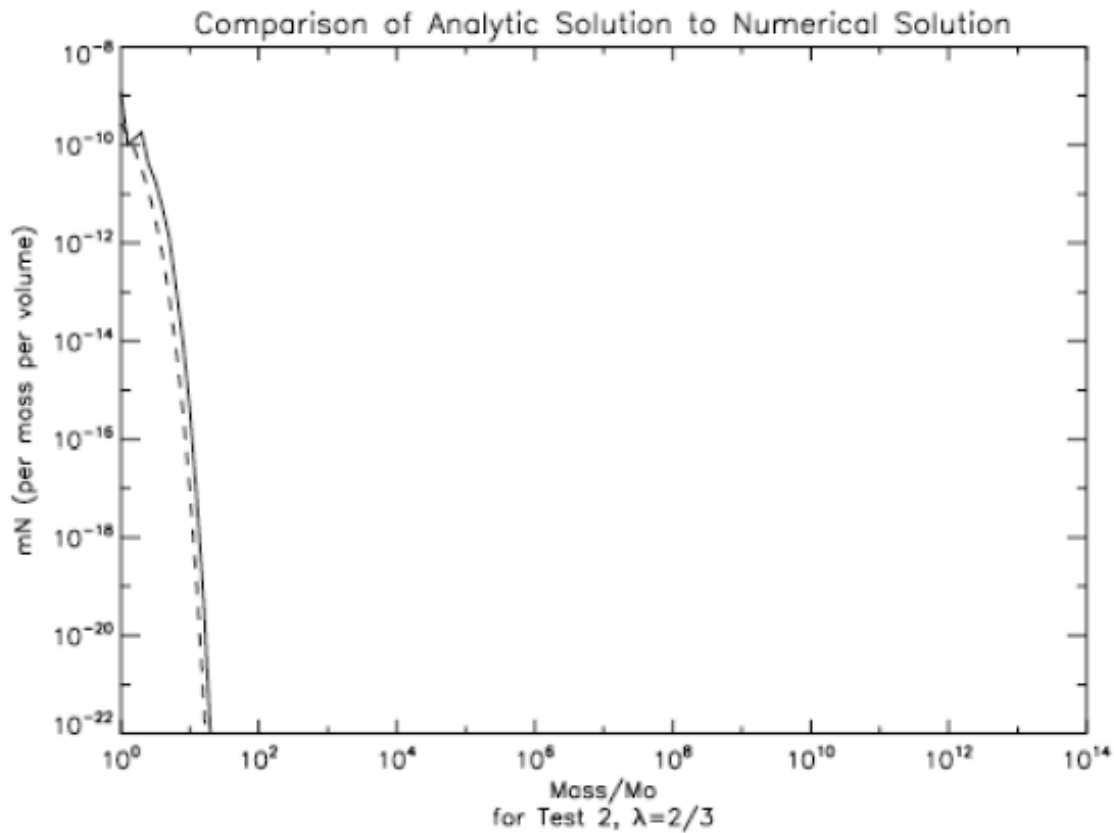
Figure 19. Comparison of analytical to numerical solutions to the coagulation equation when plotted as mass functions. The solid line is the numerical solution, the dashed line is the analytical solution at the same time. a) K=constant, b) K=m1+m2, c) K=(mass)λ. The agreement of the analytical to numerical solution for a power law mass dependent kernel in c) is good ($<m_{num}>/<m_{ana}>$=1.24). This is the most important part of this "testing" process, since K=(mass)2/3 is most like the kernels I use to describe F ring dynamics.
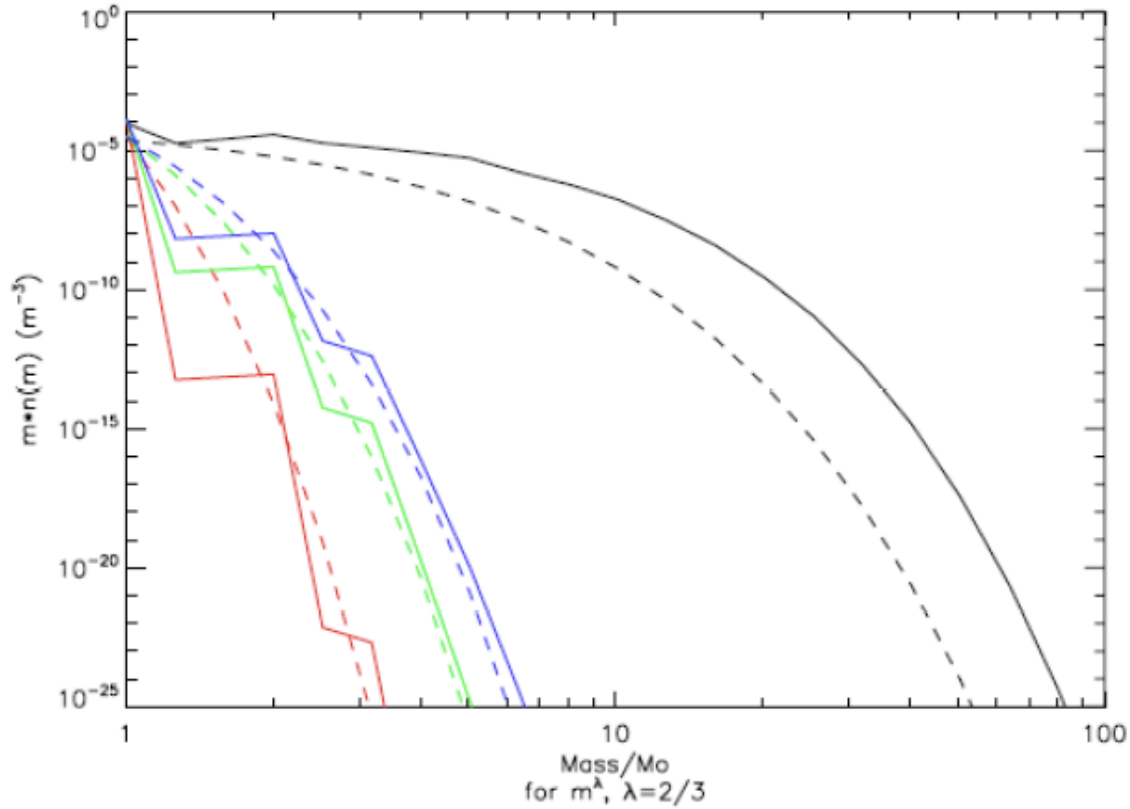
Figure 20 The evolution of the size distribution using the power-law kernel, with $\lambda=2/3$. The solid lines are numerical solutions and dashed lines are analytical solutions. As the system evolves, the numerical solution "outruns" the analytical solution. Times for the pairs of lines are (by color): t=6.6 s (red), t=1.3x10^5 s (green), t=2x10^6 s (blue), and t=9x10^9 s (black).

To accurately model the evolution of the size distribution of material in Saturn's F ring, it is necessary to account for the major processes involved in the evolution of material. Thus, in addition to coagulation, I include fragmentation in this model. The fragmentation equations are similar in form to the coagulation equation, but the gain term includes factor, P_f, to account for the redistribution of disrupted mass (Spahn et al. 2004, N. Albers private communication).

$$\frac{dn(m_1,t)}{dt} = \frac{1}{2}\int_0^{m_1} P_f K_{1,2} n_1 n_2 \, dm_2 - n_1 \int_0^\infty K_{1,2} n_2 \, dm_2 \qquad \textbf{Equation 19}$$

where $K_{1,2}$ is the collision frequency (σv_{rel}/volume), as described in the "Particle in a Box"

approximation used in the "Coagulation Equation," Section 3.1.1. The function P_f, which

describes the redistribution of disrupted fragments, is the number of fragments between m

and m+dm produced in a collision of bodies m_1 and m_2. The normalization of this function

is $\int_0^{m_{LF}} mP_f\, dm = m_1 + m_2$. Redistribution of material requires an assumption as to the

largest fragment resultant from a disruptive collision (m_{LF} in the normalization equation),

as disrupted mass is redistributed up to this mass limit. Krivov et al (2005) calculate the

largest resultant fragment from impact energy considerations with an upper limit of

$0.5m_{target}$. I adopt the assumption that the largest fragment is 0.5 m_{target}. In testing the

numerical code for this addition to the coagulation equation, I use a P_f that places all

disrupted material into only 1 size bin and a P_f that redistributes according to a power law.

The function I adopt for this investigation, however, redistributes the total colliding mass

according to a power law.

Regardless of redistribution function, the steady-state mass distribution of the

collisional fragmentation cascade is $n(m)=Am^{-\alpha}$, where $\alpha=11/6$ (Tanaka et al, 1996;

Dohnanyi, 1969). Thus, I test the fragmentation portion of the numerical code for various

initial conditions and redistribution functions and find that when the model allows all

bodies to fragment upon collision, the distribution evolves to the predicted $n(m)=Am^{-\alpha}$

distribution, where $\alpha= (\nu+3)/2=11/6$ given that ν is the collision rate mass dependence

($\nu=2/3$ for geometric cross section) (Figure 21).
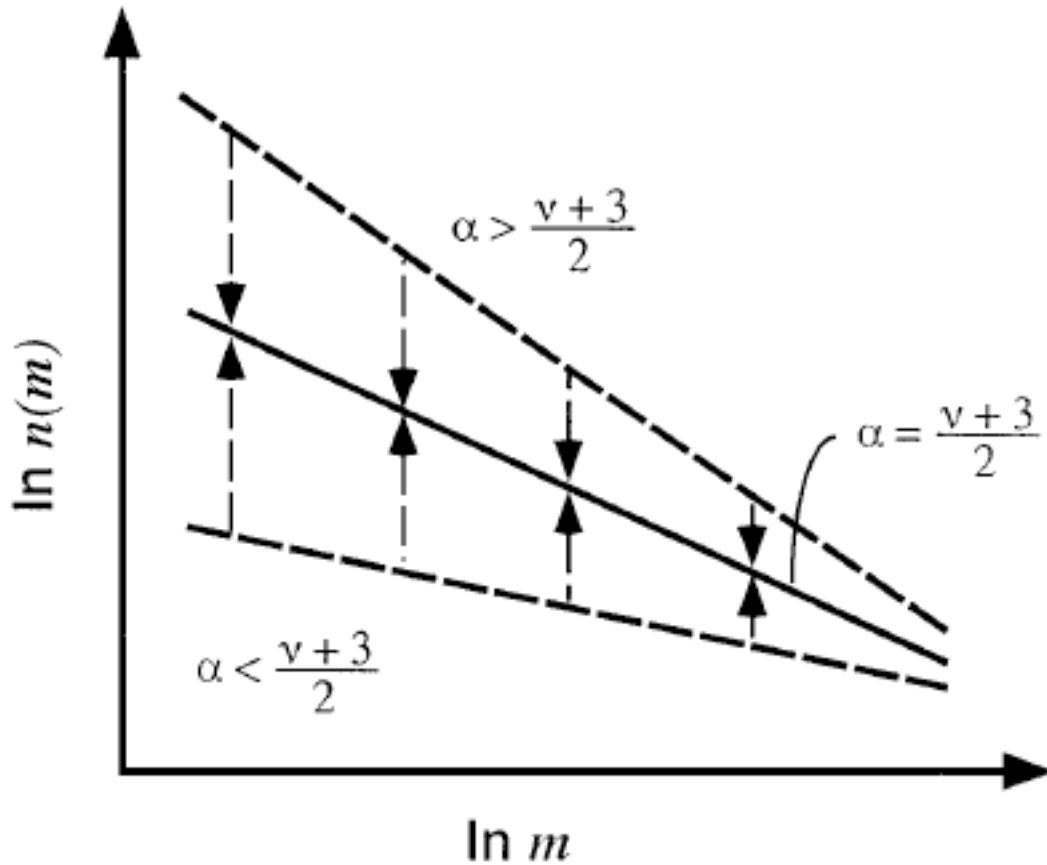
Figure 21 From Tanaka et al. (1996), Figure 1. "A schematic picture of the evolution of the mass distribution for the self-similar collision cascade. All mass distributions approach the power law solution with the exponent α=(ν+3)/2."

Now that fragmentation is included in the physics, four terms give a complete description of the mass evolution of the number density of particles in the F ring. A_{Gain} and A_{Loss} describe gain and loss, respectively, due to accretion, while F_{Gain} and F_{Loss} are the gain and loss terms due to fragmentation.

$$\frac{dn(m,t)}{dt} = A_{Gain} - A_{Loss} + F_{Gain} - F_{Loss}$$

$$A_{Gain}(m,t) = \frac{1}{2} \int_{0}^{m-m_0} n(m_1,t)n(m-m_1,t)K(m_1,m-m_1)dm_1$$

$$A_{Loss}(m,t) = n(m,t) \int_{m_o}^{\infty} n(m',t)K(m,m')dm'$$

$$F_{Gain}(m,t) = \frac{1}{2} \int_{m_1=0}^{\infty} \int_{m_2=0}^{m_1} n(m_1,t)n(m_2,t)K(m_1,m_2)P(m,m_1,m_2)dm_1\, dm_2$$

$$F_{Loss}(m,t) = n(m,t) \int_{0}^{m} n(m',t)K(m,m')dm'$$

Equation 20

With a description of the competing processes in the F ring, it is important to determine

which collisions result in accretion and which in fragmentation. The mass ratio, μ, of

colliding particles forms the basis for this determination. When evolving the system in

terms of masses (constant mass density), the critical mass ratio of colliding moonlets above

which accretion occurs and below which objects fragment is μ_{crit}. In the numerical solution

of this problem, a certain collision type is then treated by the appropriate terms in the

equation. In the Barbara and Esposito (2002) model, μ_{crit} = 100 and only applies to

moonlet-moonlet collisions. All moonlet-dust and dust-dust collisions result in accretion.

The numerical implementation of accretion and fragmentation processes in my

model is consistent with the aforementioned analytical solutions to the coagulation

equation and collisional cascades. These comparisons are rigorous tests of the numerical

kinetic code for F ring evolution including accretion and fragmentation processes. Next, I

combine accretion and fragmentation processes in an attempt to reproduce the result of

Barbara and Esposito (2002).

3.1.2 **Introduction of the binary accretion model**

With over 101 UVIS-observed occultations by the F ring, we can construct the distribution of clumps of material in the ring. As discussed in the last section, this observed distribution is not consistent with the Barbara and Esposito (2002) (hereafter BE02) model. In this section, I develop a model of the F ring distribution's evolution with an eye toward explaining the shallow power law slope of the observed distribution.

The motivation for this model of the evolution of the size distribution of the F ring is to expand upon the simple model of BE02 because it does not match the observed distribution of clumps in the ring (Meinke et al 2012). BE02 simulate the evolution of tidally-modified accretion in the F ring. They numerically model a Markov process of colliding bodies and find a final state that is a bimodal distribution of ring particle sizes (Figure 22). The mode of larger bodies predicts a moonlet belt of kilometer-size bodies in the F ring. Cassini UVIS observes such a belt (Meinke et al., 2009), but the size distribution is a power law with differential index $q \sim 2.5$ (Meinke et al 2012), rather than the predicted bimodal. This difference may be due to the modeling assumptions of BE02, as discussed in the "Observations" section. BE02 simulate steady-state distribution of solid, spherical moonlets in the F ring, not loose-packed, probably-elongated aggregates as indicated by UVIS observations. In addition, BE02 only consider the effects of tidally-modified accretion, not other processes like adhesion and compaction that are probably important in the collisional evolution of the F ring and that would modify the distribution. Also, BE02 has a sharp threshold for accretion requiring 100% accretion if the ratio of colliding bodies' masses is sufficient, 100% fragmentation otherwise.
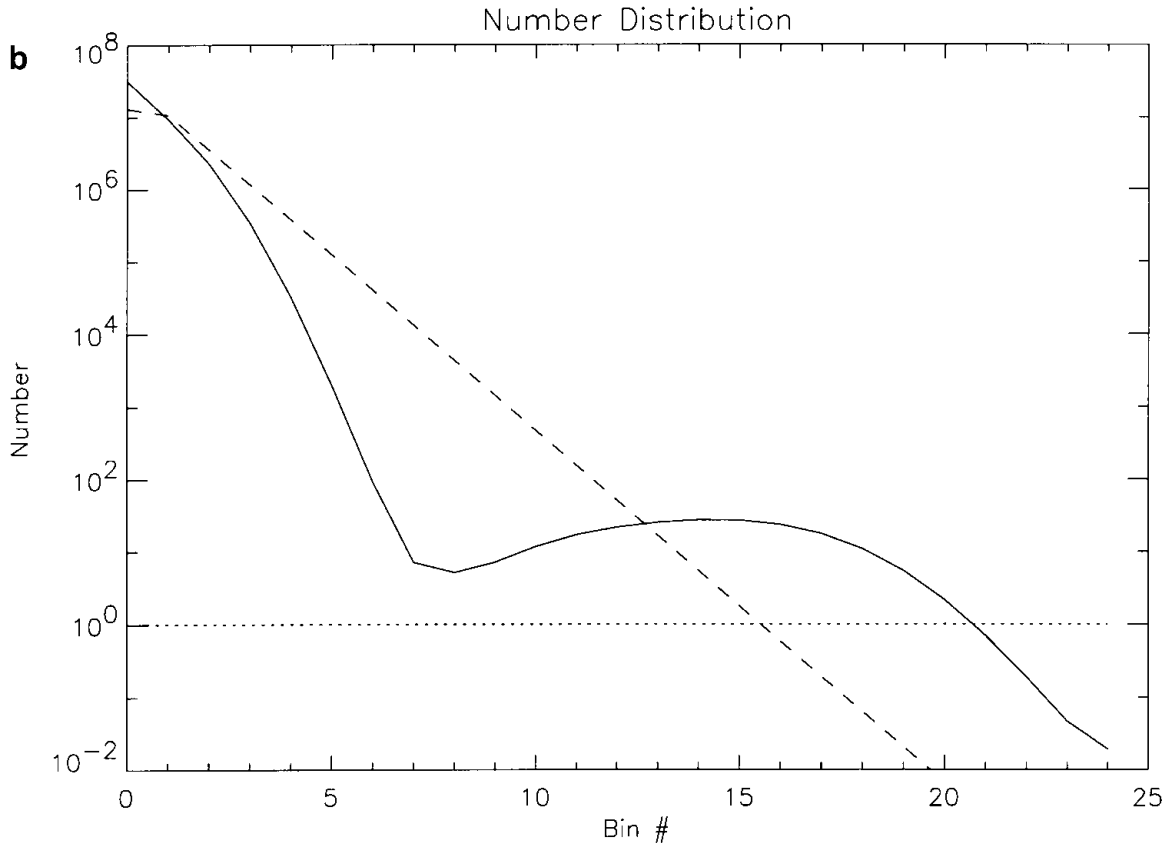
Figure 22. From Barabara and Esposito (2002), Figure 5b. "Initial continuous power law distribution (dashed) and final bimodal distribution for …number, where q_{ejecta}=3.1 and overall F-ring mass has been modified such that the average optical depth remains equal to 0.1. The dotted line …marks unity." Bin 0 is the "dust bin" of objects 10 μm to 100 m, and bins 1-25 are logarithmically spaced by a factor of $\sqrt{2}$ over a size range of r=100 m to 20 km.

A bimodal distribution has been the expected state for F ring material in the literature (Canup and Esposito, 1995; BE02), but such a distribution is inconsistent with the observations (Meinke et al. 2012). In development of a new numerical model of F ring evolution, I take an approach different from BE02. The evolving system can be described using a kinetic approach, specifically the velocity-averaged coagulation equation (Spahn et al., 2004).

The Smoluchowski coagulation equation (Eq 11) describes the evolution of a system of particles undergoing accretion. As previously described in this section, I adapt the

74

coagulation equation to describe tidally-modified accretion of material in Saturn's F ring.

Given two colliding bodies, the time evolution of the differential size distribution of bodies,

$n(m,t)$, is:

$$n(m,t+dt) = n(m,t) + \frac{dn(m,t)}{dt}dt$$

$$\frac{dn(m,t)}{dt} = A_{Gain} - A_{Loss} + F_{Gain} - F_{Loss}$$

$$A_{Gain}(m,t) = \frac{1}{2}\int_0^m n(m_1,t)n(m-m_1,t)K(m_1,m-m_1)dm_1$$

$$A_{Loss}(m,t) = n(m,t)\int_{m_o}^{\infty} n(m',t)K(m,m')dm'$$

$$F_{Gain}(m,t) = \frac{1}{2}\int_{m_1=0}^{\infty}\int_{m_2=0}^{m_1} n(m_1,t)n(m_2,t)K(m_1,m_2)P(m,m_1,m_2)dm_1\,dm_2$$

$$F_{Loss}(m,t) = n(m,t)\int_0^m n(m',t)K(m,m')dm'$$

Equation 21

In this case, $n(m, t)$ describes the differential distribution of the number density of F ring

bodies between m and $m+dm$ at time t. $P(m, m_1, m_2)$ is the redistribution function for post-

collisional fragments. I use the PIAB approximation to calculate the kernel K such that it is

related to the collision frequency of the two aforementioned masses as in Equation 12.

Furthermore, I assume $v_{rel} = 5$ m/s (Cuzzi and Burns 1988) and that the collisional cross

section is simply the geometrical cross section.

In order to treat the coagulation equation numerically, I discretize it. I use the

following discretized definitions of the accretion and fragmentation gain and loss terms:

$$A_{Gain \atop i} = \frac{\Delta n_{i=j+k}}{\Delta t} = \sum_{k=0}^{k_{max}} \sum_{j=0}^{k} n_k n_j K_{k,j} \Delta m_k \Delta m_j$$

$$A_{Loss \atop i} = \frac{\Delta n_i}{\Delta t} = n_i \sum_{j=0}^{i} n_j K_{i,j} \Delta m_j$$

$$F_{Gain \atop i} = \frac{\Delta n_i}{\Delta t} = \sum_{k=0}^{k_{max}} \sum_{j=0}^{k} n_k n_j K_{k,j} P_{i,j,k} \Delta m_k \Delta m_j$$

$$F_{Loss \atop i} = \frac{\Delta n_i}{\Delta t} = n_i \sum_{j=0}^{i} n_j K_{i,j} \Delta m_j$$

Equation 22

The model handles mass conservation, distribution evolution, and variable time step as described in Section 3.1.1 (Equation 14 and 15).

In development of a new numerical kinetic model of F ring evolution, I consider the possibility that the bimodal distribution is a consequence of a sharp accretion/fragmentation threshold resulting in a final distribution that is generally multimodal. In working with Nicole Albers (private communication) and using BE02 parameters and initial conditions, we could not independently reproduce their result. A multimodal distribution results, the general trend of which follows the Dohnanyi-predicted $q=11/6$ power law for a collisionally-evolved system. Upon investigation, we discovered the separation of successive modes is dependent on the value of μ_{crit}. The first trough in the distribution occurs where $m/m_0 = \mu_{crit}$ (Figure 23). When we extend the size scale or reduce μ_{crit}, more modes appear. Examination of the BE02 results shows that the trough in the BE02 quasi-equilibrium distribution (Figure 22) occurs where $m/m_0 = \mu_{crit}$. Perhaps the BE02 model suffered such effects but the size scale used coincidently cut off after one oscillation, conveniently giving the appearance of the expected bimodal result.
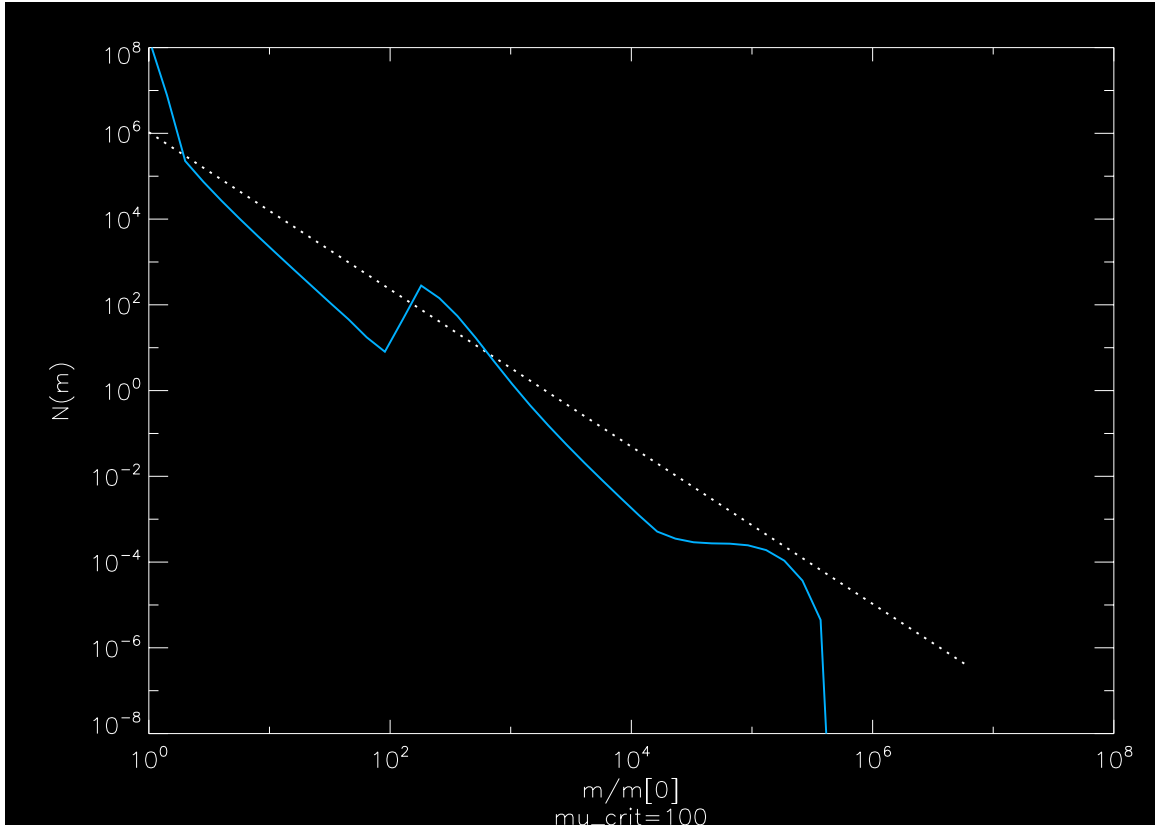
Figure 23. Quasi-steady state differential distribution. The blue solid curve is the modeled differential distribution for the prescribed parameters of the BE02 model. The dotted white line is the initial distribution. The modeled distribution is multimodal, not bimodal like the BE02 result. The break before the first mode occurs at $m/m_0 = \mu_{crit}$.

3.1.3 **Assessment of the multimodal distribution**

The constant-density model produced from my numerical implementation of the Smoluchowski coagulation equation (Equation 22; Spahn, et al., 2004) produces a result that is multimodal. When one encounters it for the first time, he or she might suspect some sort of numerical effect at work in the discretization of the coagulation equation for this behavior. In fact, the behavior appears to be an evenly spaced pattern of oscillations overlaying the Dohnanyi power law index of q=1.83 for a collisionally-evolved system. Until recently, only one other author attempted to understand the origin of what he terms a "wavy pattern." This section details my exploration of this behavior, develops an equation for the body sizes where modes exist for a set of input model parameters, and provides an explanation of why these modes develop. Further, we explain why these modes appear in dynamical evolution models of other collisional systems such as the Asteroid and Kuiper belts.

As discussed in the last section, an attempt to model tidally-modified accretion in the F ring to compare to BE02's bimodal distribution resulted in a quasi-steady state distribution that had more than two modes, each of which encompassed a smaller size range of bodies than the large mode from BE02. The multimodal result of my model was similar to other astrophysical size distributions discussed in the literature, but only one author explored the origin of the behavior or sought to quantify it based on parameters of specific models in which it appears. Campo Bagatin, et al. (1994) coin the term "wavy pattern" to describe the multimodal behavior of their model of the Main Asteroid Belt (Figure 23). They state that it is the use of a small-size cutoff of a distribution undergoing fragmentation that results in this "wavy pattern." A cutoff at either end of a size

distribution is a necessity of any numerical model of such a system.   For a small-enough

dynamical resolution, the size range of the distribution can be computationally expensive

for several decades of size. Campo Bagatin, et al. argue, however, that this is not simply a

numerical effect. Rather, small-size cutoffs exist in nature due to size-dependent erosion

processes.   There is a long history of observing asteroids. There exist several populations

of asteroids, which can be studied as independent collisional systems, namely near Earth

asteroids (NEAs), the main belt asteroids, and various groups of Trojans. The observations

of some of these populations are statistically complete to small sizes, so we focus on the

observed size distributions of these Solar system bodies (Ceplecha, 1992; Jedicke, et al.,

2002; etc). For example, Ceplecha (1992) reports the observed distribution of 10-100 m

Near Earth Asteroids is multimodal (Figure 24). NEAs have a sharp small-size cutoff in

their distribution because bodies are preferentially removed from the system up to a

critical size.   In addition, other dynamical systems may have size cutoffs due to other

erosion processes such as Pointing-Robertson drag, YORP effect, Yarkovsky effect, or

planet-crossing unstable orbits (Paddack, 1969; O'Keefe, 1976; Radzievskii, 1954; Öpik,

1951; Poynting, 1903; Robertson, 1937). Morbidelli et al. (2009)'s more recent model of

post-accretion Main Asteroid Belt results in a multimodal distribution. Fraser (2009)

develops a model of the Kuiper belt size distribution that he uses to explain "rollover" in

the observed distribution at $r\sim25$-60 km and finds what he refers to as a "divot" in the

distribution at that size.   A "wavy pattern" manifested in a natural collisional system

outside Saturn's rings and other models thereof confirms such behavior in our model;

therefore, I argue a physical basis exists for such evolution outcomes and it is not simply a

result of our numerical implementation. Thus, I continue my investigation by characterizing the pattern more quantitatively.
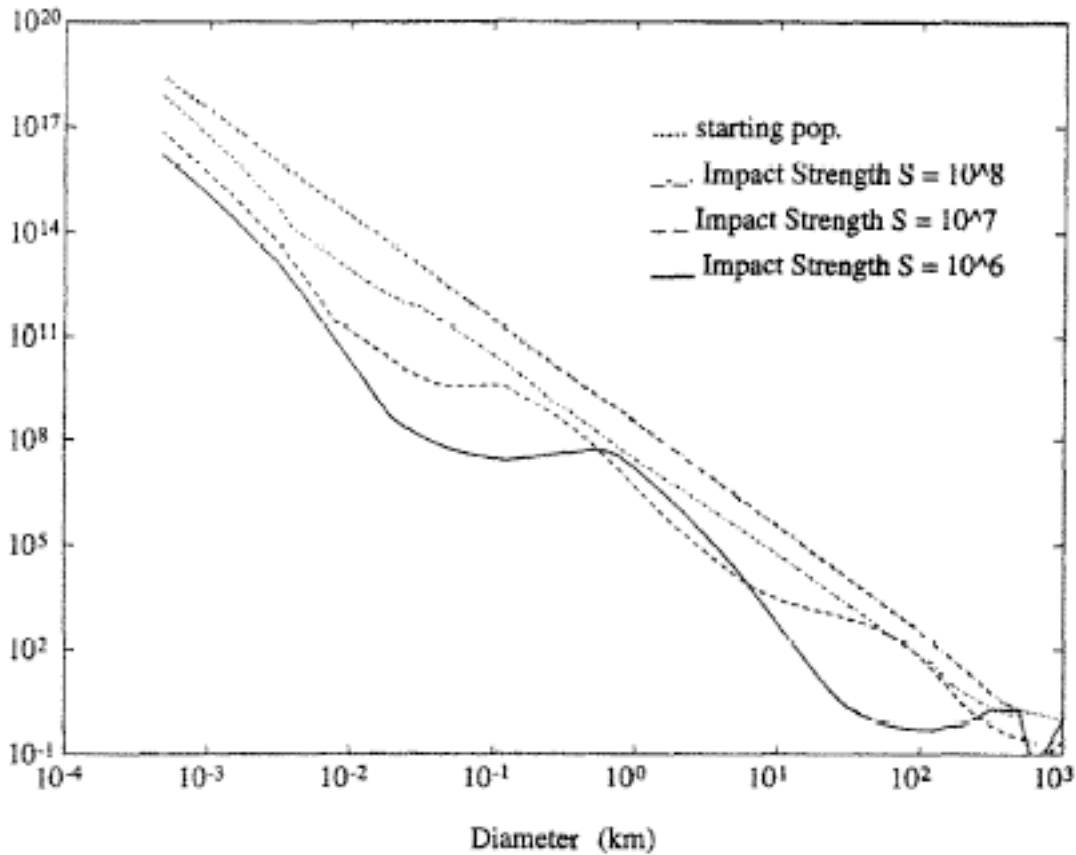
Figure 24. From Campo Bagatin et al. (1994), Figure 1. "The size distribution resulting from the numerical simlulations described in the text, with the population of every size bin plotted vs the corresponding diameter in a log-log diagram (logarithmic incremental diameter plot). Size-independent collisional response parameters have been used, with a small-size cutoff set at about 50 cm (64 bins spanning a factor 2 in mass each). Three different values for the impact strength S (in erg cm^{-3}) have been tested." Their simulated distribution of the asteroid belt evolves into a multimodal distribution as my model does. Also, the location of modes is dependent on the colliding material's strength properties.
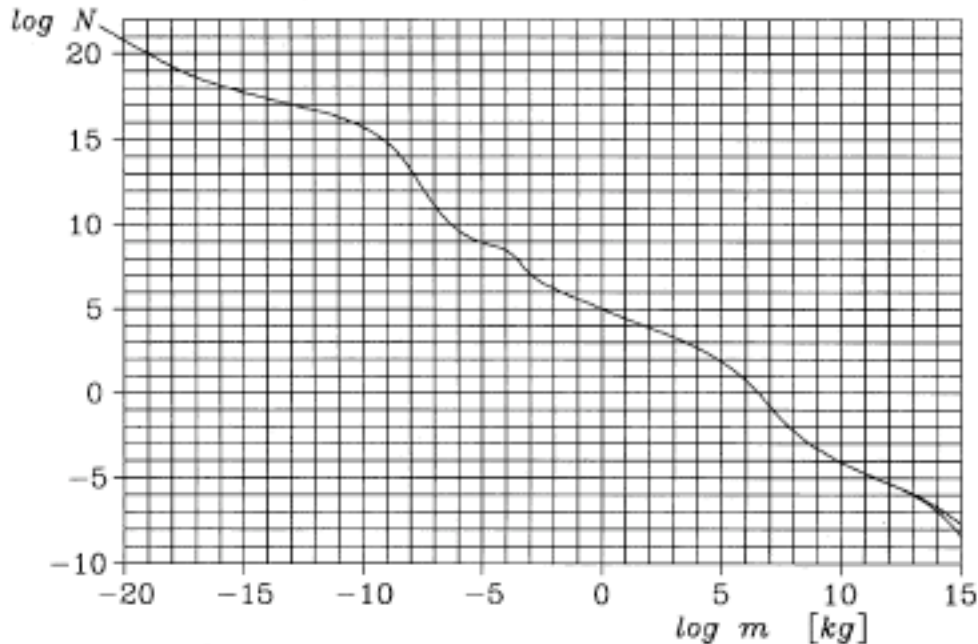
Figure 25. From Ceplecha (1992), Figure 1. "Logarithm (base 10) of the cumulative number, N, of interplanetary bodies with mass equal or greater than m coming to the Erath is plotted against logarithm of the mass . The lower curve at log m = 14 and 15 is from the data of Shoemaker et al (1990); the upper curve is the adopted average." These observed data comprise a multimodal distribution, consistent with modeled distributions of collisional systems.

Morbidelli et al's post-accretion asteroid belt grows 100-1000 km bodies from sub-meter particles via accretion without growing through intermediate sizes, hence the title "Asteroids were born big." Weidenschilling (2011) finds, however, that a primordial population of <0.1 km bodies could reproduce the "bump" or mode at D~100 km in the current observed distribution of Main Belt asteroids due to "a transition from dispersion-dominated runaway growth to a regime dominated by Keplerian shear." Not only does this disagree with the Morbidelli et al model, it also shows a system can evolve to a multimodal distribution without fragmentation, which was required for Campo Bagatin et al's explanation. These models of the same system achieve multimodal patterns that match observations via differing mechanisms; meanwhile, Campo Bagatin et al (1994) postulated

that the "wavy pattern" arose from a sharp cutoff of the distribution at small sizes, another mechanism still. I explore what causes the multimodal behavior of the F ring distribution model results and compare that to the previously postulated ones, in an effort to reconcile the underlying physical mechanisms of collisional systems evolution.

To understand the multimodal distribution results of my model, I examine the input parameters. The initial setup of the model is based on the setup of BE02, excluding their dust bin. Thus, binary collisions occur between bodies in a size range of 100 m to 20 km in radius with initial distribution $n_{initial} \propto m^{-qi}$, where the initial differential power law index q_i =1.83, Dohnanyi's derived value for a collisionally-evolved system. Tidally-modified accretion in the F ring region allows for complete (100%) accretion of incoming mass if the mass ratio of colliding bodies $\mu=m_1/m_2$ is larger than a critical mass ratio μ_{crit} =100 (Ohtuski 1993, Canup and Esposito 1995) and complete fragmentation if $\mu<\mu_{crit}$. Fragmented material is redistributed among all bins smaller than half the mass of the larger colliding body as $n_{ejecta}=m^{-qej}$, where the redistribution differential power law index q_{ej}=1.23 is reported from laboratory studies of ice collisions (Stewart and Ahrens).

Simple checks of the model during the initial construction showed that the initial distribution does not affect the quasi-steady state outcome. The size range of bodies in the system also has no qualitative effect, the system still evolves to a multimodal distribution in time. The power law index describing the redistribution of fragments does affect the final distribution, but does not suppress multiple modes (cf. Figure 38). Considerable quantitative differences are evident when the accretion conditions are modified, however.

Tidally-modified accretion depends on the critical mass ratio μ_{crit} above which colliding bodies will accrete and below which they will fragment. For the location of the F

ring (a=140221.3 km (Albers et al. 2012)), μ_{crit}=100 (Canup and Esposito 1995). Complete

accretion or fragmentation of colliding mass on either side of this threshold makes for a

sharp transition in the dynamics of the system. To examine how the value of μ_{crit} affects the

evolved distribution, I compare the model with different values of μ_{crit}. Figure 26 shows the

evolution of the model with μ_{crit}=100, 10^3, 10^4, and 10^5. The first mode of each of these

results is at a different value of m/m_0. Upon initial inspection, the value of m/m_0 at which

the first mode appears is near the value of μ_{crit} for that particular model. Further, one can

see the second modes appear at a value of m/m_0 roughly equal to μ_{crit}^2. Over a sufficiently

large size range compared to μ_{crit}, one can observe many subsequent modes spaced at

regular intervals of m/m_0 compared to the prescribed value of μ_{crit} for that model. In order

to quantify this phenomenon, I found by visual inspection the value of m/m_0 at which the

peak value of each mode occurs for distributions over various size ranges and values of

μ_{crit}. In Figure 27, I plot the value of m/m_0 of a mode versus the μ_{crit} for that simulation. I

fit the points for each mode to find the simple power-law index that relates μ_{crit} to the

location of that particular mode. These are overplotted as solid lines in Fig 27. The

following fits were derived:

$m(mode1)= m_0\ \mu_{crit}^{1.1}$

$m(mode2)= m_0\ \mu_{crit}^{2.3}$

$m(mode3)= m_0\ \mu_{crit}^{3.3}$

$m(mode4)= m_0\ \mu_{crit}^{5.7}$

Equation 23

Obviously, all simulations have a mode 1, but the appearance of subsequent modes

depends on the size range of the distribution; therefore, I have the greatest number of data

points for mode 1 at 23, and Fig 27 shows how good the fit to mode 1 location is. For mode

2, 13 points are found for the fit; mode 3 had 6 and mode 4 had 2. Mode 1 and mode 2

location fits are the most relevant because the peak $n(m,t)$ for mode 3 is over ten orders of

magnitude lower than for mode 1, so the probability of observations is drastically reduced.

It is important to note here that the width of a mode is dependent on the resolution of the

model. Larger bins distribute bodies over a wider range of sizes, and the mode is not as

well resolved, as seen in Fig 27. A bin spacing of $\sqrt{2}$ between masses provides sufficient

resolution for a discretized approach, which is why I use it for the fits reported in Equation

23 and from this point onward in my model, as do most other modelers.
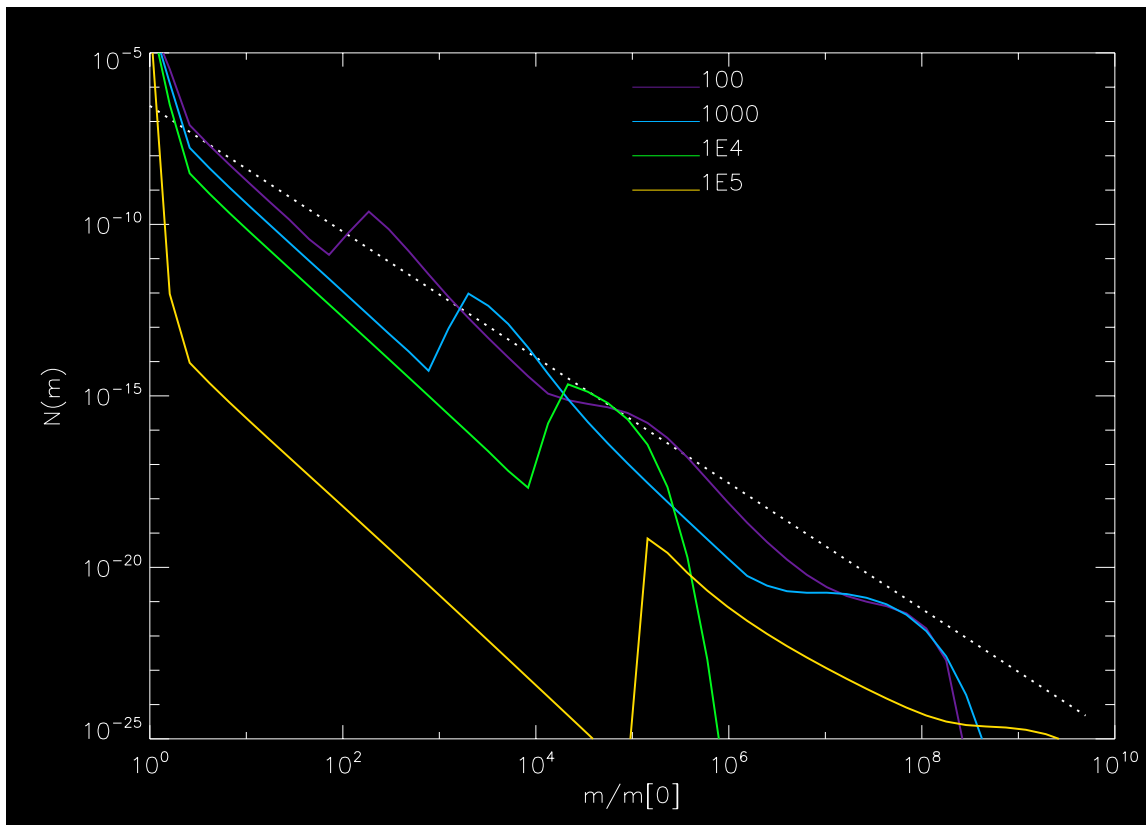
Figure 26. The evolution of the model with μ_{crit}=100, 10^3, 10^4, and 10^5. The first mode of
each of these results is at a different value of m/m_0, which approximately corresponds to
each model's μ_{crit} value.
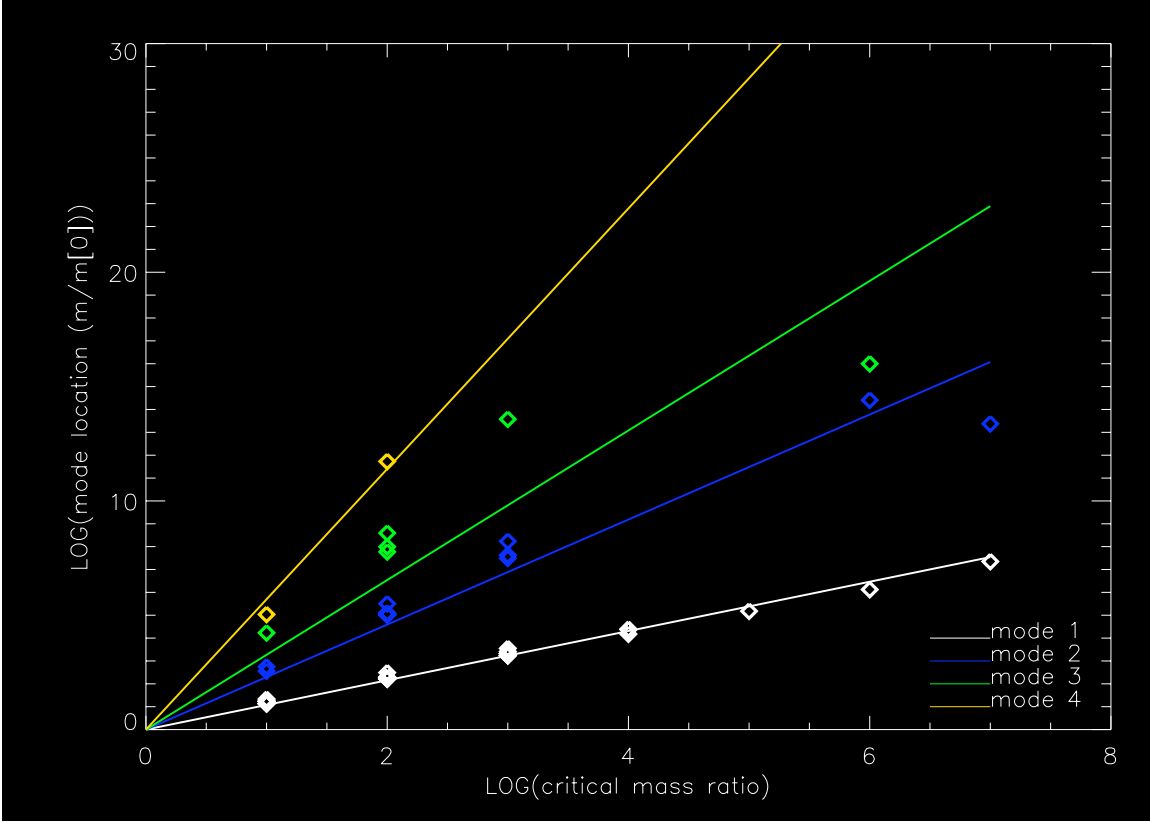
Figure 27. The value of m/m_0 of a mode versus the μ_{crit} for various simulations. Solid lines are fitted power-law indices that relate μ_{crit} to the location of that particular mode (color coded). Fits are reported in eq 23.

The fits reveal that the value of m/m_0 at which modes form is dependent on the threshold value of mass ratio for accretion, μ_{crit}. Combining this relation with the prescribed size range of a distribution, one may predict the largest-size mode possible in the distribution and know that the distribution falls off sharply thereafter. The maximum possible mass ratio of colliding bodies in a system is $\mu_{max} = m_{max}/m_o$. The multiplicative number of times larger the maximum size ratio is than the critical value is given by the expression $\mu_{ratio} = \mu_{max}/\mu_{crit}$. For the mass size of mode number i, $m_i = m_o A_i \mu_{crit}^{\varepsilon(i)}$, where A_i is a constant and ε_i is the power law index that relates μ_{crit} to m_i as found in Eq 23. So, if $\mu_{ratio} < \varepsilon_1$ no prediction is possible. If $\varepsilon_i < \mu_{ratio} < \varepsilon_{i+1}$, the distribution drop off is predicted at

a size just larger than $m_i = m_o A_i \mu_{crit}{}^{\varepsilon(i)}$. Thus, $m_{dropoff}$ is a function of m_o, m_{max}, and μ_{crit}, and the number of modes possible equals i.

Because the modes trend with the value of μ_{crit}, I propose that a sharp accretion threshold is responsible for the buildup of multiple modes in a size distribution through binary collisions. The tidally-modified accretion that governs the outcome of colliding masses in a system has a sharp threshold: 100% of all incoming mass accretes to form one new body if $m_1/m_2 > \mu_{crit}$, and 100% of all incoming mass fragments into a distribution of smaller bodies if $m_1/m_2 < \mu_{crit}$. In a numerical implementation of the coagulation equation (Equation 111, Equation 21), tidally-modified accretion allows the smallest sized body in the system, m_0, to accrete only when it encounters a body larger than $\mu_{crit}m_0$, but that body can encounter many bodies of comparable size and fragment. As in all collisional system distributions, there are a lot more small bodies than large ones; therefore, the smallest bodies built via accretion are of size $\mu_{crit}m_0$, which build up quickly because of the large number of bodies sized m_0. Meanwhile, bodies of all sizes produce a steady distribution of fragments due to collisions with bodies of comparable sizes. This progresses to build a mode at roughly $m = \mu_{crit}m_0$. Thus, one may predict a "throw distance" for accreted mass in a system to be a factor of μ_{crit}, which is the trend seen via simple visual inspection and demonstrated via the more detailed fit to the simulations. This process continues to occur once mode 1 reaches a sufficient size and then occurs again at a size roughly a factor μ_{crit} from the mass of mode 1. Building of modes continues to "echo" though the system until it reaches an upper size cutoff and then the number of bodies just larger than the largest mode possible quickly falls off. From this explanation, the reason modes develop is because of the "all or nothing" way that accretion operates. The sharp threshold of the

critical mass ratio builds modes at specific locations and keeps the continuous distribution of fragments from overtaking them at those specific sizes.

To test the idea that a sharp accretion threshold is responsible for the multimodal distribution I investigate how to remove modes from the system by softening the accretion threshold. The accretion threshold we have used up to this point has been a step function of 100% fragmentation below and 100% accretion above μ_{crit} (Figure 28); therefore, I experiment with several functional forms of the accretion threshold that have a smoother transition from fragmentation to accretion (Figure 29-36). Eight different accretion threshold functions, which relate the percentage of total colliding mass that accretes to a new body to the mass ratio of the colliding bodies, were examined. For each, the initial conditions and physics are identical with the exception of the accretion threshold function. The functions examined are listed below, each is accompanied by a figure of the fraction of colliding mass accreted or fragmented as a function of mass ratio of colliding bodies and a figure of the resulting evolution of the distribution (each color is a different time):

a) "Binary"
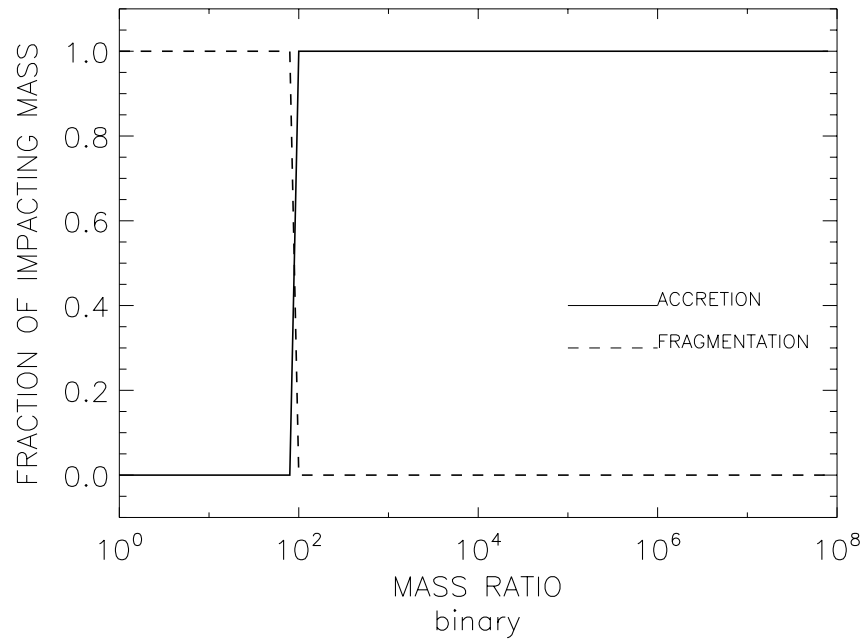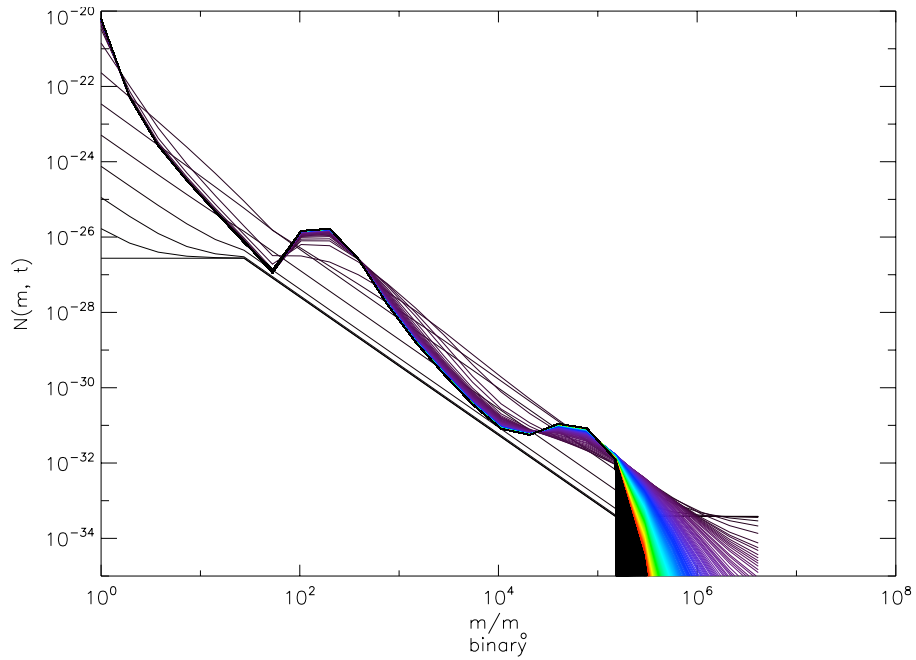
b)

Figure 28. Distribution Evolution via a Binary Accretion Function. a) Plot of the "accretion threshold function." The fraction of impacting mass that accretes or fragments as a function of the mass ratio of colliding bodies. b) The resulting evolution of the distribution. Colored lines distinguish various time steps. The earliest times are purple and run in time through green to red and final is in black.

BINARY:

Accretion:

$P(\mu \geq \mu_{crit}) = 1$

$P(\mu < \mu_{crit}) = 0$

Fragmentation:

$P(\mu \geq \mu_{crit}) = 1$

$P(\mu < \mu_{crit}) = 0$

a) "Neg Combo"
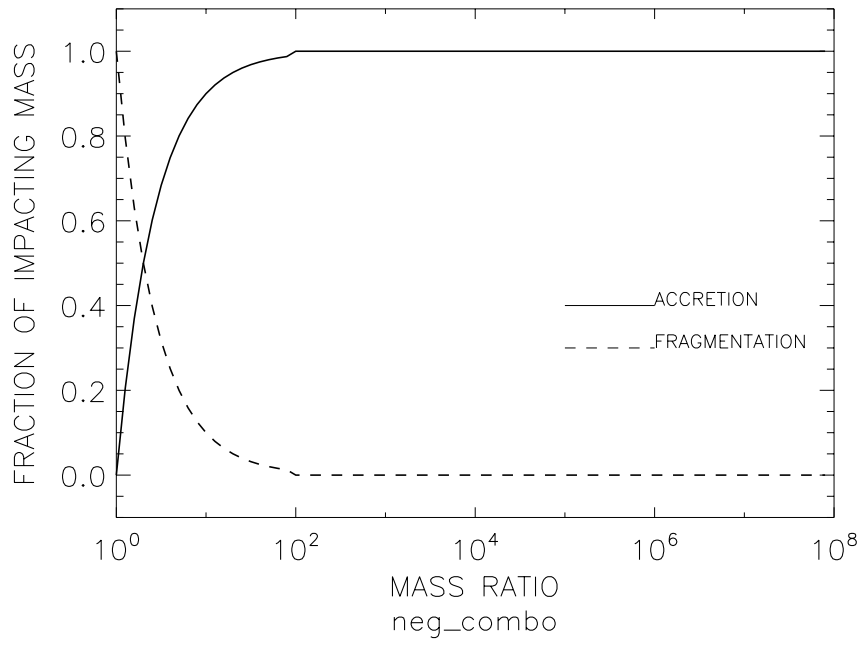
b)
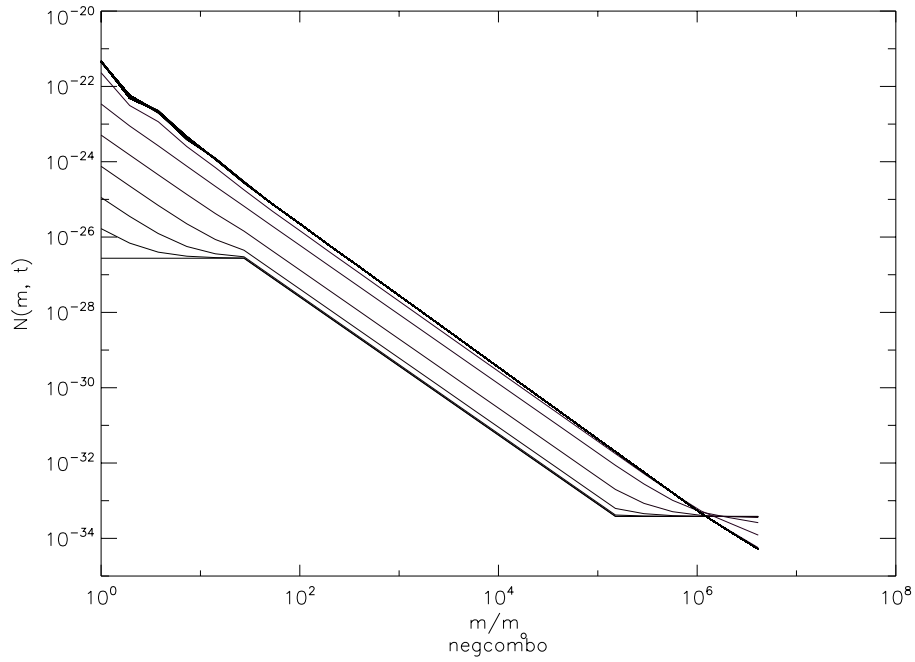
Figure 29. Distribution Evolution via a "Neg Combo" Accretion Function. a) Plot of the "accretion threshold function." The fraction of impacting mass that accretes or fragments as a function of the mass ratio of colliding bodies. b) The resulting evolution of the distribution. Colored lines distinguish various time steps. The initial distribution is the

power law that begins and ends in flat sections. It then evolves to the near-power law upper curve.

NEG_COMBO:

Accretion:

$P(\mu \geq \mu_{crit}) = 1$

$P(\mu < \mu_{crit}) = 1 - 1/\mu$

Fragmentation:

$P(\mu \geq \mu_{crit}) = 0$

$P(\mu < \mu_{crit}) = 1/\mu$

a)

FRACTION OF IMPACTING MASS

MASS RATIO
comboP1

ACCRETION
FRAGMENTATION
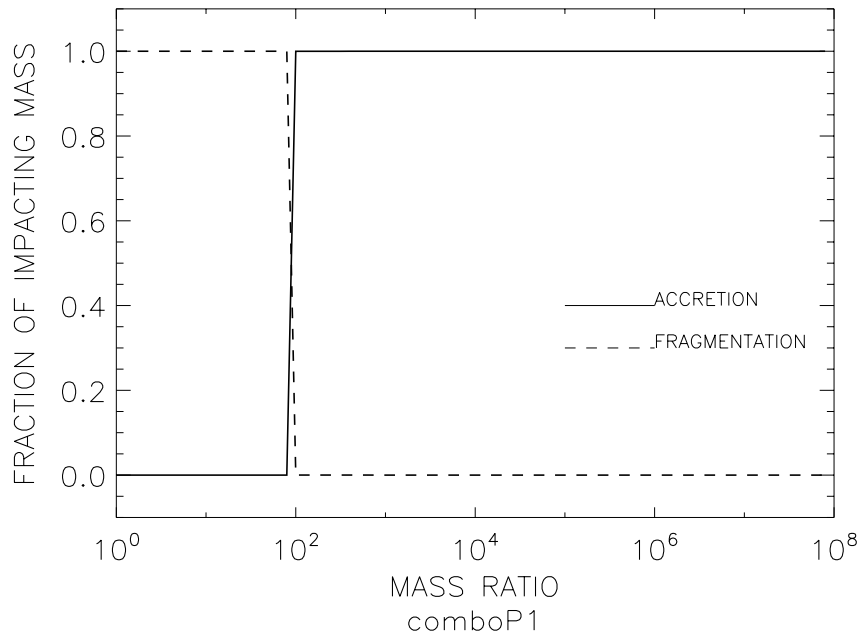
b)
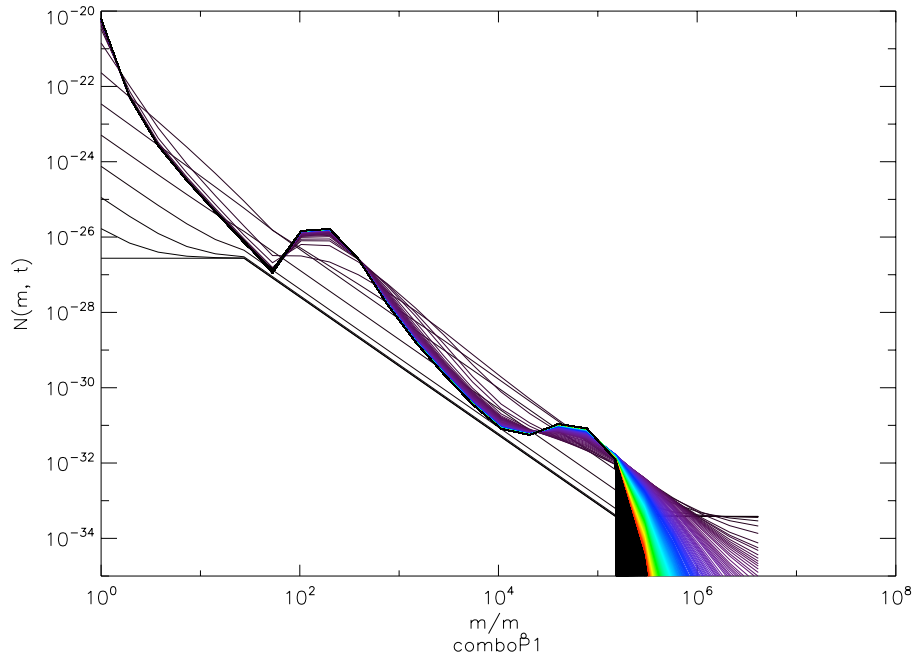
Figure 30. Distribution Evolution via a "Combo" Accretion Function. a) Plot of the "accretion threshold function." The fraction of impacting mass that accretes or fragments as a function of the mass ratio of colliding bodies. b) The resulting evolution of the distribution. Colored lines distinguish various time steps. The earliest times are purple and run in time through green to red and the final is the black multimodal distribution.

COMBO:

for fraction F =1.0 (various values tested but not plotted here: 0.01,0.1,0.5,1.0)

Accretion:

$P(\mu \geq \mu_{crit}) = 1 - F/\mu$

$P(\mu < \mu_{crit}) = 0$

Fragmentation:

$P(\mu \geq \mu_{crit}) = F/\mu$

$P(\mu < \mu_{crit}) = 1$

a)
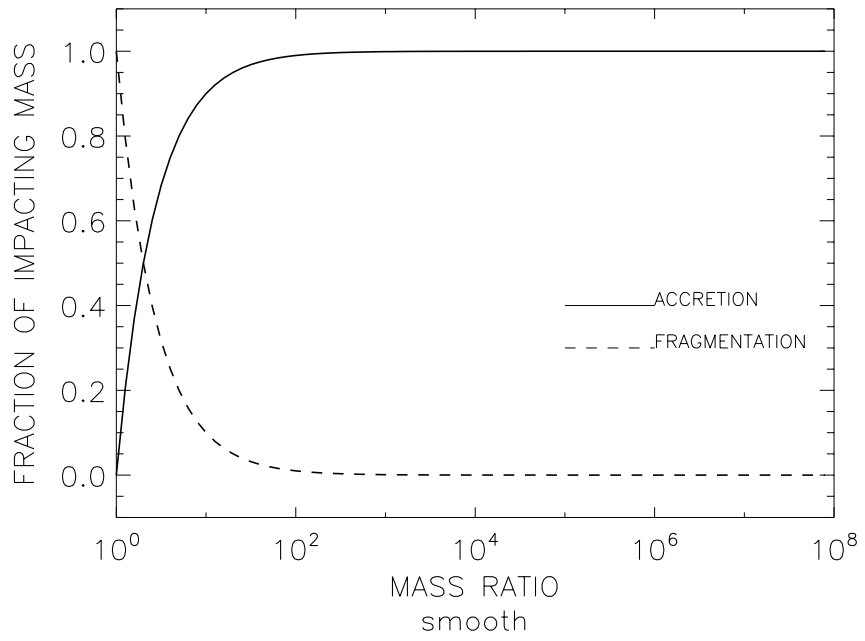
b)
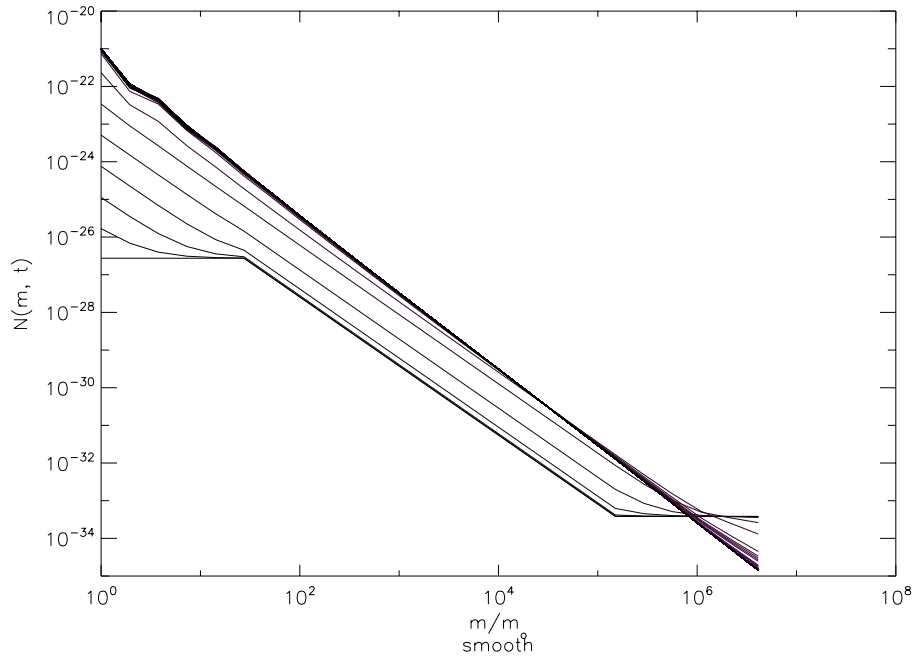
Figure 31. Distribution Evolution via a "Smooth" Accretion Function. a) Plot of the "accretion threshold function." The fraction of impacting mass that accretes or fragments as a function of the mass ratio of colliding bodies. b) The resulting evolution of the distribution. Colored lines distinguish various time steps. The initial distribution is the

power law that begins and ends in flat sections. It then evolves to the near-power law upper curve.

SMOOTH:

Accretion:

$P(\mu) = 1 - 1/\mu$

Fragmentation:

$P(\mu) = 1/\mu$

a)
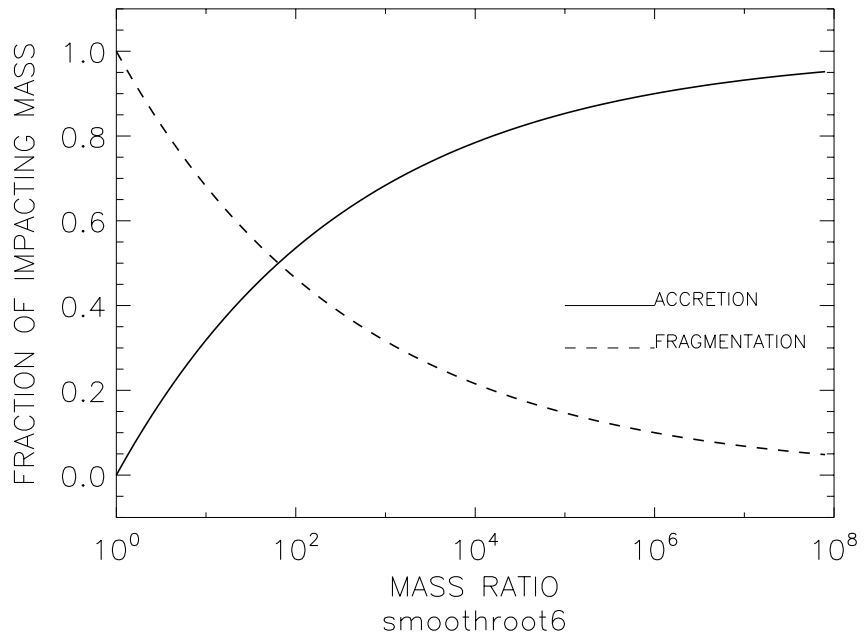
smoothroot6

b)
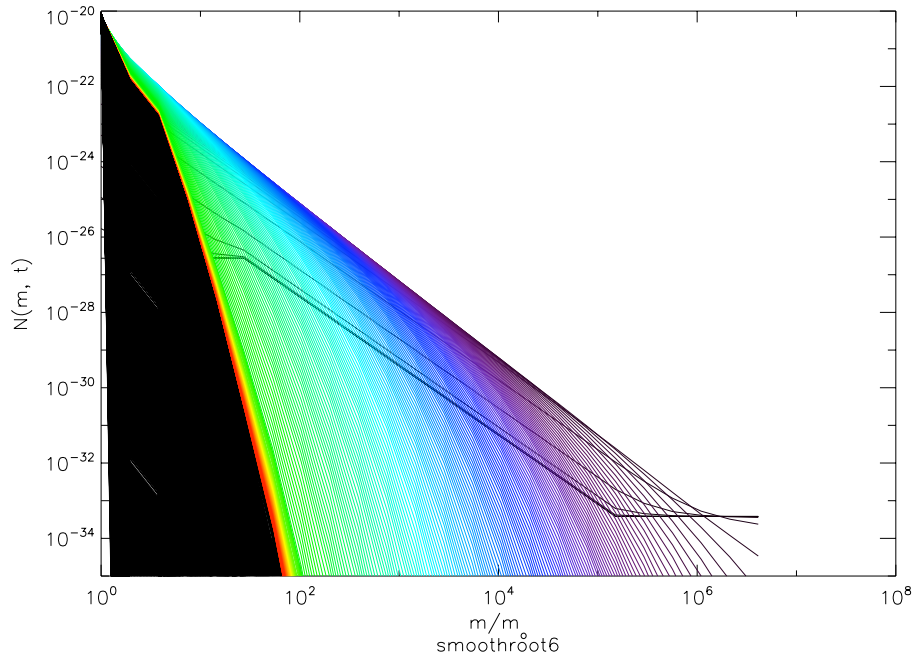
Figure 32 . Distribution Evolution via a "Smooth Root" Accretion Function. a) Plot of the "accretion threshold function." The fraction of impacting mass that accretes or fragments as a function of the mass ratio of colliding bodies. b) The resulting evolution of the distribution. Colored lines distinguish various time steps. The earliest times are purple

and run in time through green to red and the final is the black distribution that is completely eroded to the smallest size bodies.

SMOOTHROOT:

for Nth root (tested values N=3 (not plotted here) and N=6 (plotted here))

Accretion:

P(μ) = 1 - (1/μ)^(1/N)

Fragmentation:

P(μ) = (1/μ)^(1/N)

a)
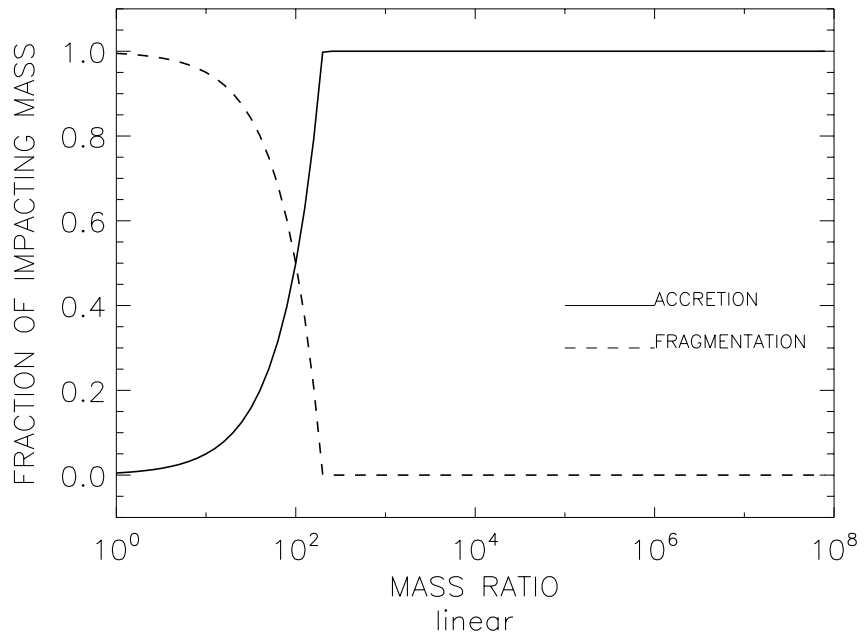
b)
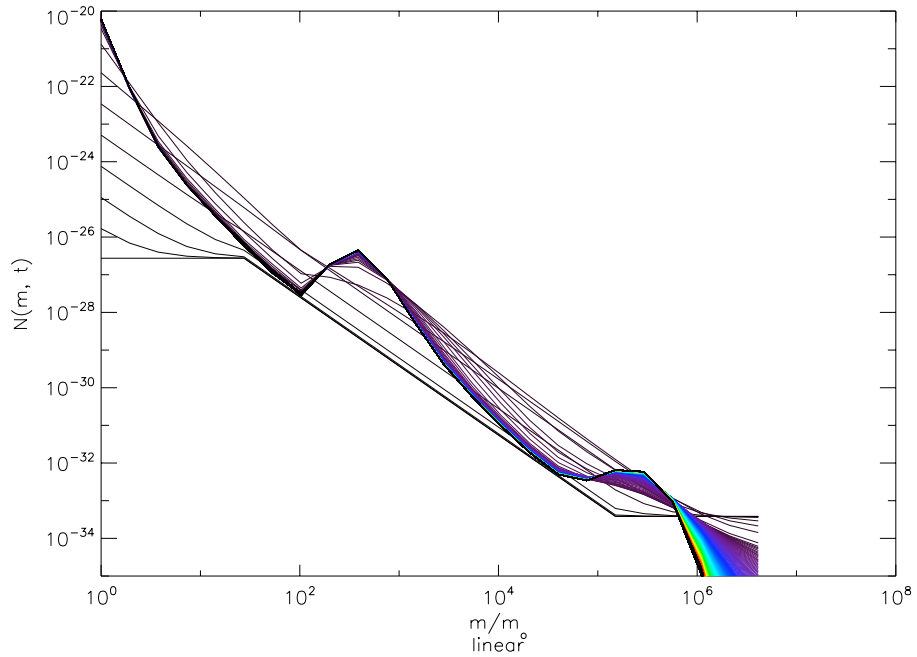
Figure 33. Distribution Evolution via a "Linear" Accretion Function. a) Plot of the "accretion threshold function." The fraction of impacting mass that accretes or fragments as a function of the mass ratio of colliding bodies. b) The resulting evolution of the distribution. Colored lines distinguish various time steps. The earliest times are purple and run in time through green to red and the final is the black multimodal distribution.

104

LINEAR:

Accretion:

$P(\mu) = (0.5/\mu_{crit}) * \mu$

Pmax=1

Fragmentation:

$P(\mu) = 1 - (0.5/\mu_{crit}) * \mu$

Pmin=0

a)
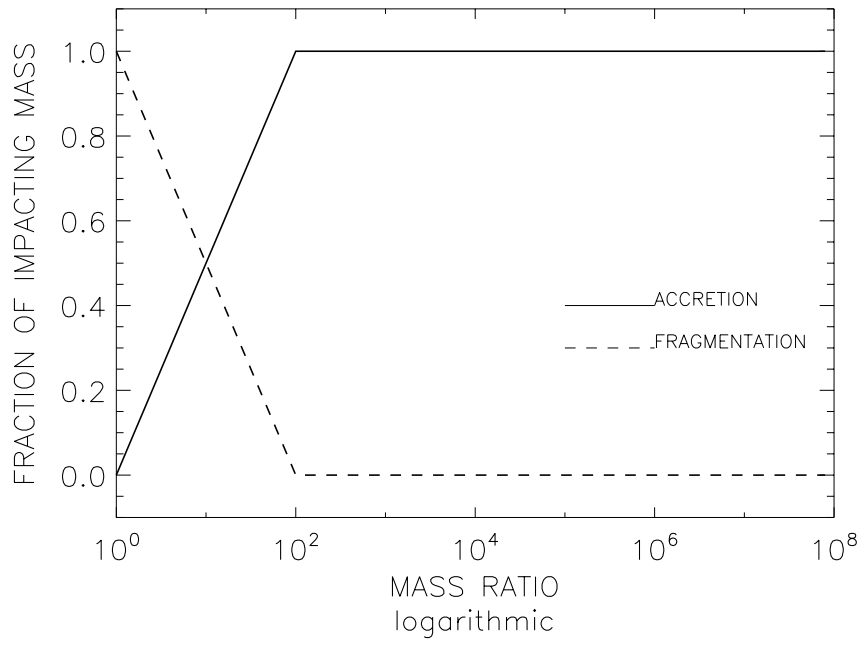
b)
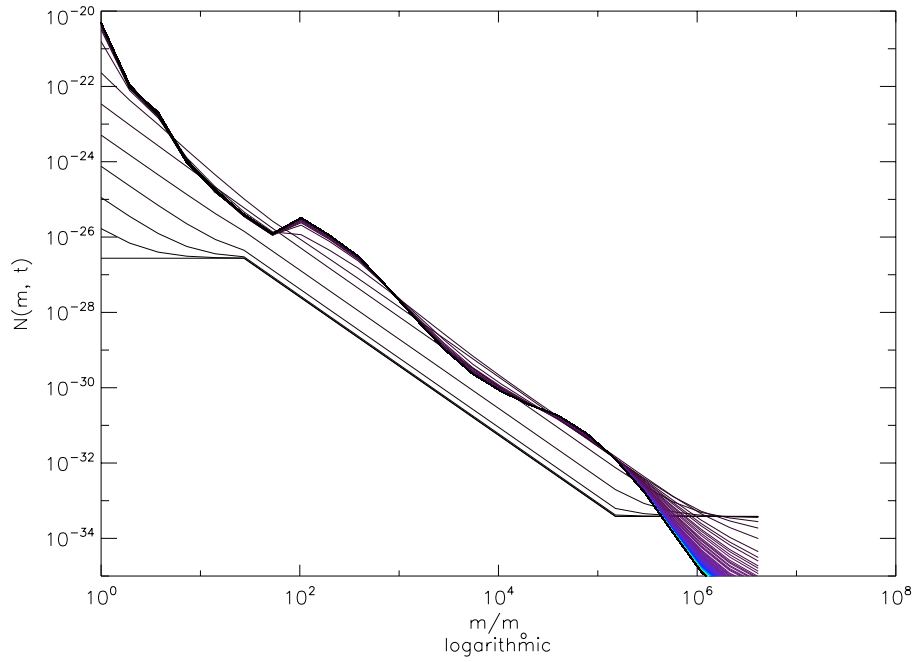
Figure 34. Distribution Evolution via a "Logarithmic" Accretion Function. a) Plot of the "accretion threshold function." The fraction of impacting mass that accretes or fragments as a function of the mass ratio of colliding bodies. b) The resulting evolution of the distribution. Colored lines distinguish various time steps. The earliest times are purple and run in time through green to red and the final is the black multimodal distribution.

LOGARITHMIC:

Accretion:

$P(\mu) = \ln(\mu)/\ln(\mu_{crit})$ *Pmax=1*

Fragmentation:

$P(\mu) = 1 - \ln(\mu)/\ln(\mu_{crit})$

Pmin=0

a)
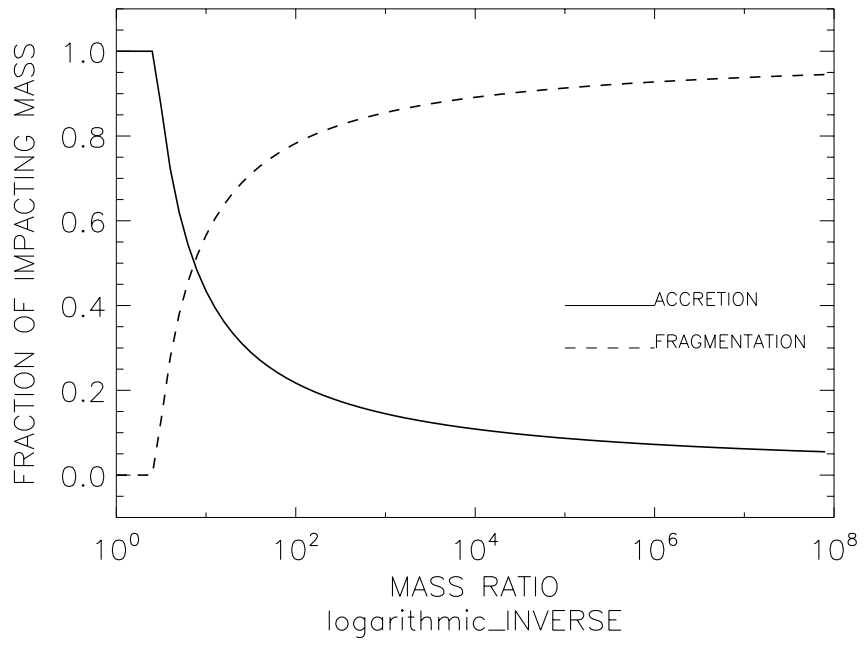
b)
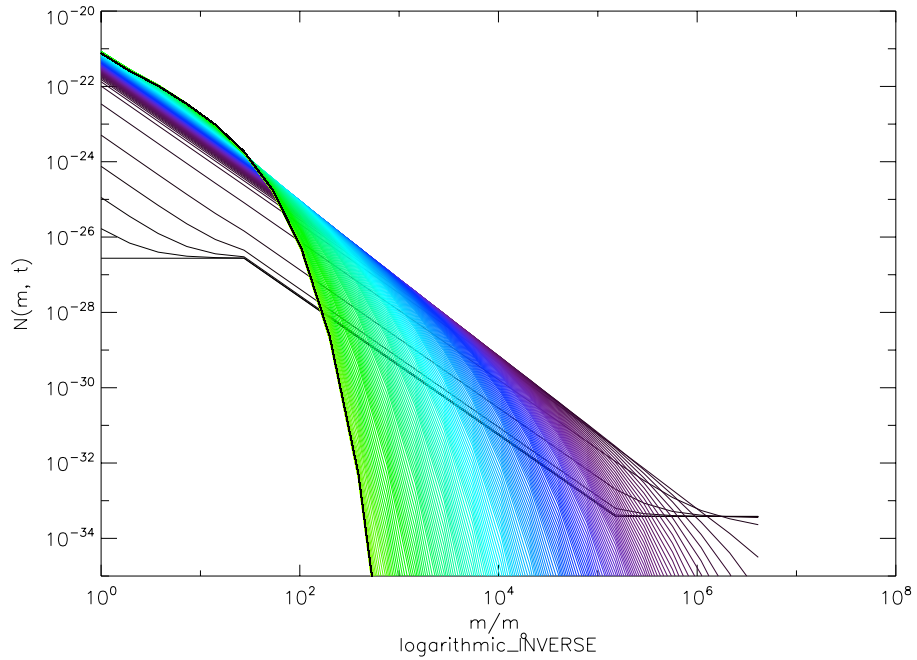
Figure 35. Distribution Evolution via a "Logarithmic Inverse" Accretion Function. a) Plot of the "accretion threshold function." The fraction of impacting mass that accretes or fragments as a function of the mass ratio of colliding bodies. b) The resulting evolution of the distribution. Colored lines distinguish various time steps. The earliest times are purple and run in time through green and the final is the black distribution.

LOGARITHMIC_INVERSE:

Accretion:

$P(\mu) = \ln(\mu_{crit})/\ln(\mu)$

Pmax=1

Fragmentation:

$P(\mu) = 1 - \ln(\mu_{crit})/\ln(\mu)$

Pmin=0

a)
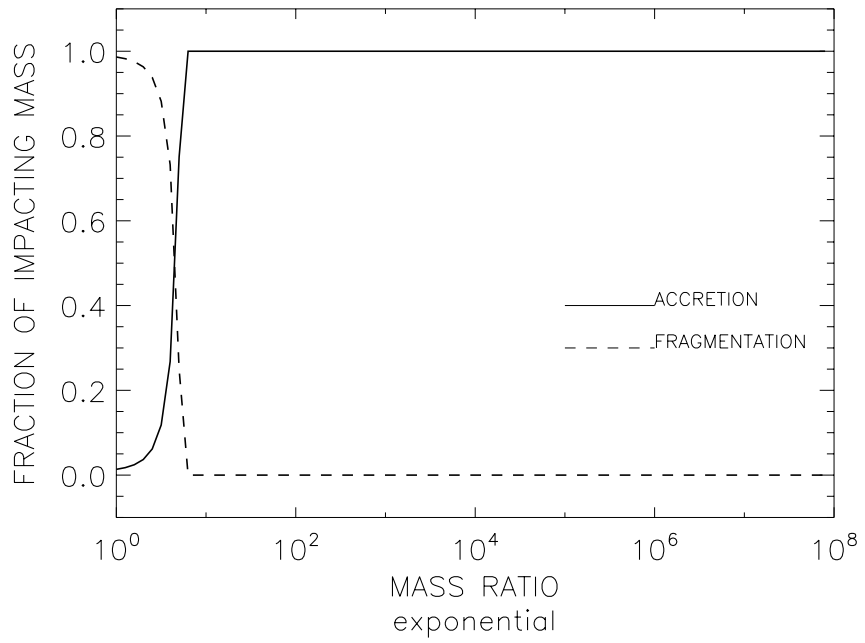
b)
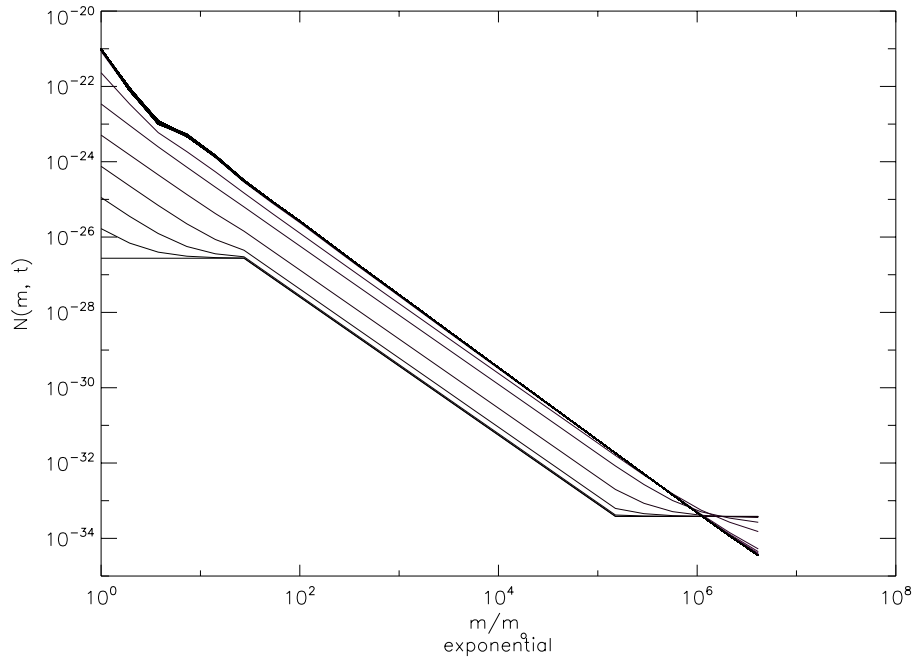
Figure 36. Distribution Evolution via a "Exponential" Accretion Function. a) Plot of the "accretion threshold function." The fraction of impacting mass that accretes or fragments as a function of the mass ratio of colliding bodies. b) The resulting evolution of the distribution. Colored lines distinguish various time steps. The initial distribution is the

power law that begins and ends in flat sections. It then evolves to the near-power law upper curve.

EXPONENTIAL:

Accretion:

$P(\mu) = \exp(\mu)/(2\mu_{crit})$

Pmax=1

Fragmentation:

$P(\mu) = 1 - \exp(\mu)/(2\mu_{crit})$

Pmin=0

The accretion threshold functional forms for which a multimodal distribution

evolves are: Binary, Combo, Linear, and Logarithmic. These functional forms all have some

form of a hard transition from accretion to fragmentation and include a range of μ for

which accretion or fragmentation is at 100%. The multimodal distribution does not evolve

when Neg_combo, Smooth, Smooth_root, or Exponential describe the accretion

percentages. None of these have a sharp transition from accretion to fragmentation.

Neg_combo, Smooth, Smooth_root, and Log_inverse all have a $(1/\mu)^N$ dependence. The

Log_inverse suppresses accretion for almost all body sizes, so large bodies are all eroded

away, which is why I exclude it from the remainder of the analysis here. From this analysis,

it is evident that the sharp threshold between accretion and fragmentation of colliding

bodies causes a distribution to evolve to a multimodal state. Smoothing the transition from

complete accretion to complete fragmentation so there can be a percentage of each

outcome at certain values of μ suppresses the modes.

I now investigate the physical plausibility of a natural mechanism that would allow for such a smooth transition. As mentioned at the beginning of this section, other modelers and observers have reported the appearance of multimodal size distributions of collisional systems. Campo Bagatin et al (1994) postulate the cause to be the small-size cutoff of the asteroid distribution. Weidenschilling suggests a "bump" in the observed asteroid population as a result of accretional regime change, which has a sharp transition between the physical processes that govern growth for bodies of different sizes. Meanwhile, I find and explain mode formation as a result of the sharp threshold between accretion and fragmentation of colliding masses. These causes of mode formation are all more generally consistent with sharp transitions or thresholds in a physical property of a system. This explanation also boosts the plausibility of multimodal distributions occurring in natural systems. Sharp changes in physical parameters are realistic, such as loss mechanisms for small particles or thresholds for sticking. I move forward with my model by keeping in mind the characterization of mode location and spacing just provided, the causes thereof, and what they mean for the actual F ring.

Another aspect of the shape of the quasi steady-state distribution is the prescribed value of the power law index, q_{ej}, of fragments redistributed after collision. The overall trend of the model results, regardless of modes is along a differential power law index $q=1.83$. This is the same value chosen for the initial distribution, $q_i=1.83$, but the model evolved to this regardless of initial condition (Figure 37).   The value of q_{ej} does have an effect on the evolution of the distribution. Because accreting material forms new bodies at least μ_{crit} larger in mass than the smaller of the colliding pair, the modes form at regularly-spaced sizes. The small-size cutoff of the distribution establishes the location of

subsequent modes from the value of m_0, as the smallest bodies with which they can accrete

are necessarily $\mu_{crit}m_0$ in size. Thus, at certain locations, modes continuously build up.

Meanwhile, the source of bodies in the troughs of the "wavy pattern" is predominantly

fragments from collisions among larger bodies. Since the fragments are redistributed

according to q_{ej}, the distribution in the troughs has this characteristic power law slope.

Figure 37 shows an extreme case for ease of visual inspection where $q_{ej}>>q_i$. When $q_{ej}\sim q_i$,

however, the distribution shape exhibits much "softer" modes and troughs. For $q_{ej}\leq0.5$ (for

$q_i=1.83$) or $q_{ej}<<q_i$ (generally), the fragments redistribute along a "flat" distribution such

that the overall appearance of the modes shifts. Figure 38 shows a fit to the first and

second mode locations for simulations using various q_{ej} values ($q_i=1.83$ for all). The body

masses at which first and second modes occur move to larger m values as q_{ej} decreases.

The fitted relationship is found to be:

Mode 1: $217\ q_{ej}^{-0.66}$

Mode 2: $9\times10^4\ q_{ej}^{-0.72}$

Equation 24

Such small power law index values are not physically realistic in a system like the F ring, so

this has no effect on my model, but other modelers should note this effect if they have

particularly shallow redistribution functions.
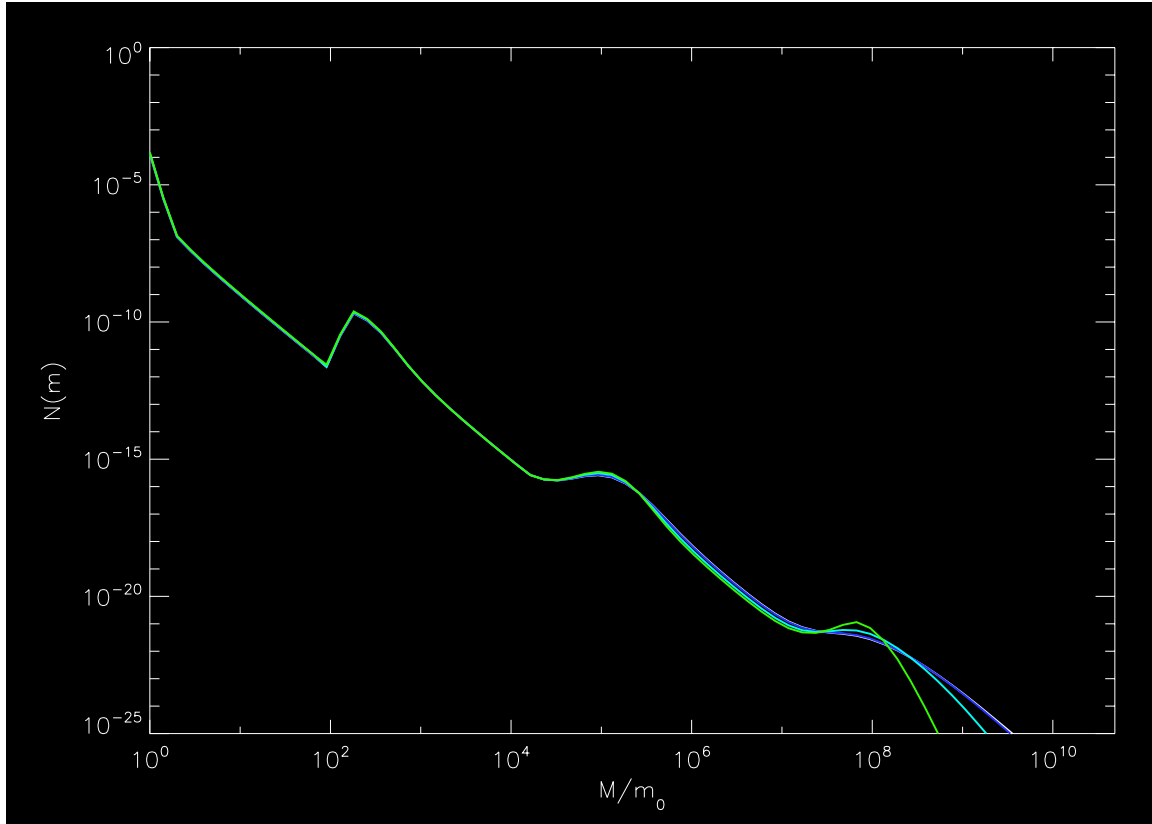
Figure 37. Differential size distribution outcomes for different initial distributions. Each has a different power law index: q_i=2.33 (green), q_i=1.83 (cyan), q_i=1.33 (blue), q_i=0.83 (white). The model evolves to the same quasi-steady state distribution regardless of initial distribution.
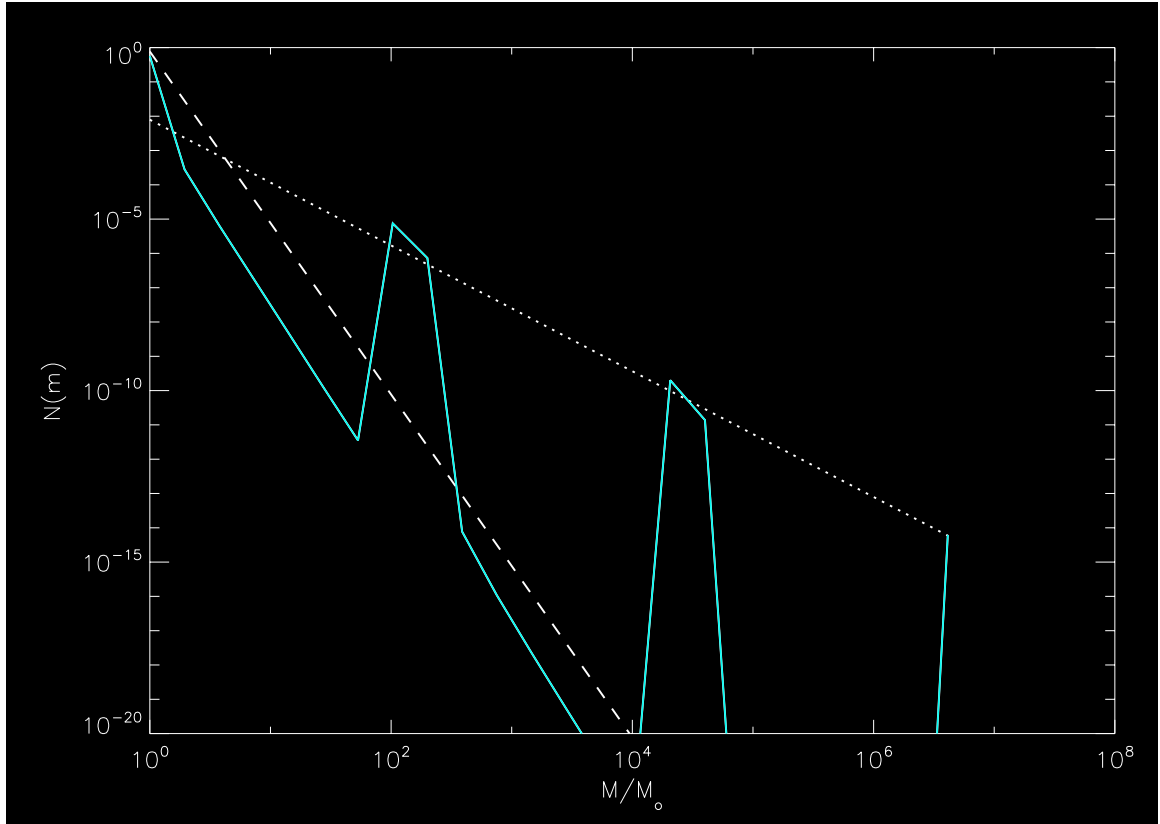
Figure 38. An extreme case for ease of visual inspection where $q_{ej}>>q_i$. The fragments redistribute along a very steep distribution such that the modes are sharp increases along the general trend of the distribution. The solid light blue curve is the final distribution; dotted white is the initial power law; and dashed white is the redistribution power law.
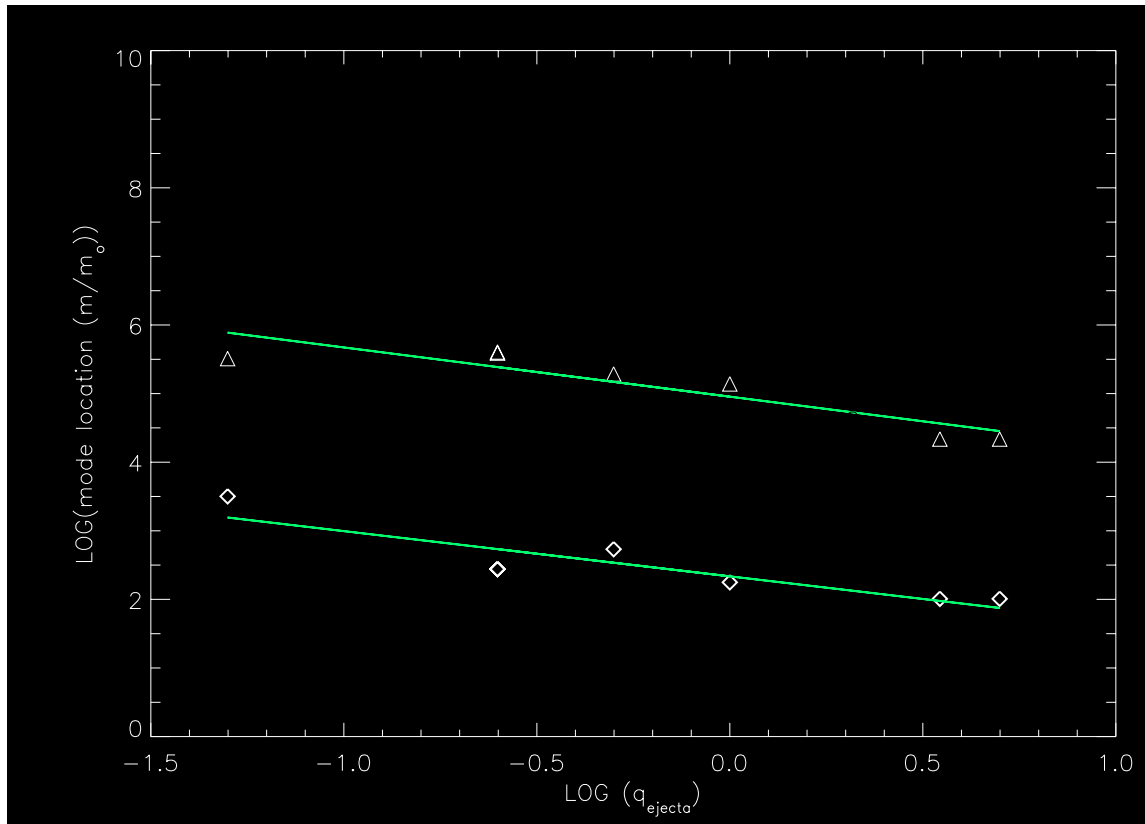
Figure 39. Fit to the first and second mode locations for simulations using various q_{ej} values (q_i=1.83 for all). The body mass at which first and second modes occur moves to larger m values as q_{ej} decreases. Fit reported in Equation 24.

In summary of this section, the binary collision model adapted from the coagulation equation evolves to a multimodal distribution of bodies. Separation of the modes of the distribution scales with the critical mass ratio necessary for accretion in the system. Regardless of initial condition, the distribution forms around a differential power law index of 1.83, but the redistribution of fragmented material may affect the sharpness of modes. Fraser (2009) derives an analytic expression for the size at which a "divot" occurs in his modeled distribution of the Kuiper belt. This expression is dependent on the energy threshold for disruption and the strength parameters of colliding material. Comparison of his result (Figure 40) shows that the "divot" is simply the trough that occurs before modes I report in this section. He overlooks any "echos" in the system that produce a multimodal

shape. Thus, even though this behavior has been reported in other models and

observations, I am the first to undertake a full investigation of the behavior and develop an

explanation for it.
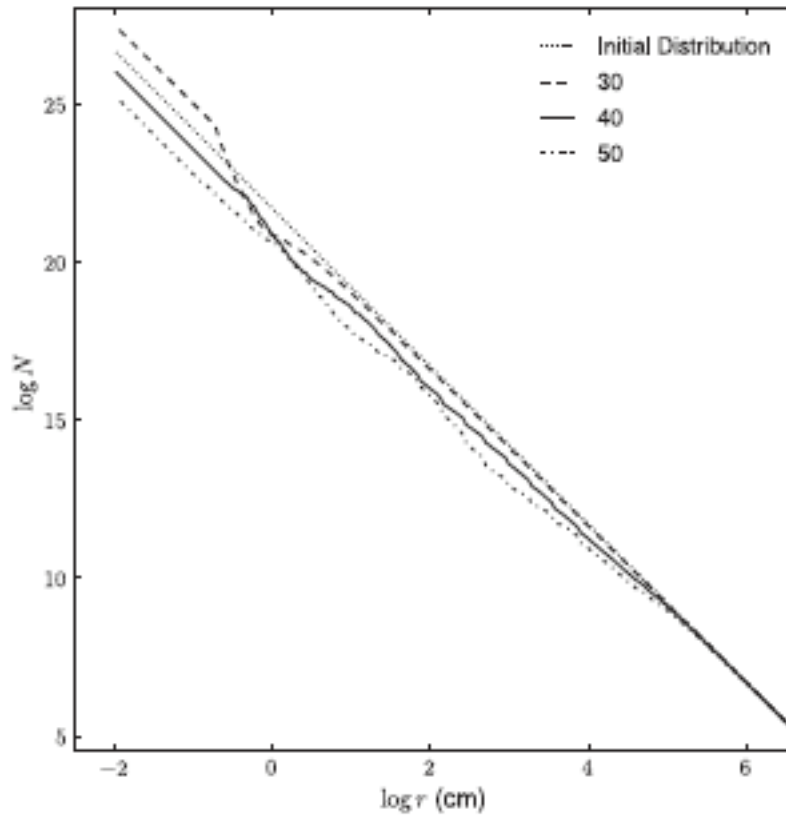
Figure 40. From Fraser (2009), Figure 10. "Results of collisional evolution after 2000 time steps, starting from a distribution in collisional equilibrium (dotted line). The various lines are the results when equilibrium was forced over 30, 40, and 50 bins." When allowed to evolve, the model develops multiple modes, but Fraser only comments on the locations of the divot at a size just smaller than the first mode.

3.1.4 **Attempts to match the modeled distribution to the observed distribution of F ring clumps**

As discussed in the "Observations" section, the observed distribution of clumps in

the F ring has a differential power law index of *2<q<2.5*. Figure 41 compares the

incremental distributions of the observed features, BE02 results, and my multimodal

120

model. Obviously, the modeled distributions are significantly steeper than that observed.

In this section, I present several attempted methods for flattening the modeled distribution

to match the observations.
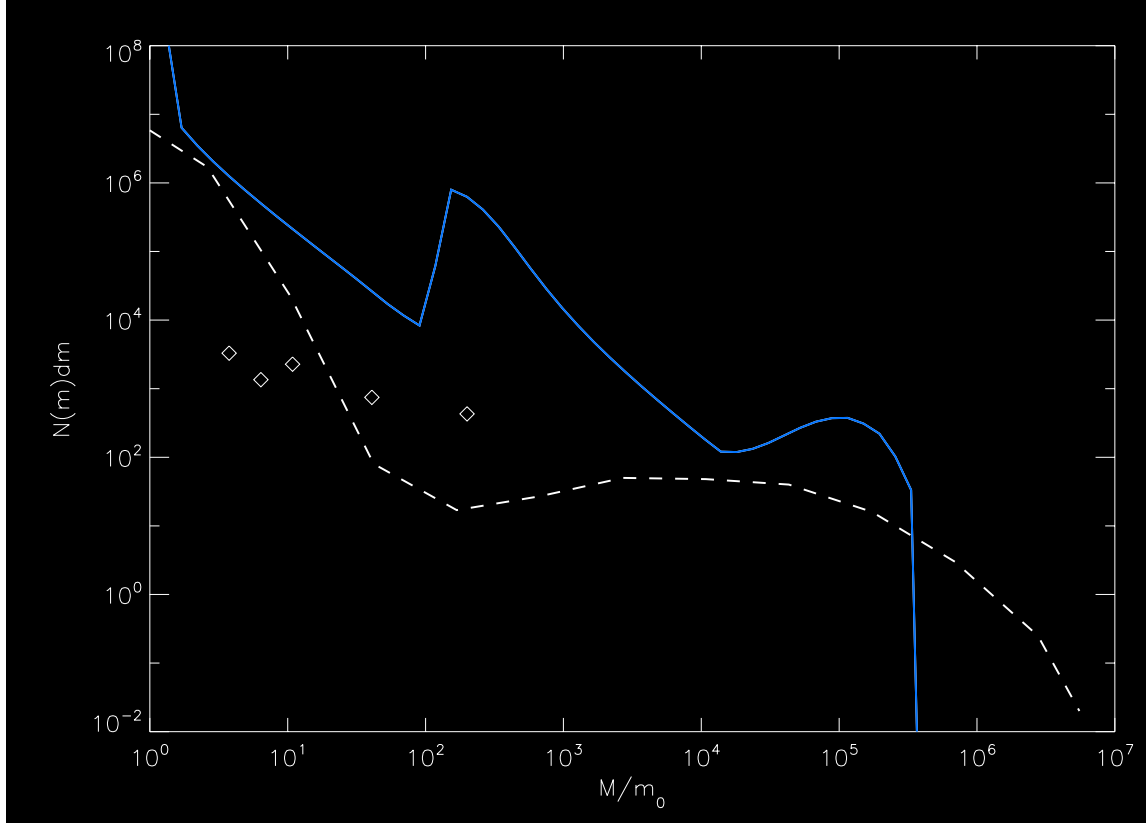
Figure 41. Comparison of the incremental distributions of the observed distribution
(reported Moonlets and Icicles; diamonds), BE02 result (dashed white line), and my binary
accretion model (blue solid line). Both modeled distributions are too steep to match the
observed distribution of aggregates.

In order to decrease the power law index of the modeled distribution, the

production of larger bodies must be faster than that of the smaller bodies. Increasing the

collision frequency of larger bodies could provide such an increase in the number of larger

bodies. Rather than the standard, fixed relative velocity of v_{rel}= 50 cm/s, I experiment with

larger collision velocities. For example, I select a collisional velocity equal to the escape

velocity of the target body in a collision $v_{esc} = \sqrt{2GM_{Saturn} / r_{t\arg et}} \propto m^{-1/6}$. This weak mass-

dependent velocity results in smaller collisional velocities for larger objects. Figure 42 shows that the resulting distribution remains a multimodal distribution with a general trend of q=1.83. Next, I use a collisional velocity equal to the escape velocity of the dominant bodies in the system, those in the first mode, $v_{esc} = \sqrt{2GM_{Saturn}/r_{model}}$. Again, this velocity has no mass dependence and thus does not lessen the slope of the quasi-steady-state distribution (Figure 43).
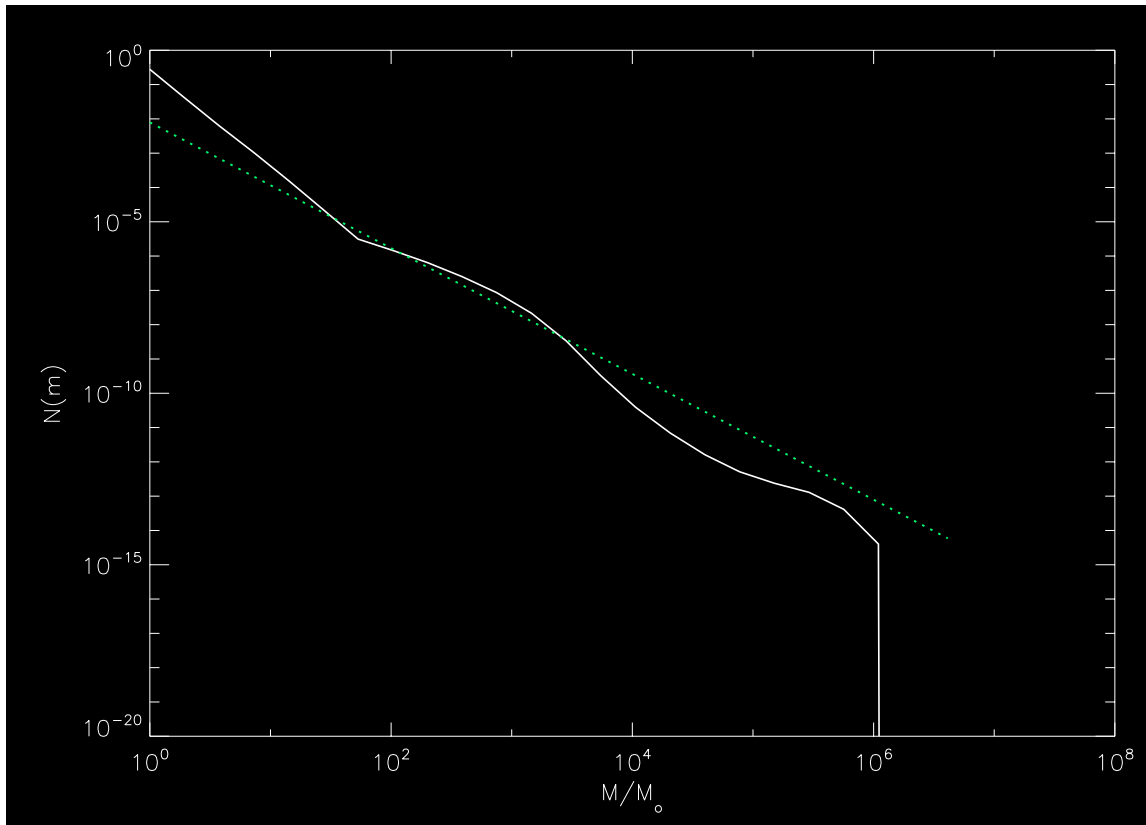
Figure 42. The collisional velocity equal to the escape velocity of the target body in a collision $v_{esc} = \sqrt{2GM_{Saturn}/r_{target}} \propto m^{-1/6}$. This weak mass-dependent velocity results in smaller collisional velocities for larger objects. The quasi-steady-state distribution (dotted line) compared to the observed distribution (diamonds) is still steeper. The continuous power law (solid line) is the initial distribution of the system.
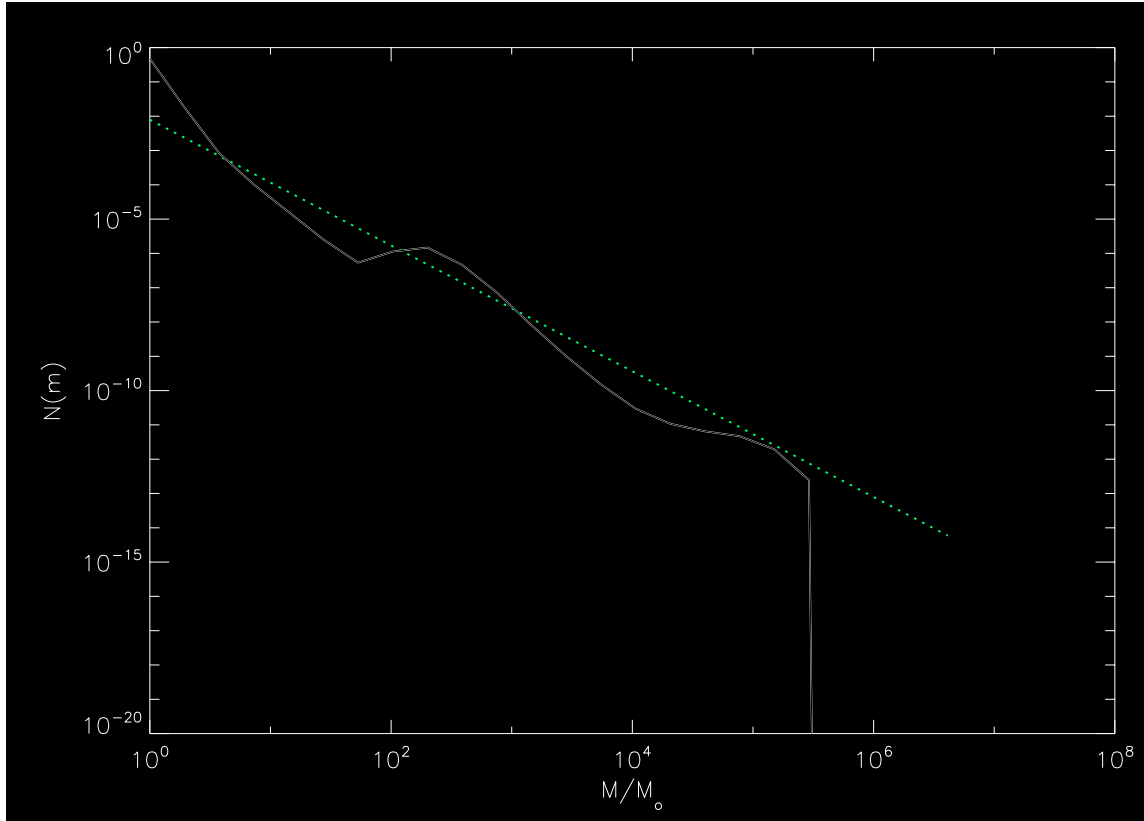
Figure 43. The collisional velocity equal to the escape velocity of bodies in the first mode, $v_{esc} = \sqrt{2GM_{Saturn}/r_{model}}$. Again, this velocity has no mass dependence and thus does not lessen the slope of the quasi-steady-state distribution (solid white line). The continuous power law (dotted green line) is the initial distribution of the system.

The next method I use fixes the collisional velocity at 50 cm/s, but artificially increases the erosion of larger bodies in the system. For $r_{critical}>1$ km, accretion is only $P_{acc}\%$ of the original, and fragmentation is $(100-P_{acc})\%$. The intent here is that erosion of larger bodies builds up the amount of small material uniformly by mass, and would result in a flatter distribution for the smaller sizes of the distribution. This model, however, evolves to the multimodal distribution with a sharp cutoff at the prescribed $r_{critical}$ (Figure 44).
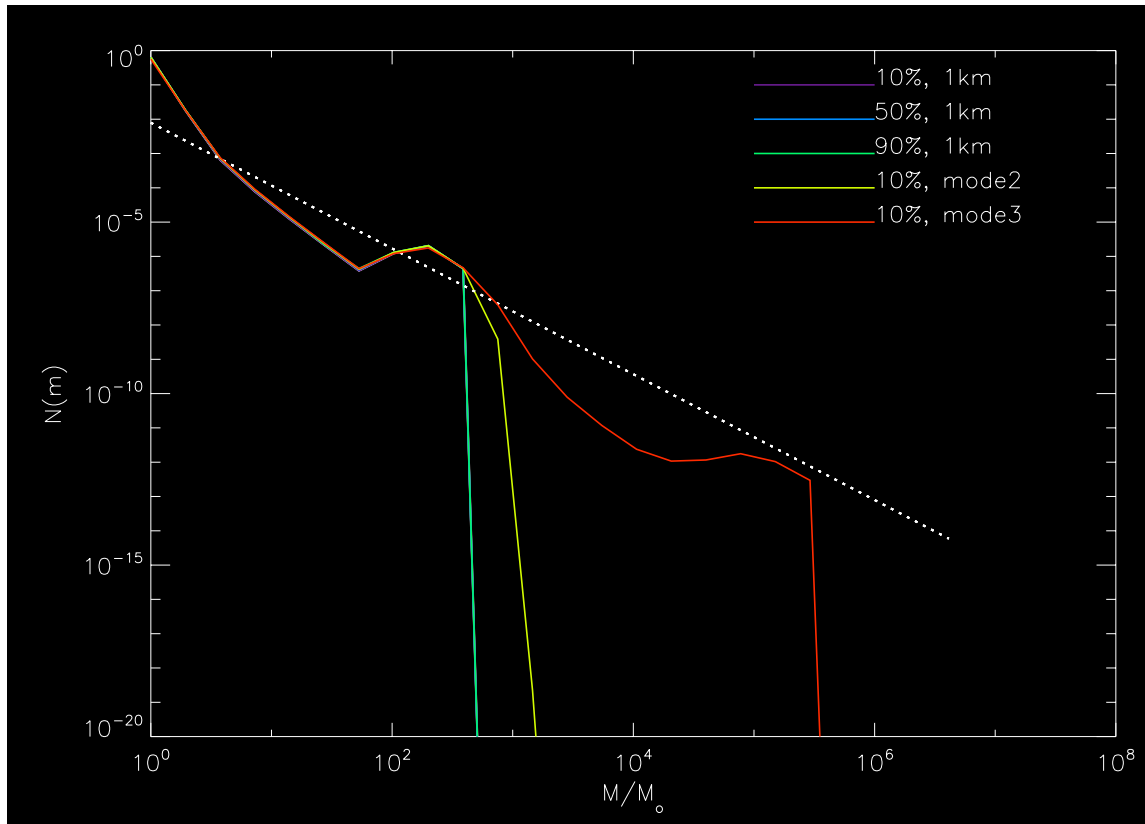
Figure 44. The collisional velocity fixed at 50 cm/s, but model artificially increases the erosion of larger bodies in the system. For $r_{critical}$, accretion is only P_{acc}% of the original, and fragmentation is $(100-P_{acc})$%. Cyan curve is the overlap of purple, blue, and green curves that all have $r_{critical}$=1 km.

Ruling out collision velocity and fragmentation as mechanisms that affect the final distribution of F ring bodies, I experiment with various power law indices for the initial distribution and the redistribution of fragments. The initial distribution of has no effect on the evolution or final state of the distribution. Comparing distributions of various power law indices, broken power laws, and the observed distribution, Fig 37 shows that the system necessarily evolves to the same quasi-steady state. Evolution should progress regardless of the initial distribution of material; thus, I have confirmed the expected outcome. To test the effects of varying the redistribution of fragments, q_{ej}, I set the initial distribution to be $n(m,t)dm \propto m^{-q_m}dm$, where q_m=1.83, Dohnanyi's prediction for a

collisionally evolved system. Figure 45 compares final distributions for q_{ej} values from 0.05 to 1.23. As discussed in the assessment of the "wavy pattern" (Section 3.1.3), the value of q_{ej} does have an effect on the evolution of the distribution. The source of bodies in the troughs of the "wavy pattern" is predominantly fragments from collisions among larger bodies. Since the fragments are redistributed according to q_{ej}, the distribution in the troughs has this characteristic power law slope. Figure 38 shows an extreme case for ease of visual inspection where $q_{ej} >> q_i$. When $q_{ej} \sim q_i$, however, the distribution shape exhibits much "softer" modes and troughs. For $q_{ej} \leq 0.5$ (for $q_i = 1.83$), the overall appearance of the modes shifts, but the overall distribution does not itself become "flatter." The body mass at which first and second modes occur move to larger m values as q_{ej} decreases.
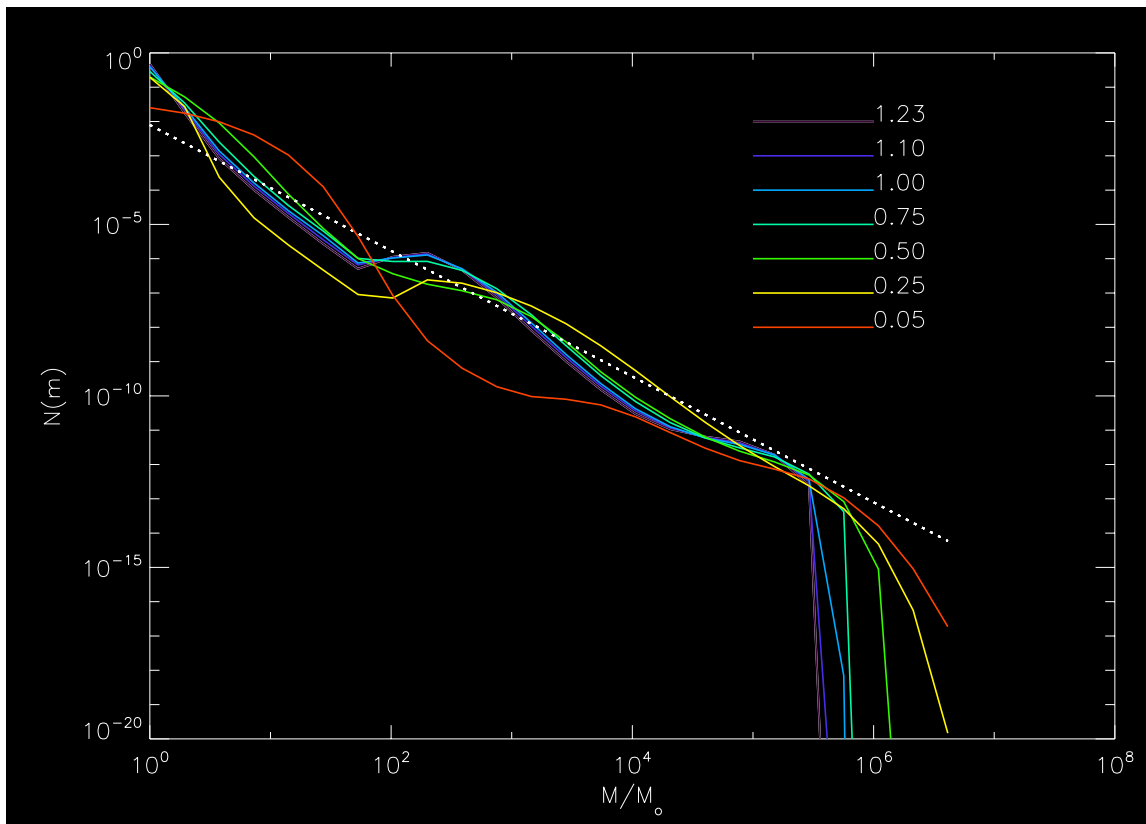
Figure 45. Final distributions for q_{ej} values from 0.05 to 1.23. As discussed in the assessment of the "wavy pattern," the value of q_{ej} does have an effect on the evolution of the distribution.

Next, I investigate the possibility that the observed distribution is merely the small range that coincides with a mode.   This possibility can be dismissed because the size range of observed clump-associated features spans over 2 orders of magnitude (Figure 46). Because the critical mass ratio for accretion in the F ring is 100 (Ohtsuki 1993, Canup and Esposito 1995), modes space out at approximately factors of μ_{crit}. If $\mu_{crit}=100$, but the span of sizes is a factor $\sim 10^6 >> 100$, then the observed distribution cannot be a subsection of a larger multimodal distribution that coincides with the width of a mode. This is the case here.
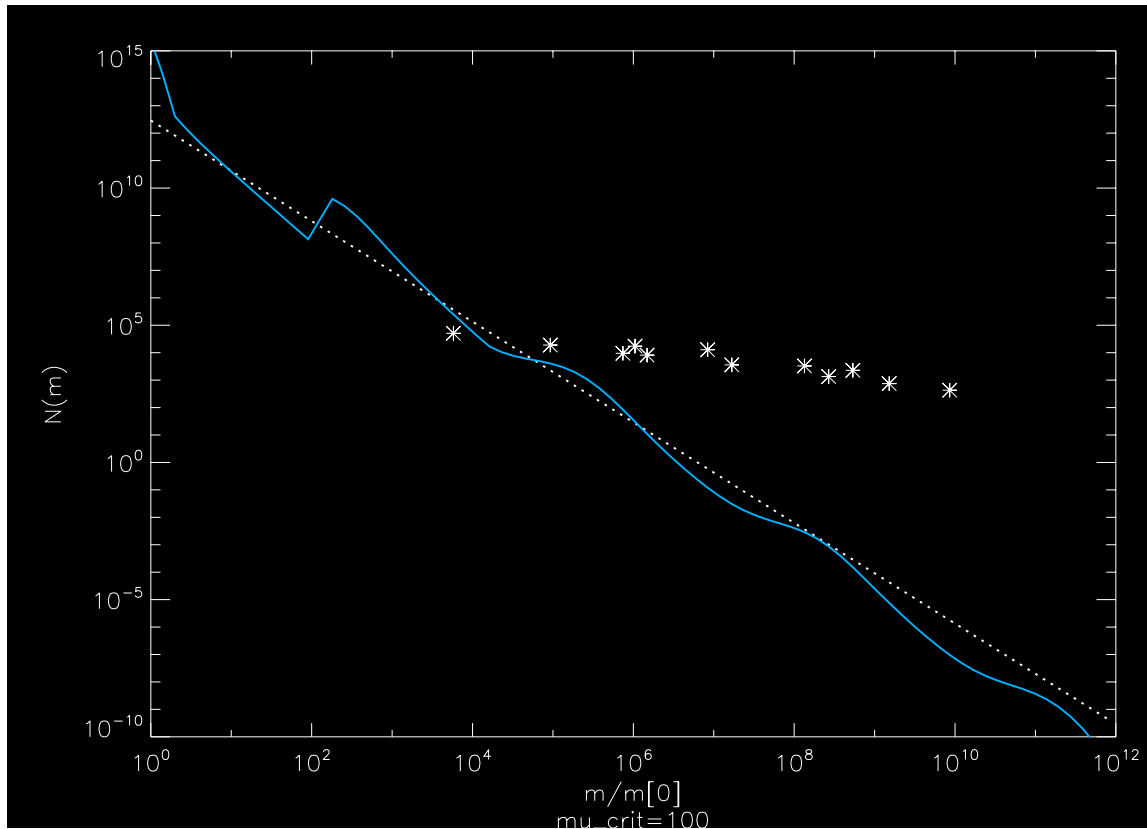
Figure 46. The observed distribution compared to the multimodal quasi-steady state of the model. The observed features in the F ring span a size range of six decades, so they cannot correspond to a mode that has a shallow power law index for ~ 2 orders of magnitude in size.

After the investigation into the simple methods available for changing the outcomes

of my model, I proceed to drastically change a principal component of the physics of the

system, namely accretion. The most plausible way to increase the number of large bodies

and flatten the size distribution is to increase accretion of specifically these large bodies.

The physical mechanisms possible would increase the effective collisional cross section,

thus increasing the collision frequency ($K_{accr} \approx \sigma v$). Unlike increasing the collisional

frequency by increasing the collisional velocity, which at best scales as $m^{-1/6}$, cross sections

scale with the size of the object, which preferentially allows larger bodies to grow faster.

First, I change the simple geometric cross section to include a gravitational focusing factor,

$\alpha_{GF} = \left(1 + \left(\dfrac{v_{esc}}{v_{rel}}\right)^2\right)$. This changes the scaling of the cross section with mass:

$$K_{accr} = \sigma v_{rel} = \pi (r_1 + r_2)^2 v_{rel} \propto m^{\frac{2}{3}}$$

$$K_{accr,GF} = \alpha_{GF} \sigma v_{rel} = \left(1 + \left(\frac{v_{esc}}{v_{rel}}\right)^2\right) \pi (r_1 + r_2)^2 v_{rel} \propto m^{\frac{4}{3}}$$

Equation 25

Equation 25 describes how including a gravitational focusing factor for a body scales its

collisional frequency, K, as $m^{4/3}$, which allows larger bodies to accrete more efficiently.

However, the increase in effective accretion rate does nothing to affect the overall

evolution of the model.

I further increase the collisional cross section my increasing the effective body size

to be described by the Hill radius of the body, $R_{Hill} = a_{Fring} \left(\dfrac{m}{M_{Saturn}}\right)^{1/3}$. This scales with mass

as the geometrical cross section does ($m^{2/3}$) but is larger by a constant factor,

$a_{Fring}/M_{Saturn}^{1/3}=0.17$.   Thus, the use of the Hill radius to describe the body size increases

the collision frequency at a constant rate. Coupling Hill radius and gravitational focusing

factor does increase accretion for large bodies in the system, but, as seen in Fig 47, the

resulting distribution oscillates in time in the size range between mode 1 and mode 2. This

is not a match the to observations, though. These two physical mechanisms do not

sufficiently boost accretion to match the modeled distribution to the observed one.
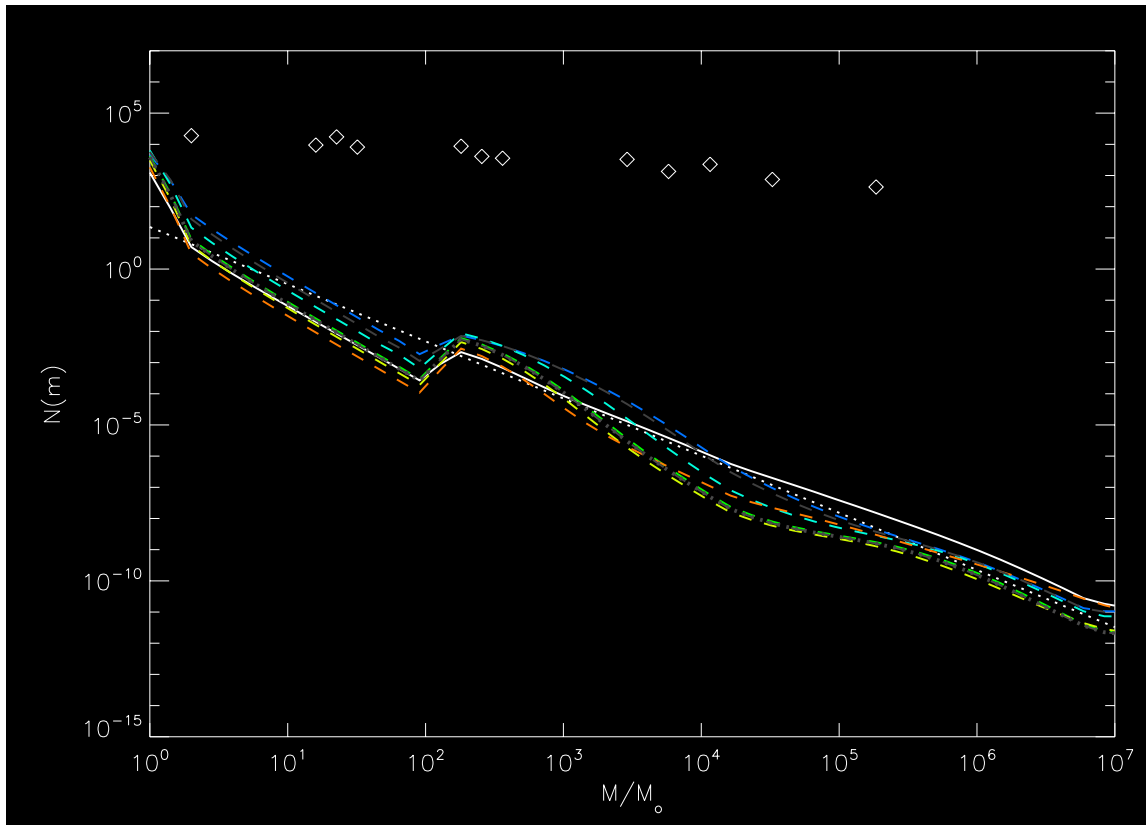
Figure 47. Model using the Hill radius as the physical size of the body and including a gravitational focusing factor for collisional cross section. This does increase accretion for large bodies in the system, but oscillates in time between modes 1 and 2. Multiple colored lines mark out different snap shots to show the temporal oscillations in the distribution. Diamonds are the UVIS-observed distribution of Moonlets and Icicles.

I artificially increase accretion to place a threshold on the amount of increased

accretion necessary to build larger bodies and match the modeled distribution to the

observed one. I set a threshold size, m_{LB}, above which bodies accrete at an accelerated rate.

For bodies below the threshold size, accretion proceeds as described in Section 3.1.2:

$m_1/m_2 > \mu_{crit}$: Accretion =100% of colliding mass

$m_1/m_2 < \mu_{crit}$: Accretion =0%

For bodies above this threshold size, the following conditions apply:

$m_1/m_2 > \mu_{crit}$: Accretion increased by factor X_{accel}

$m_1/m_2 < \mu_{crit}$: Accretion increased by factor $X_{residual}$

First, I set X_{accel}=1 and only vary $X_{residual}$ from 0.001 to 0.1, which only increases the

accretion for collisions below μ_{crit} by 0.1% to 10%. This makes no difference in the

evolution of the system. Keeping $X_{residual}$ =0.001, I set X_{accel}=10. With this increased

accretion, the familiar multimodal behavior does not develop but the general trend of the

distribution does not flatten out to that of the observed distribution.   Next, I change the

amount of accretion allowed regardless of mass ratio of colliding bodies such that

$X_{residual}$=50% of colliding material with $\mu<\mu_{crit}$ and $m>m_{LB}$ accretes. This again, makes

accretion easier for large bodies even when they encounter comparable-sized bodies. A

collision between two large bodies under these conditions would not completely disrupt

the incoming mass, keeping more larger bodies in the distribution as evolution proceeds,

which in turn decreases the power law index of the overall distribution. Figure 48 displays

the model results with X_{accel}=10 and $X_{residual}$=0.5. The distribution is a broken power law

with the slope at smaller sizes shallower than that at larger sizes. To create a model

consistent with observations, what is the minimum value of X_{accel} required? At X_{accel}=100,

the broken power law develops three sections. At X_{accel}=1000, the power law that covers

the middle of the size range has the lowest q value and looks similar to the observed

distribution (Figure 49). The minimum value of X_{accel} required to remove multiple modes from the system and begin to flatten the smaller-size end of the distribution is $X_{accel}=6$.
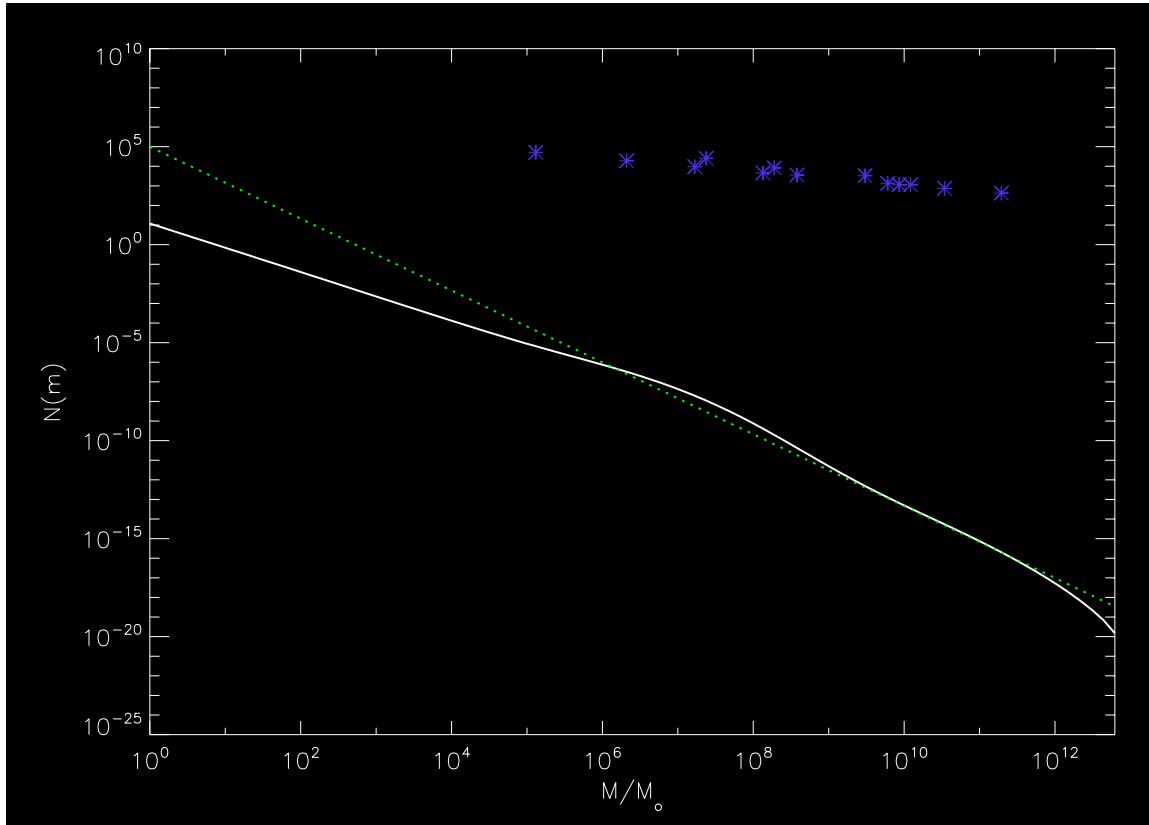
Figure 48. Model results with $X_{accel}=10$ and $X_{residual}=0.5$. Model results (solid white line) do not match observation (blue *) because the model is still too steep, even at smaller-sized bodies. Green dashed line is the model's initial distribution.
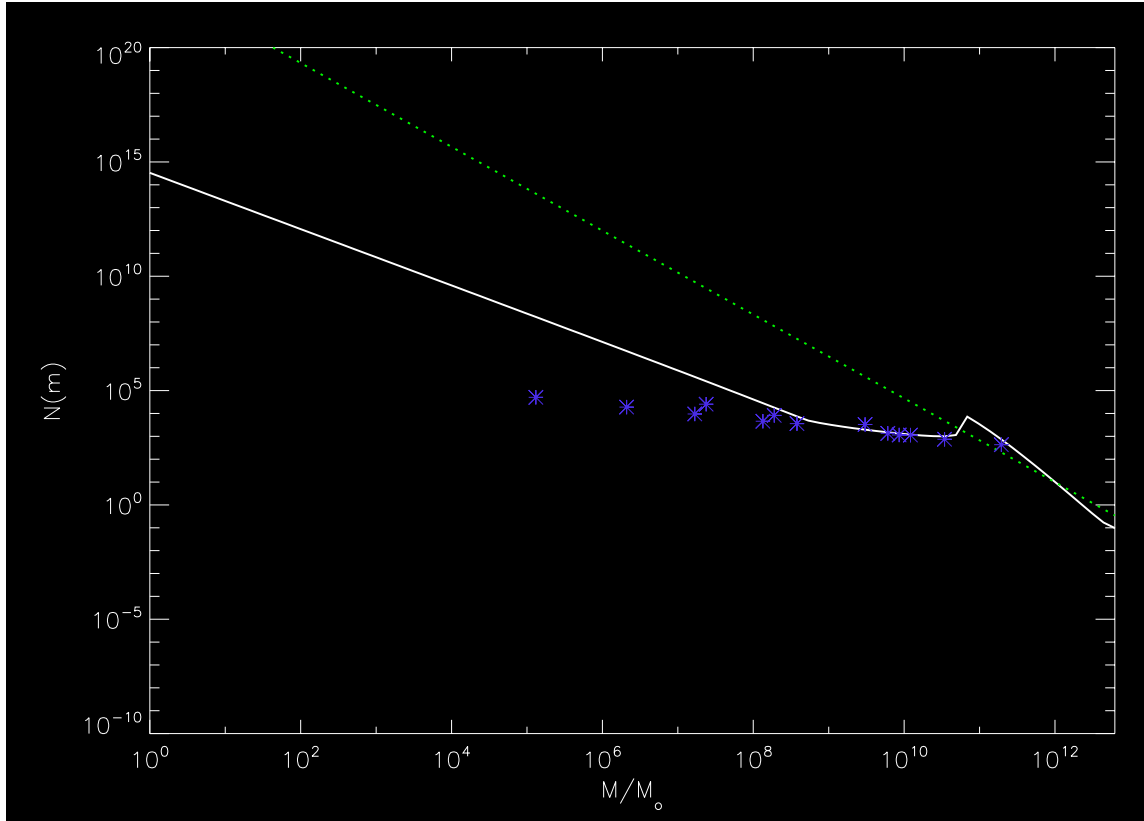
Figure 49. Model results with X_{accel}=1000 and $X_{residual}$=0.5. Model results (solid white line) appear consistent with a portion of the observed distribution (blue *). The power law that covers the middle of the size range in the model has the lowest power law index and looks similar to the observed distribution for those sizes. Green dashed line is the model's initial distribution.

The evolution of the distribution is also sensitive to the size threshold for accelerated accretion. The value of m_{LB} is set relative to the critical mass ratio, $m_{LB} = \mu_{crit}^{X_{LB}} m_0$. Producing models with X_{LB} =0.1 through 5.0, I find that the smaller the value of m_{LB} the larger the range over which the distribution has a shallow power law index. X_{LB} must be less than 3.0 in order to produce the flattened portion of the distribution. Thus, the smaller the critical size above which a body has increased accretion, the more bodies in the distribution that experience increased accretion.

Tuning the parameters mentioned above to match the observed distribution of clump-associated features in the F ring, I find accretion must be increased by a factor $X_{accel}>6$ for bodies $m>m_{LB}$ and $\mu>\mu_{crit}$, $X_{residual}=0.5$ for bodies $m>m_{LB}$ and $\mu<\mu_{crit}$, and the critical body size must be $m_{LB}<\mu_{crit}^{3.0}m_0$.

Figure 50 displays the best-fit (by inspection) model to the observed incremental distribution. The best-fit model has the following parameters:

$X_{accel}=1000$,

$X_{residual}=0.5$

$m_{LB}=\mu_{crit}^{2.5}m_0$

size range: 10m – 40 km

Collisional Cross Section: includes R_{Hill} and gravitational focusing factor for bodies $>m_{LB}$
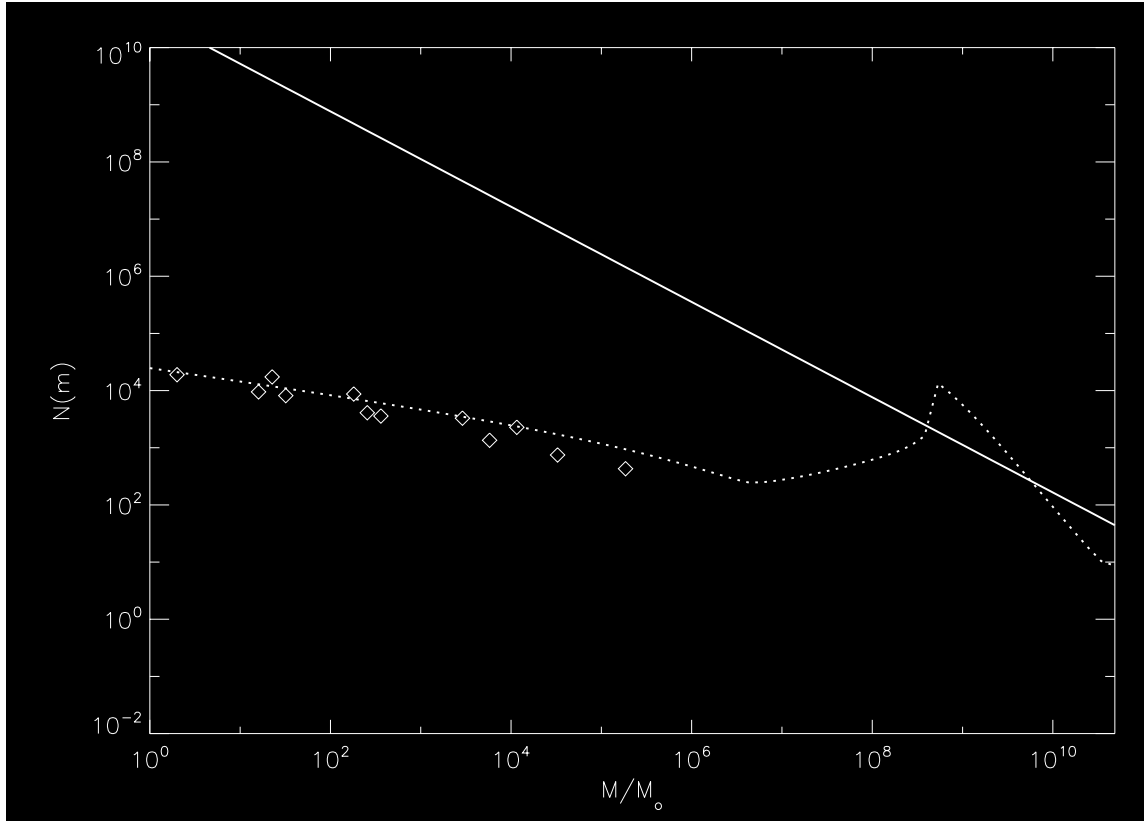
Figure 50. The best-fit model to the observed incremental distribution achieved by increasing accretion within the binary accretion model. The best fit model has the following parameters: X_{accel}=1000, $X_{residual}$=0.5, $m_{LB} = \mu_{crit}^{2.5} m_0$, size range of 10m – 40 km, collisional cross section that includes R_{Hill}, and gravitational focusing factor for bodies >$m_{LB.}$ It is important to note here that "best-fit" is by inspection. When tuning the values of : X_{accel}, the best fit was apparent by eye, no statistical assessment required. Additionally, because this method has no plausible physical basis, an approximation to the "best-fit" parameters is sufficient.

No plausible physical mechanisms or combination thereof support this best-fit model, however. Gravitational focusing and Hill radii do not increase the accretion anywhere near a thousand-fold. Furthermore, while consistent with UVIS observations, it is inconsistent with Imaging results. If there was, in fact, a mode at m/m_0=10^9 (corresponds to r~few km), then ISS would have seen many moonlets because this size is above their detection threshold. To create a physically-plausible model that is consistent

133

with observations, we must include an additional term that specifically accounts for the production of large bodies.

3.1.5 **Addition of a production term to the coagulation equation**

In order to flatten the slope of the modeled distribution to match UVIS observations of clumps, I introduce a production term to the coagulation equation. Recalling Equation 21, we can write the coagulation equation for binary collisions including accretion and fragmentation. When numerically implemented, this equation does not produce a distribution consistent with F ring observations. The incremental distribution of observed clump-like features in the F ring has a much smaller (shallower) power-law index than my simple binary collision model (Figure 46), thus an improvement to the model is data driven. Furthermore, attempts in the last section to match the model to observations comparisons show that accretion must be easier than fragmentation by a large factor to seriously affect the modeled distribution. Exploration of mechanisms to increase production of large bodies led to a new view of enhanced aggregate construction that is motivated by work with Glen Stewart and Esposito et al (2012)'s predator-prey model.

As reported in Section 3.1.4, a drastic increase in the accretion coefficient efficiently builds larger bodies and flattens the modeled distribution to match observations. At a factor of 1000, the increase is implausibly large. Another method that could boost accretion is perhaps more physically plausible. Imagine a situation in which bodies larger than a critical size could experience enhanced growth while they are in a high-density region (HDR) of the ring. In this small region, such a body could efficiently sweep up smaller bodies or aggregates. An additional "production term" in the coagulation equation

134

incorporates this mechanism to create a modeled distribution consistent with observations.

Satellite wakes are a phenomenon created when a moon perturbs nearby ring particle orbits such that their streamlines create a pattern of compacted and rarefied regions. As discussed in the Introduction, familiar satellite wakes occur at ring-gap edges, but the moon Prometheus orbits just inside the semi-major axis of the F ring and creates a pattern of satellite wakes known as "fans." These fans, seen in Cassini images like Figure 51, are periodic regions of drastically increased surface density. The average optical depth of the F ring is 0.1, but in these regions is well above unity. These HDR arise when particle orbits crowd. Particles on the orbits pictured in Figure 52 create a HDR that travels at the orbital speed of Prometheus, but specific particles continue to move through the HDR and are not fixed with respect to it. Like a boat wake in the ocean, the structure (HDR or wake) moves at a speed different from that of the particles (ring particles or water molecules). This is the difference between pattern speed and particle speed, $v_{particle} \neq v_{pattern}$. Thus, a body passing though an HDR is unlike a bullet through a cloud.
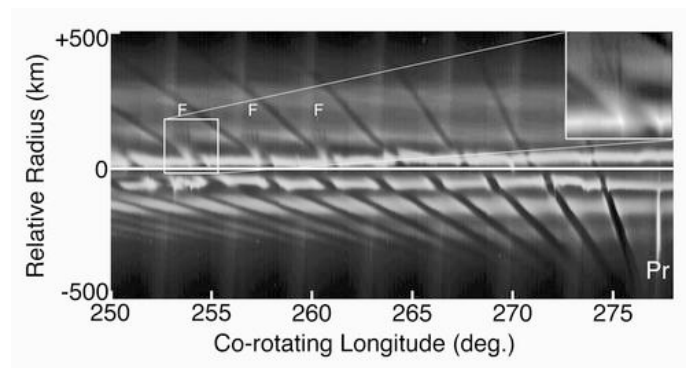
Figure 51. PIA12784: Multiple F-Ring "Fans". Bright areas are "fans" created by Prometheus, which has enhanced surface density. Image Credit: NASA/JPL/Space Science Institute
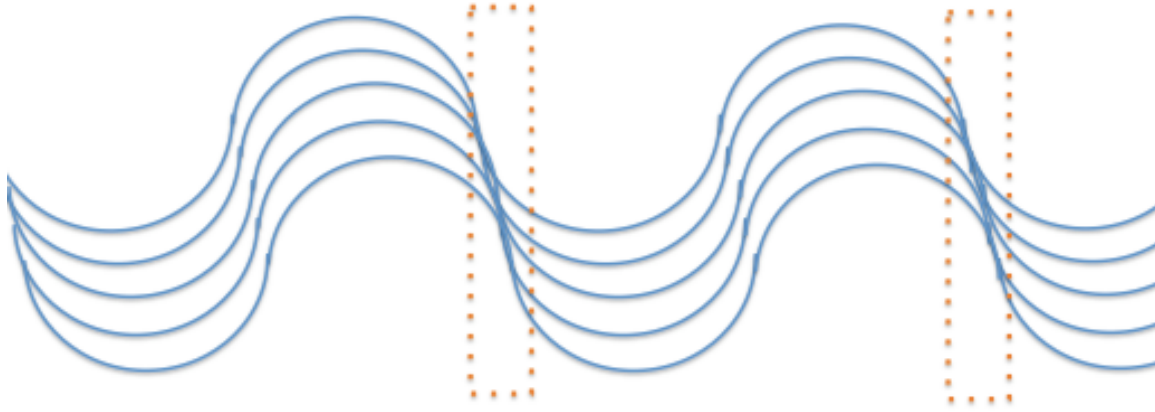
Figure 52. Satellite wakes. The blue curves are particle streamlines, which are perturbed by Prometheus to form the pattern of compacted and rarefied regions. The regions boxed by orange dotted lines are what are referred to as HDR in the text, where streamlines crowd to create increased surface density that can lead to enhanced growth of bodies passing through it.

When a body passes through a HDR it encounters a considerable increase in surface density, thus a considerable increase in collision rate. From Esposito et al (2012) (which they adapt from Eq 9 in Shu and Stewart 1985), the collision rate for a region of given optical depth τ is given by:

$$T_{coll} \approx \frac{T_{orb}}{4\tau}$$

Equation 26

For the average F ring optical depth of $\tau=0.1$, the time between collisions is $T_{coll}=10^5$ s, which is about one orbit. Meanwhile, for the highest F ring core optical depth observed in UVIS occultations $\tau=3.0$ (Albers, et al., 2012), $T_{coll}=4200$ seconds, which would result in 12 collisions per orbit if the entire ring were that optical depth. We assume that one of the HDRs is that optical depth and that the fan structure fills at best a quarter of an F ring particle orbit; therefore, these satellite wakes produce the equivalent of a three-fold increase in the number of collisions each particle experiences over the course of an orbit.

An increase in collisions damps the dispersion velocity. Considering the Toomre criterion for gravitational instability,

$$Q_{Toomre} = \frac{c_s \kappa}{\pi G \Sigma} < 1$$
,

<div align="right">**Equation 27**</div>

we find that a decrease in the dispersion velocity, c_s, results in instability, for optical depths near unity. Thus, increased collisional "sweep up" leads to gravitational instability and collective growth. Both are at work in these HDRs.

The next task in the derivation of a "production term" to add to the coagulation equation is to approximate the bodies in the HDRs. As discussed in Meinke et al. (2012), clumps in the F ring are likely azimuthally-elongated ellipsoids, like cigars. We can model the aggregate shape as a wire in the azimuthal direction and write down an expression for the characteristic surface density and line density of the cigar:

$$\sigma_{kitten}(x) = \frac{1}{\pi} \left(\frac{\sigma_0 w^2}{w^2 + x^2} \right)$$
$$\lambda_{kitten} = \int_{-\infty}^{\infty} \sigma_{kitten} \, dx = \sigma_0 w$$

<div align="right">**Equation 28**</div>

where $x = r - r_0$ (the radial direction) and σ_0 is the incoming body's surface density. The production term describes the one-dimensional gravitational infall of material onto a body in a HDR that leads to enhanced growth of that body. The collapse is along the radial coordinate in a circular shear flow with self-gravity. Figure 53 is a cartoon of the infall and the coordinate system.
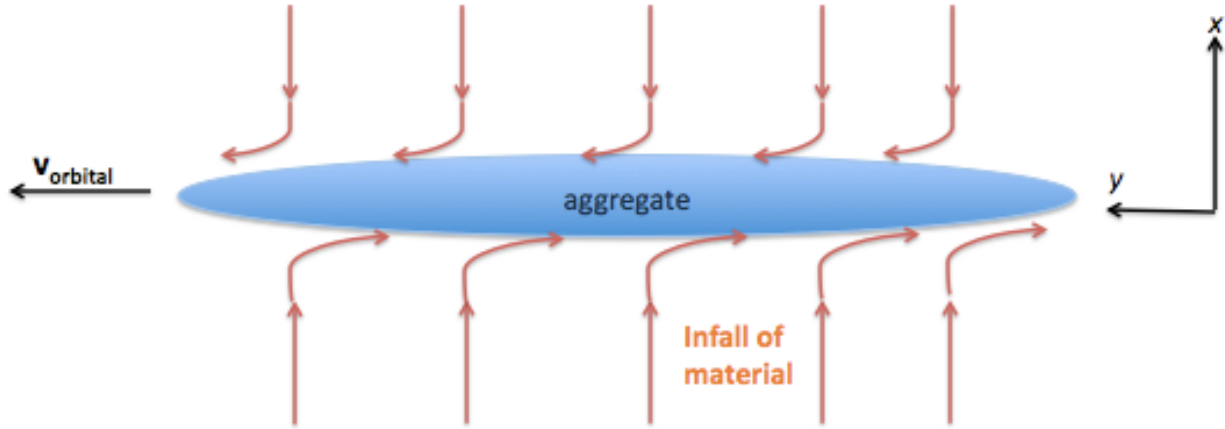
Figure 53. Radial one-dimensional infall of ring material onto a cigar-shaped aggregate as it passes through a HDR. The radial coordinate is x, azimuthal is y. This is in the aggregate's coorbital reference frame.

From linearized fluid equations, neglecting azimuthal derivatives and assuming a body only spends a fraction of an orbit in a HDR, we can derive a simplified expression for the increase in the surface density of an aggregate. Then, we integrate over the radial width of the aggregate to find the enhanced mass per unit length:

$$\Delta\lambda = \frac{G\Sigma}{w}t_{HDR}^2\lambda_0$$

Equation 29

where w is half the body's radial width and t_{HDR} is the amount of time spent in the high-density region (1/4 of an orbit). The initial mass per (azimuthal) length of the body is $\lambda_o=m/L$, where $L=2wR_{axes}$ (the radial width times the axial ratio). Later, we use Σ=40 g cm^{-2} (that of the A ring) for the HDR. Figure 54 illustrates the scenario where a body approaches a HDR, grows as it passes through the HDR and comes out the other side a larger aggregate. Remember that the velocity at which the body moves through the HDR, $v_{pass}= v_{orb} - v_{HDR}$, is related to the difference in the angular speeds of F ring material and the moonlet wake pattern speed $\Delta\Omega = \Omega_F\text{-}\Omega_{HDR}$ and is not the relative speed at which particles

collide. Thus $v_{rel} \neq v_{pass}$. Putting together the change in line density and the speed at which

the body passes through the HDR, the change in mass of a body as it moves through the

HDR is:

$$\Delta M = \Delta \lambda v_{pass} t_{HDR}$$

<div align="right">**Equation 30**</div>
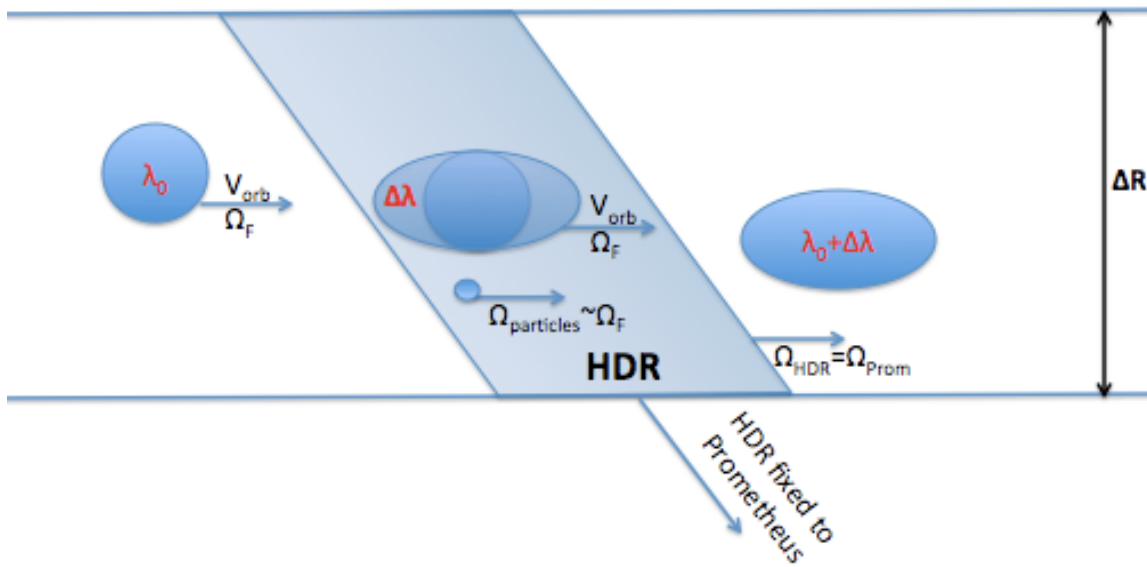
Figure 54. Cartoon depiction of aggregate growing as it passes through a HDR.

The production term A_{HD} modifies eqs 11 and 21 to a new expression for the

coagulation equation:

$$\frac{dN'(m,t)}{dt} = A_{HD} + A_{Gain} - A_{Loss} + F_{Gain} - F_{Loss}$$

<div align="right">**Equation 31**</div>

A_{HD} is the change in number of bodies of a particular size (m) per time (t) as a result of

individual bodies increasing in size while in HDRs. An individual body of size m grows to a

size $m_{aggregate}$ by sweeping up bodies smaller than m_{swarm}, thus increasing the number of

bodies of size $m_{aggregate}$ and decreasing the number in the swarm size range ($<m_{swarm}$).

Thus, for bodies of size *m* entering the HDR with relative orbital speed described by v_{pass}

and increasing by *dm* we can describe the increase in the number of bodies of size *m+dm*

as:

$$A_{HD}(m + dm) = n(m)\left(\frac{\Delta\lambda v_{pass}}{dm}\right)$$

Equation 32

This increase in bodies of size *m+dm* is balanced by the loss of bodies swept up in the new

aggregate:

$$A_{HD}(m) = n_{swarm}\left(\frac{A_{HD}(m + dm)m\,dm}{\displaystyle\int_{m_0}^{m_{swarm}} n_{swarm}m\,dm}\right),$$

Equation 33

where n_{swarm} describes the size distribution of bodies in the swarm. The size distribution of

the swarm is the size distribution of the fragments redistributed by binary collisions. The

discretized form of A_{HD} is given by:

$$A_{HD_{i+1}} = A_{HD}(m_{i+1}) = n_i\left(\frac{\Delta\lambda v_{pass}}{m_{i+1} - m_i}\right)$$

$$A_{HD}(m = [m_0, m_{swarm}]) = n_{swarm}\left(\frac{A_{HD_{i+1}}m_{i+1}dm_{i+1}}{\displaystyle\sum_{m_j=m_0}^{m_{swarm}} n_{swarm,j}m_j dm_j}\right)$$

Equation 34

When I include this production term in the model, I find a quasi-steady state

distribution that is consistent with observations, as seen in Figure 55. The important

tuning that is required of this term is the threshold between the upper size of bodies in the

"swarm," r_{swarm}, and the lower size cutoff of the bodies that undergo enhanced growth, $r_{moonlet}$. Allowing $r_{swarm} = r_{moonlet}$, I can establish the size of bodies in the F ring that contribute to larger moonlets and the size of those moonlets. Figure 566 is a comparison of this model with different values of r_{swarm} (2 m, 20 m, and 200 m). As the figure clearly shows, the smaller the value of r_{swarm}, the worse the match to observations. No distribution at $r > r_{swarm}$ develops that spans a wide enough range of sizes or has a small enough power law index to match observations. The comparison does demonstrate that the larger the value of r_{swarm}, the better the match to observations appears. I have attempted models with many values of r_{swarm} to tune the best match to observations, the best of which is in Fig 55. The model is consistent with observations when r_{swarm} is larger than the largest icicle observed (~640 m). Thus, the features reported in Meinke et al. (2012) and Section 2.4 are members of the "swarm" and contribute to the enhanced growth of even larger moons.
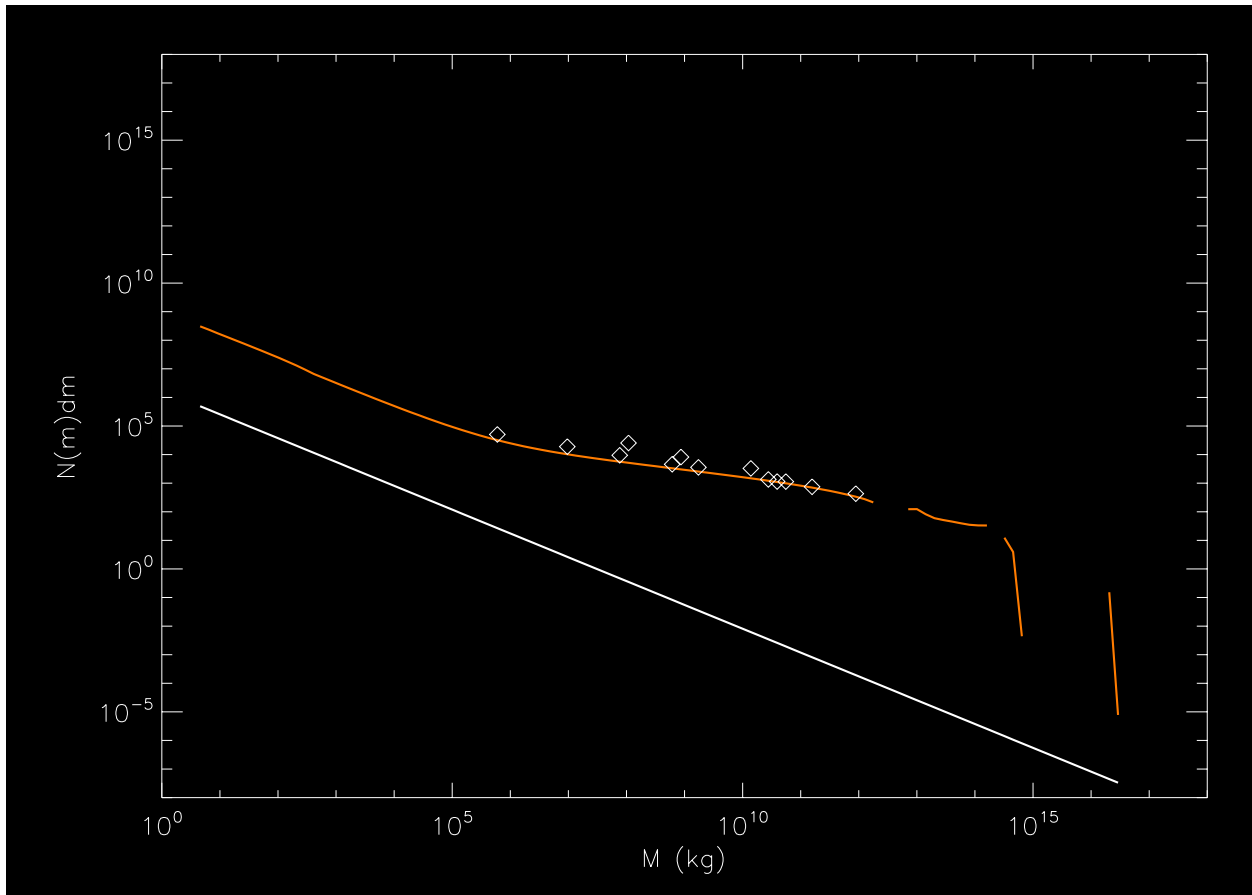
Figure 55. Model of F ring evolution including a production term. The incremental distribution model (orange line) matches the observations (white diamonds) best when the threshold size between the swarm of bodies swept up and bodies sweeping them up is r_{swarm}=640 m. The white line is the initial distribution of the modeled system.
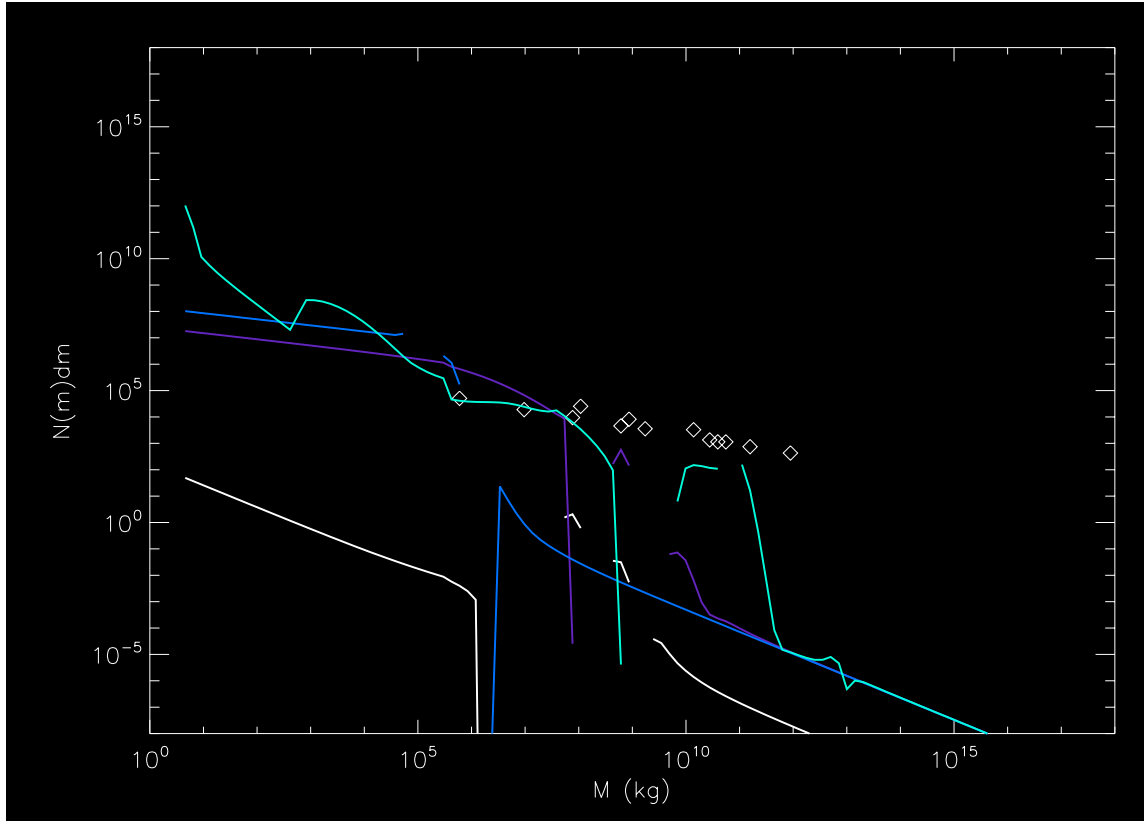
Figure 56. Comparison of models of F ring evolution including a production term with varying r$_{swarm}$ values. The incremental distribution models (colored lines) match the observations (white diamonds) better as the threshold size between the swarm of bodies swept up and bodies sweeping them up increases. The blue line has r$_{swarm}$=2 m, purple has 20m, and cyan has 200 m.

In Fig 55, the break in the distribution occurs at r_{swarm}. Below r_{swarm}, the distribution

is shallower than that of the binary accretion model alone. Above r_{swarm}, the distribution

breaks and then forms a "moonlet mode" of bodies a few kilometers in size. This moonlet

mode is transient. As the system evolves and the distribution below r_{swarm} flattens, the

moonlet mode grows then slowly erodes away. This behavior is consistent with rapid

buildup of large bodies due to enhanced growth followed by erosion via binary collisions

with the largest bodies (thus $\mu<\mu_{crit}$) in the swarm, the number of which increases as the

distribution of the swarm flattens. As Figure 57 shows, the model is consistent with

observations for r_{swarm}=640 m. The UVIS-observed distribution does not have a break in it,

so the model-predicted break must occur at larger sizes. Likewise, the number and size of

bodies in the moonlet mode is consistent with Imaging results. These could be like the

bodies seen and tracked for a few weeks and months (e.g., S/2004 S 6). To date, UVIS has

not observed any such body; therefore, I use Equation 9 from Section 2.5 to calculate an

upper limit of $\sim 10^4$ S/2004 S 6 –like bodies to be in the ring and to have gone undetected in

UVIS occultations. This upper limit on a body like S/2004 S 6, estimated size 3-5 km

spherical (Porco, et al., 2005), is in Fig 57.
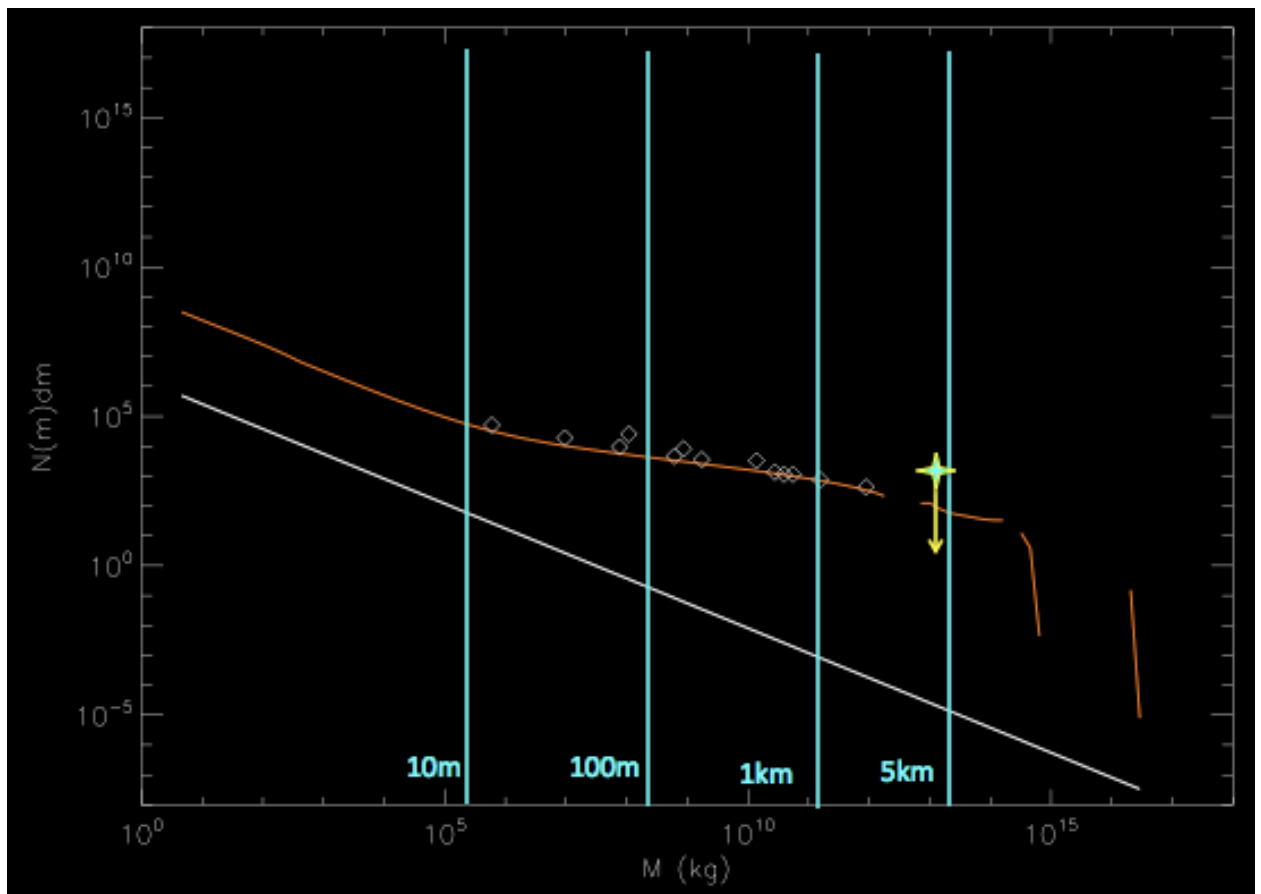
Figure 57. Model of F ring evolution including a production term. This is the same as Fig 55 but overplotted with radial sizes of bodies (vertical cyan lines) and the upper limit on the number of bodies like S/2004 S 6 (yellow star and arrow) The incremental distribution model (orange line) matches the observations (white diamonds) best when the threshold size between the swarm of bodies swept up and bodies sweeping them up is r_{swarm}=640 m. The white line is the initial distribution of the modeled system

The doubling time of the number of bodies of a given size larger than r_{swarm} is given by Equation 35 and plotted in Figure 58. This doubling time is with respect to the production term alone. Likewise, the numbers of bodies being swept up in the HDRs are decreasing at a rate described by the "halving time," Equation 36 and Fig 58.

$$T_{double} = \ln(2) \left(\frac{\Delta \lambda v_{pass}}{m_{i+1} - m_i} \right)^{-1}$$

Equation 35

$$T_{half} = \ln(2) \left(\frac{\displaystyle\sum_{i=\max(swarm)}^{i=\infty} \left[\left(\frac{\Delta \lambda_i v_{pass}}{m_{i+1} - m_i} N_i \right) m_{i+1} dm_{i+1} \right]}{\displaystyle\sum_{j=0}^{\max(swarm)} N_{swarm,j} m_j dm_j} \right)^{-1}$$

Equation 36
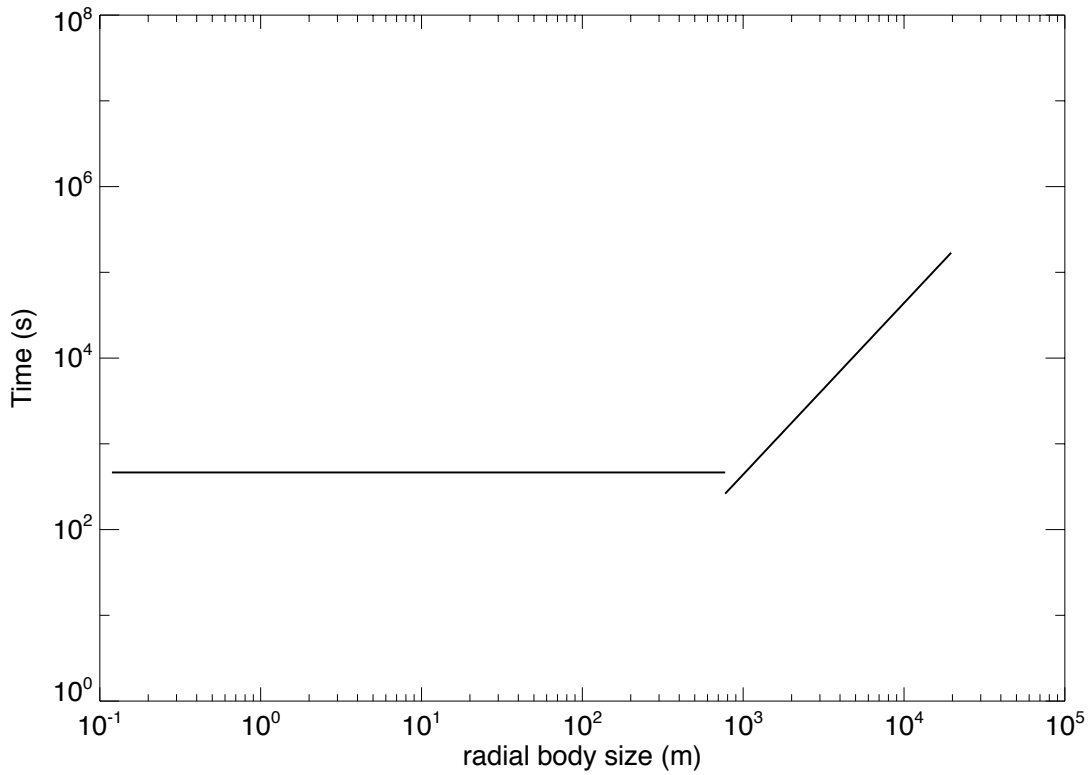
Figure 58. Doubling and Halfing times of enhance growth and swept up bodies, respectively. Halfing time is 464 s; doubing time ranges from 4 minutes to 2 days.

The halving time (464 s) is independent of body size, but the doubling time is dependent on body size. The time scale for most enhanced bodies to double their population is roughly a few hours to a few orbits. Since bodies spend less than a quarter of an orbit inside a HDR, these bodies will not double their populations. The doubling time is larger than a quarter orbit for any thing larger than 5.5 km, which is consistent with the dearth of observed bodies >5 km. In addition, there is likely a destruction mechanism not accounted for here. Enhanced growth in a HDR could be balanced by enhanced destruction due to perturbations from Prometheus or due to bodies ripping each other during close radial passages. The F ring is a complex system and requires multiple mechanisms to match models to observations; therefore, I do not believe the production term is the final word in modeling the ring's evolution.

In summary, the largest bodies in the system are the only ones that have increased accretion in the HDRs because gravitational instabilities form around them. The numbers of the smallest bodies decrease as the larger bodies sweep them up. This "flattens" the distribution by preferentially removing small bodies. Thus, the "kittens" that UVIS sees may themselves be swept up by even larger moonlets (e.g. S/2004 S 6).

The next step in the investigation of F ring particle-size distribution evolution is to include other processes at work in the ring into the model, namely porosity and compaction. From Cassini observations (Meinke et al., 2012; Charnoz, 2008), F ring material appears generally to clump together like a rubble pile rather than form solid, spherical moonlets. A loose aggregation of ring particles may compact when it collides with other ring material, which changes the evolution of the size distribution

3.2 **Expansion of the model to include compaction**

The UVIS-observed distribution of clump-associated features in Saturn's F ring motivates a new model for the evolution of the ring. BE02's bimodal results do not match the power law shape of the distribution, nor the shallow slope thereof ($2<q<2.5$) (see Section 2. 5). The model presented in this dissertation was undertaken in order to resolve the discrepancies between observations and BE02; however, after modeling accretion due to binary collisions that only accounts for the mass of each object (one dimensional), I expand the model to evolve across two physical characteristics (two dimensional) of each body: radial size and porosity. The observations of Moonlets and Icicles in the F ring have varying optical depths, indicative of varying porosities (Meinke et al 2012). Icicles have smaller optical depths, usually of the order a few tenths; therefore, the object allows some starlight to pass though because it has some porosity. Meanwhile, Moonlets are opaque in occultation, completely attenuating stellar signal to the background level, because they are more densely consolidated than an Icicle. Meinke et al. (2012) speculate that these observational characteristics of F ring features indicate an evolution of object density (porosity) as well as radial size. Thus, I now expand my model to evolve in two dimensions, accounting for density of each object as well as size.

The expansion of the model to include evolution of clump density is the only way the model changes. All initial conditions and physical parameters are the same as they were in the constant–density model. Laboratory experiments provide constraints on the outcomes of collisions between bodies of porous water ice. Love, et al. (1993) find that "[p]orosity is more important than strength in determining the outcome of disruption impacts." They perform hypervelocity impacts of soda lime glass projectiles into porous sintered aggregate

glass targets to find that the disruption threshold scales with porosity as *(1-P)$^{-3.6}$*. Thus, the model modifies the critical mass threshold that separates accreting collisions from fragmenting ones accordingly. The threshold mass ratio value for accretion is $<\mu_{crit}$ for "porous" and "fluffy" bodies, with the more massive body in the collision determining the threshold value. Stewart and Ahrens (1999) perform impacts on plaster of Paris (i.e., gypsum) with porosities in the range of 30-80%. They find fragments follow a cumulative size distribution of *$N_c dr= r^{-b}dr$, b=2.7*. Thus, I convert this value to a differential one with respect to mass and use it as the prescribed differential redistribution power law for fragments (*q_{ej}=1.23*) in the multi-density model. Further, Housen et al (1999) perform high velocity impacts into porous material to simulate impacts on asteroid Mathilde, where no ejecta blanket is observed (Chapman et al 1999, Veverka et al 1997, 1999). They find <2% of crater mass is ejected, which means compaction plays an important role for impacts or collisions on bodies with high porosities. The collision energy goes into compaction rather than disruption. The only caveat here is that material must not be near the most efficient packing state (like sand) for this to work; therefore, over time, bodies may compact to a "fully dense state," but this is not a concern for a system like the F ring where fragmentation is also a regular process.

Evolving the system over two dimensions is computationally-intensive, so I do not establish a vector of finely-spaced bins in density. Rather, I designate three possible density states: solid, porous, and fluffy. The porosities I associate with each of these density states are P_{solid}=0%, P_{porous}=30%, and P_{fluffy}=70%; therefore, because the "solid" body of the system is Prometheus ($\rho_{Prometheus}$=470 kg m^{-3}), the densities are compared to that moon: ρ_{solid}=470 kg m^{-3}, ρ_{porous}=329 kg m^{-3}, and ρ_{fluffy}=141 kg m^{-3}. Next, I prescribe

collision outcomes for density. The compaction of Icicles to occasionally form Moonlets motivates these prescriptions (Table 3). For accretion, the resulting body assumes the density of the denser object, and if two like-density bodies accrete, they compact to the next-denser state. For example, if a fluffy body collides with a porous body, the resulting body is porous. For fragmentation, the ejecta from each of the colliding bodies retains the density of its parent body. Thus, if a body of mass $2m_0$ and porosity P_{fluffy} collides with a body of mass m_0 and porosity P_{solid}, then twice as many fragments (determined by mass fraction in each state: $f = r_1^3 \rho_1 / \left(r_1^3 \rho_1 + r_2^3 \rho_2 \right)$, in this case $2m_0/3m_0$) have porosity P_{fluffy} as P_{solid}. Table 3 breaks down the outcomes by density for a pair of incoming colliding bodies.

accretion	H	M	L
H	H	H	H
M	H	H	M
L	H	M	M

fragmentation	H	M	L
H	H	f →H 1-f →M	f→H 1-f →L
M	f →H 1-f →M	M	f→M 1-f→L
L	f→H 1-f →L	f→M 1-f→L	L

Table 3. Prescribed density outcomes for collisions. The Bold font first row and first column of each table denotes the density if the incoming bodies. H means highest density, M medium density, and L lowest density. For fragmentation outcomes, f is defined as the fraction of incoming mass which goes to each state: $f = r_1^3 \rho_1 / \left(r_1^3 \rho_1 + r_2^3 \rho_2 \right)$.

Figure 59 shows the steady-state distribution for the model parameters described. Naturally, the three density states evolve according to the prescribed collision outcomes, which results in size segregation by porosity state. Bodies compact into higher densities, which in turn grow to larger sizes. Thus, the percentage of mass that is in the densest

149

states increases as it decreases from the more-porous states. To better track the mass segregation by density state, I report the resulting distributions with different numbers of density states. Figure 60 shows the results of a model with two density states. Each has a different critical mass ratio, which is why they each evolve to different multi-modal distributions, but the size segregation is apparent. The denser state (solid lines) dominates the distribution at larger-sized bodies, while the more porous state dominates the smaller end of the size range. Although computationally expensive, I increase the number of density states in the model. Figure 61 is a model with five density states that follow the same collisional outcomes described above. The size segregation seen in the three-density model is exaggerated here. The smallest objects are the least dense, and the largest objects are the densest. At intermediate densities, the number of bodies of a particular size self-segregate, but the middle density state dominates the first mode of body size (see Section 3.1.3). The first mode size of this multimodal distribution would be the bodies most likely to be observed because of both their size and their numbers. This is consistent with 90% of Meinke et al. (2012)'s clump-associated observed features being Icicles, as these structures are speculated to be loosely-aggregated bodies. Only 10% of their reported features are opaque Moonlets, bodies consistent with the densest state reported here, which dominate the larger sizes end of the modeled distribution in Fig 59 through 61.
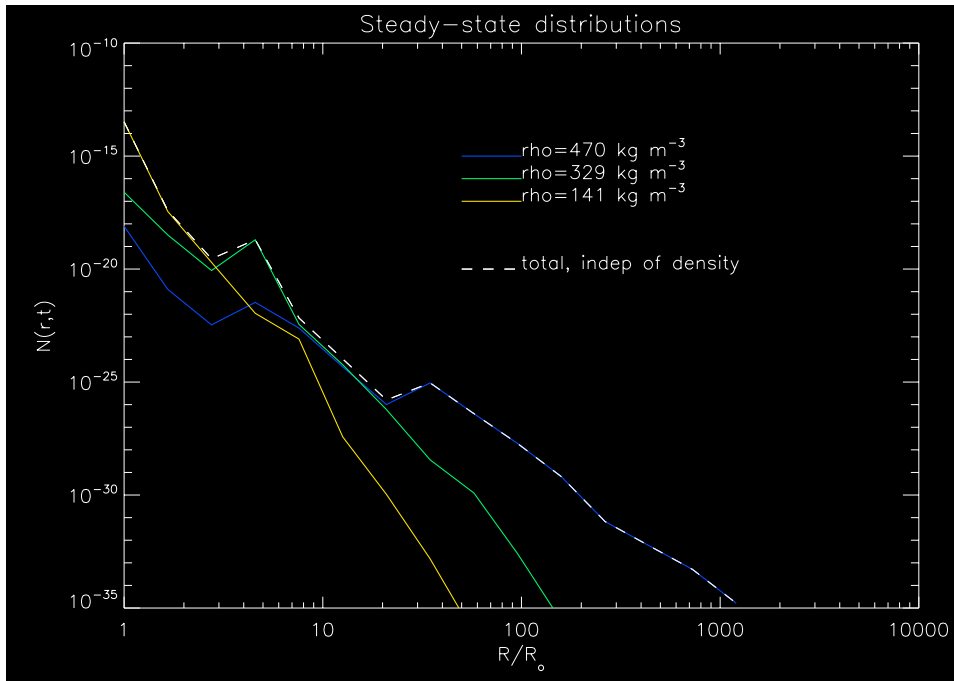
Figure 59. The steady-state distribution for the model parameters described in the text and collision outcomes from Table 3.
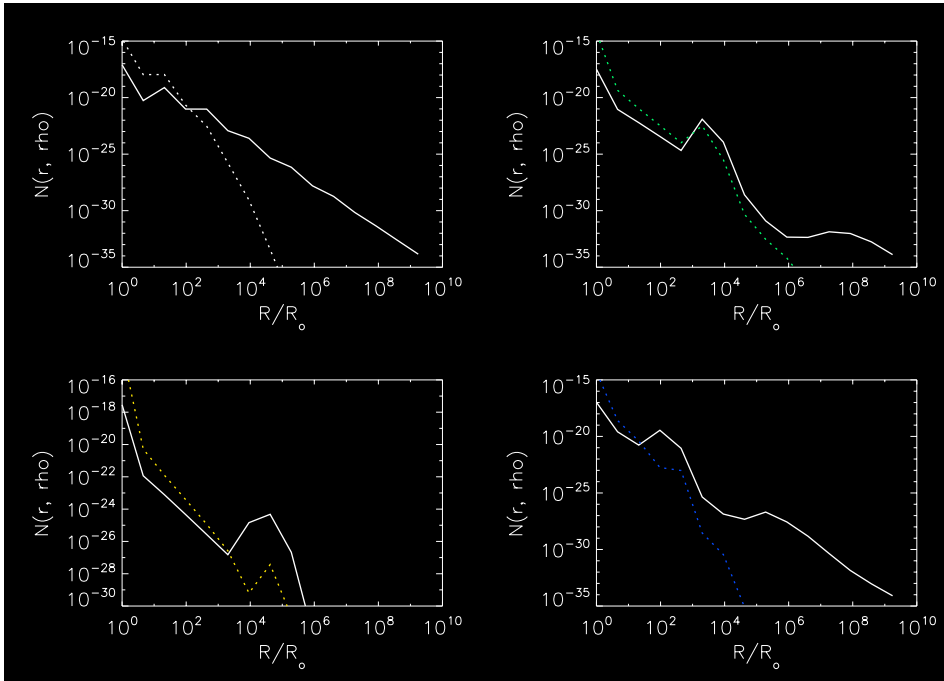
Figure 60. The quasi-steady state distributions for models with two density states. Starting with the upper left panel and moving clockwise, the critical mass ratio for each model is: 10, 10^3, 10^2, and 10^5. In each, the dotted colored line is the more porous (lower density) state, while the solid white curve is the distribution of the lower porosity (i.e. higher density) state.
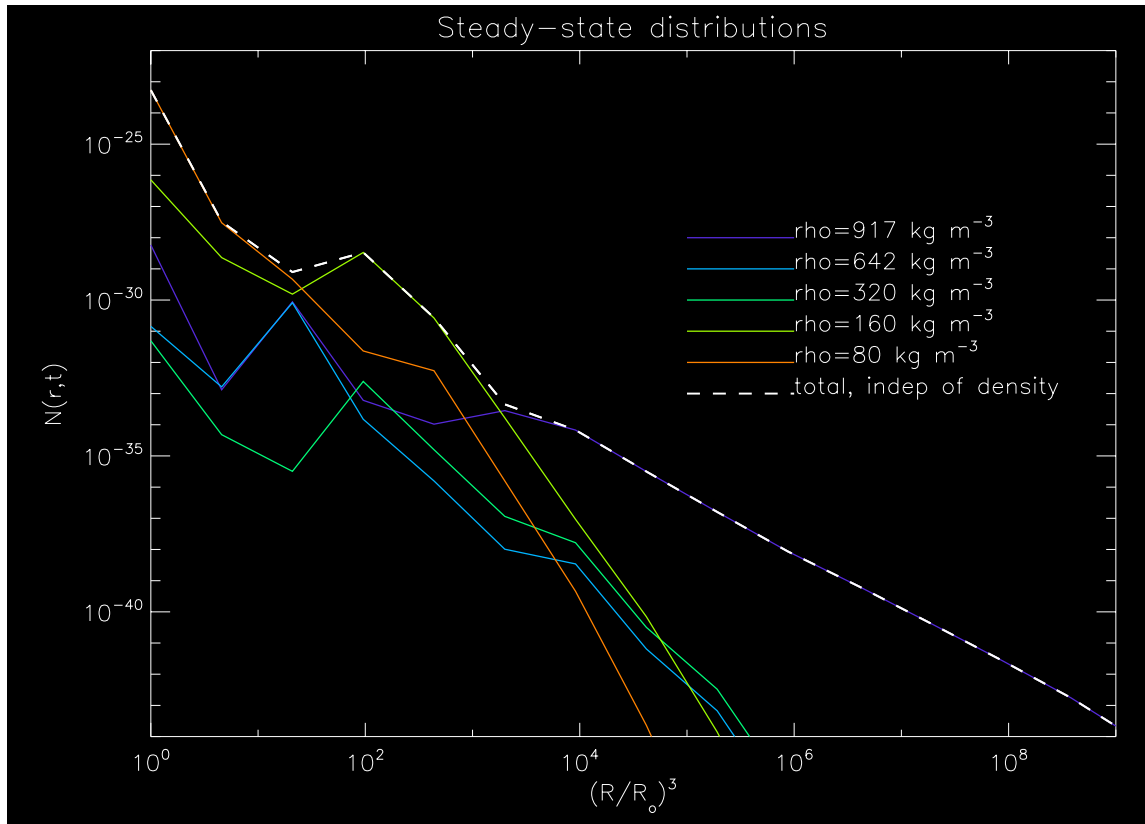
Figure 61. The quasi-steady state differential distribution for a model with five density states. Each colored solid line is of the distribution of one of the density states, as listed in the legend. The white dashed line is the quasi-steady state distribution of the entire system, coadded across density states.

As with the constant density model, I investigate the effect of different initial distributions on the final distributions. Figure 62a and b show the final distributions for each density state plotted over the various initial distributions. The initial distributions are broken power laws rather than the standard continuous power law previously used for this model. From inspection, it is clear these all evolve to the same final distribution. This is most obvious with the coadded distribution for each, which is consistent with the results for the constant density model. The steady state distribution of these models is insensitive to the initial distribution.

153
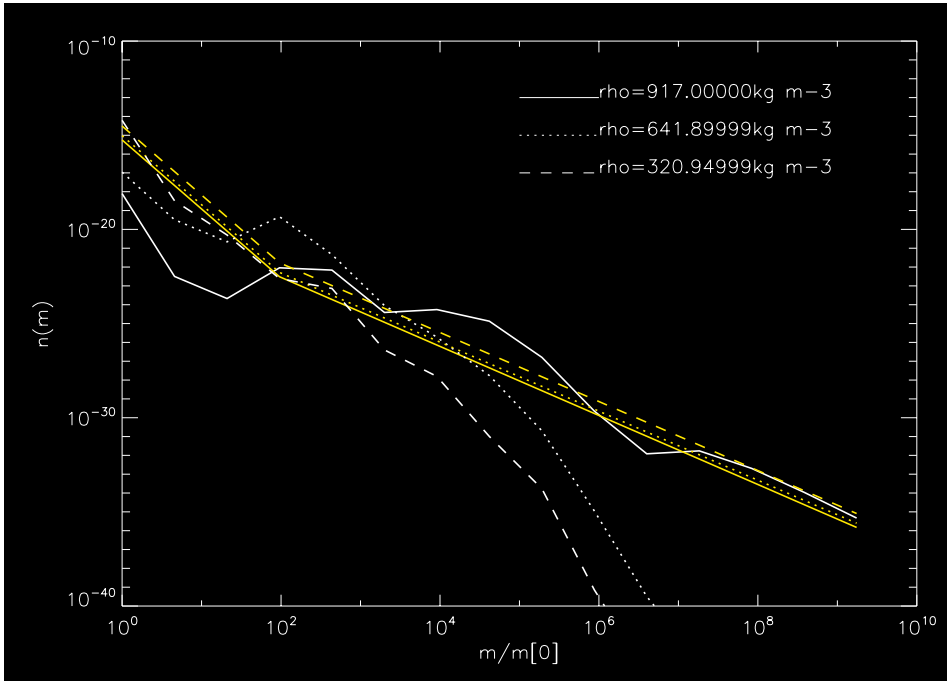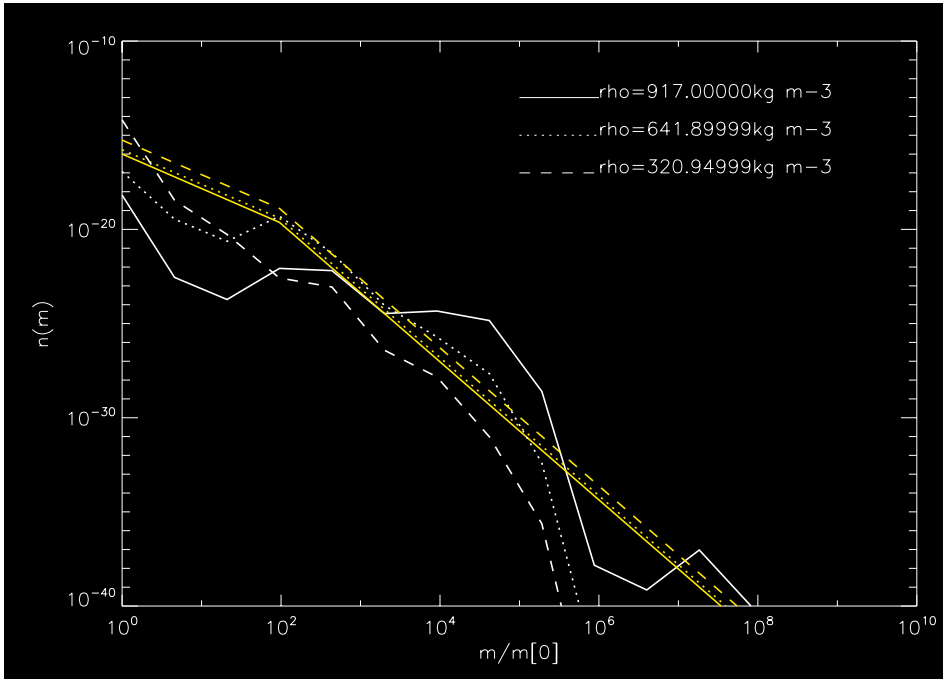
Figure 62. The final distributions (white) for each density state plotted over the various initial distributions (yellow). The initial distributions are all broken power laws, but the final coadded distributions have all evolved to similar multimodal shapes.

Upon examination of each density state independently I find that each has a multimodal shape, and when coadded by size (*n(r)* over all densities), I recover the same distribution as from the constant density model, *n(m,t)* (Figure 63). Consequently, modeling the distribution of F ring clumps by allowing for compaction does not match the observed distribution. Thus, the original motivation for this model does not come to fruition, but see the previous section for the effect of enhanced accretion in a high-density region; however, this expansion of the model opens up a wide range on investigations. With different physics governing the collisional outcomes for different density states, one can use this model to predict the probability of creating a solid, coherent object like a moon. Further, one might introduce high-density seed to the model in order to stimulate growth. In this way, this expansion can be used for other systems of bodies where compaction is also important, such as asteroids and planetesimals.
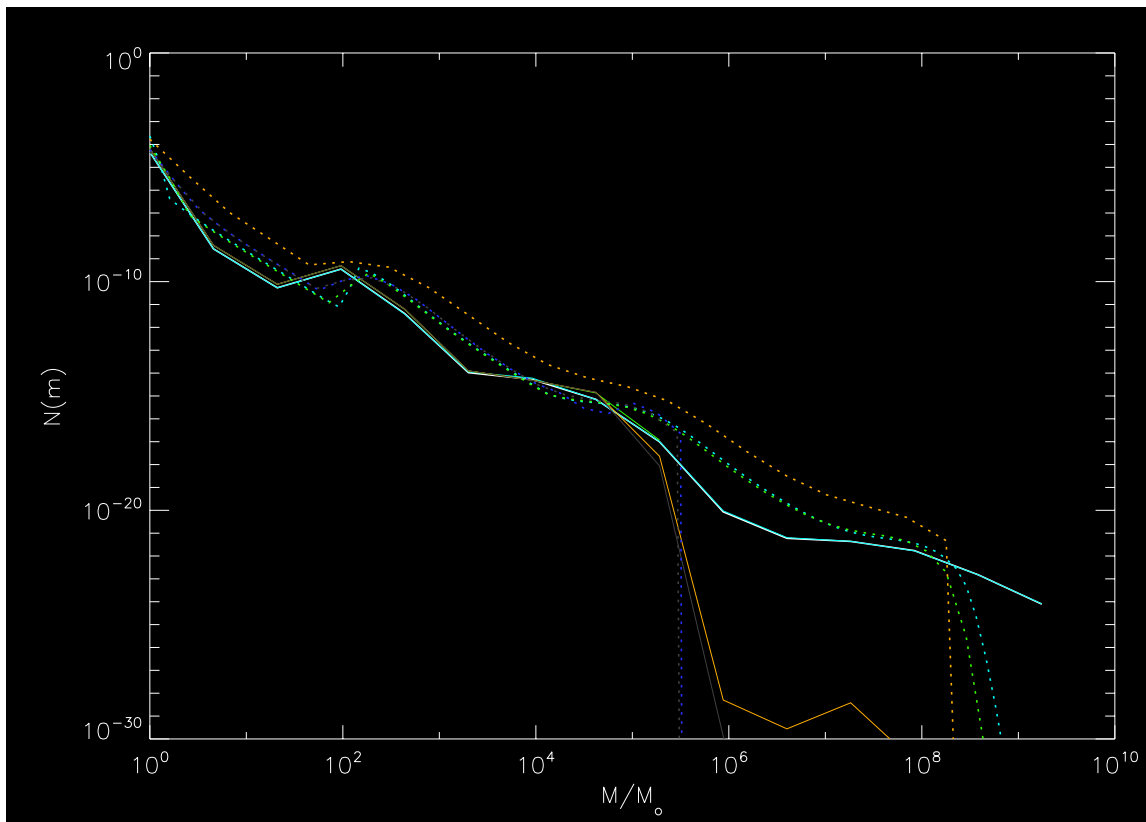
Figure 63. Coadded multi-density (solid lines) models compared to constant-density (dotted) models, all of which have appeared in other figures throughout this dissertation. Both types evolve to multimodal distributions. The differences among these are that some have an upper size cutoff (see Section 3.1.4) and the multi-density models have mode locations at a slightly smaller mass than the constant-density model does (due to summing and plotting by object mass rather than radius because lower density objects skew the distribution to smaller masses).

3.3 **Comparison of model results to those of BE02**

Because BE02 motivated this model, I compare it to the results of my model. BE02 reported an initially continuous size distribution evolves toward a bimodal distribution under the conditions of a "tidally-modified" region. My results agree, but they are not "bimodal" over the size range explored (Figure 64). Rather, the system evolves toward a "multimodal" distribution, where the modes occur at body sizes that scale by the critical mass ratio. In addition, BE02 conclude from their model that the larger mode of the final state represents a belt of moonlets (~1 km) as proposed in Cuzzi and Burns (1988). I find that modes may represent possible "clump" belts, but these are transient and may be very loosely accumulated; however, bodies in the larger modes are denser and may represent the evolution of a sparse population of moonlets in the F ring. Finally, BE02 predict that complete disruption of loosely-bound, larger moonlets can give rise to burst events observed by Showalter and in ring plane crossings. Combining my model and Meinke et al (2012) observations and conclusions, burst events might be just the release of loosely-bound outer layers of clumps before they compact into denser, longer-lived bodies.
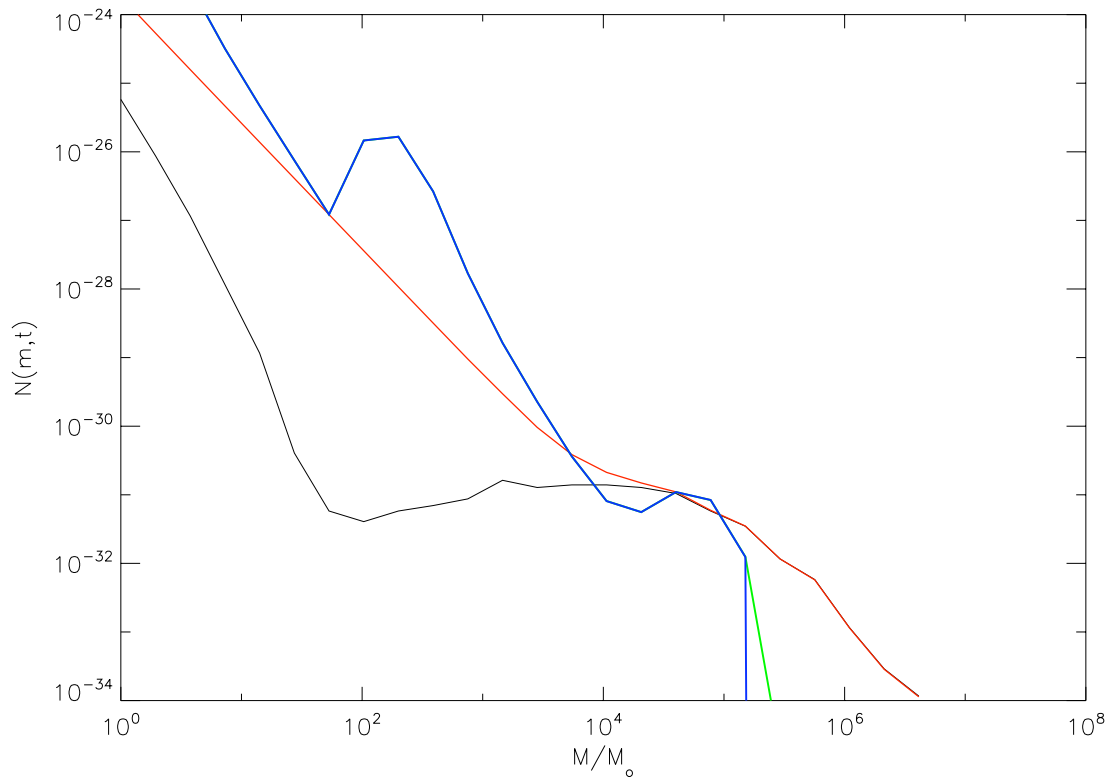
Figure 64. Binary accretion model described in this dissertation, using the BE02 model result (adjusted to be "number density" in the F ring rather than the reported number) as the initial distribution (black). The blue multimodal curve is the quasi-steady state that evolves from the BE02 result. The red curve is an intermediate stage of evolution; obviously, the population of smallest bodies grows the fastest.

The model presented here is tuned to Saturn's F ring, but many astrophysical

collisional systems exist that could be described using this model. Within the Solar System,

there are three other prominent ring systems. In addition, the Asteroid Belt and Kuiper

Belt are regions of bodies that trace the evolution of the Solar system. In the following

section, I discuss the applicability of my F ring model to these other systems.

3.4 **Applicability of this model in collisional systems beyond Saturn's F ring**

The first system I explore is the outer rings of Uranus, the ν and μ rings, first

detected in Hubble Space Telescope (HST) observations in 2003-2005 (Figure 65 is

reproduced from an HST news release with the ν and μ rings labeled as R/2003 U2 and

R/2003 U1, respectively). The ν ring shares some key parameters with the F ring, and the μ

ring contains the embedded moon Mab, which makes both rings places to explore moon

formation. Accretion and fragmentation compete in the "Portia group" (Showalter and

Lissauer 2006, French and Showalter 2011), which is comprised of the material between

Portia (a= 66097 km) and Rosalind (a= 69926 km), known as the ν ring; meanwhile, Portia

continuously perturbs material. Rings exterior to Portia are dynamically unstable on

timescale $\sim 10^6 - 10^8$ years (Duncan and Lissauer 1997, Showalter and Lissauer 2006).

Young rings would resemble the continuously recycling F ring. Further, if the ν ring is due

to a recent moon disruption, there would be a source of small bodies distributed in the ring

that would undergo accretion and fragmentation processes to eventually build aggregates.
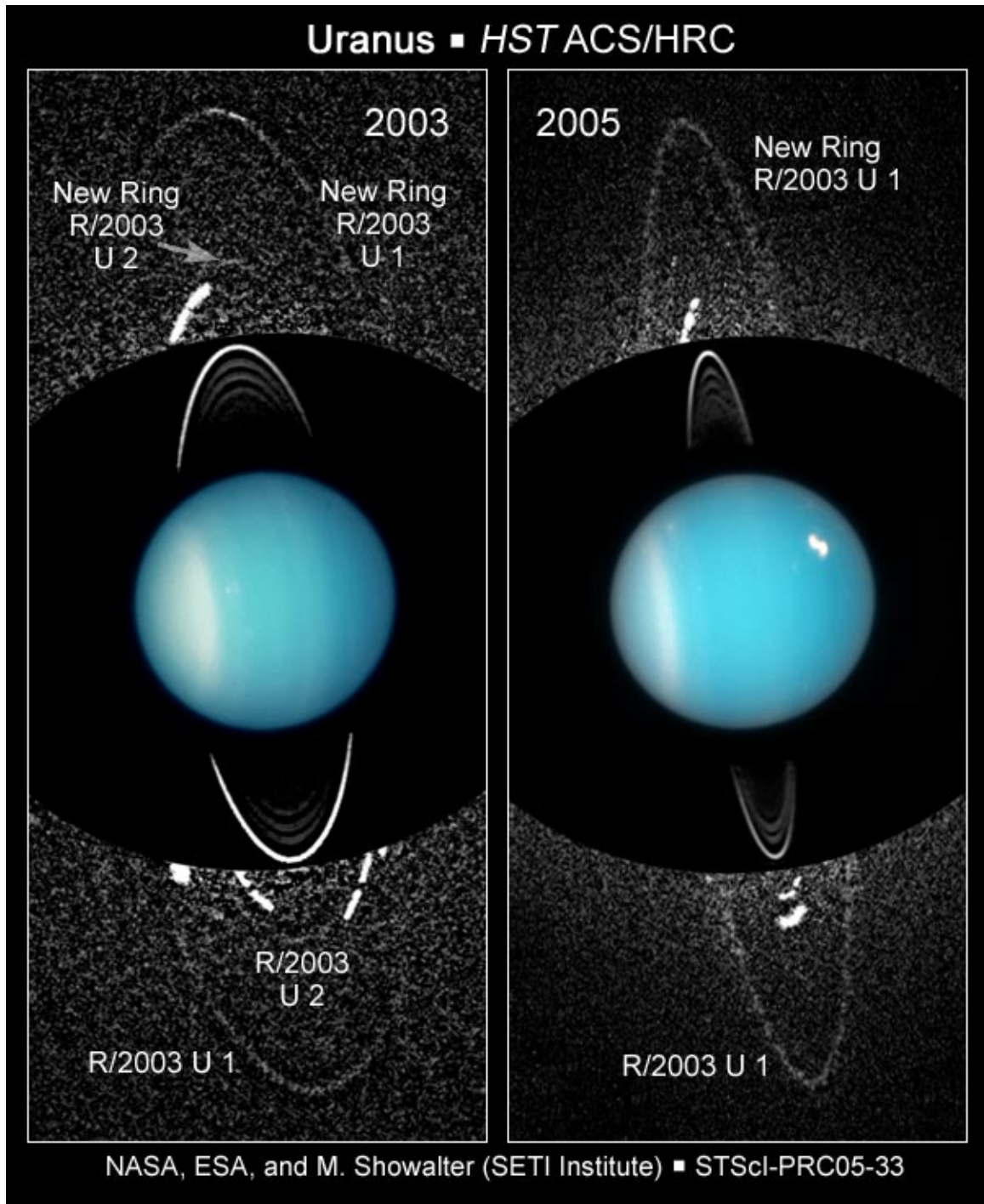
Figure 65. The μ and ν rings of Uranus (R/2003 U1 and U2) in images from 2005. Credit: NASA, ESA, and M. Showalter (SETI Institute).

I model the evolution of the ν ring via binary accretion. Like the F ring, the ν ring is

in the Roche zone ($\mu_{crit,\,inner} \sim 30$ to $\mu_{crit,\,outer} \sim 10^3$, average $\mu_{crit} \sim 225$) where fragmentation

and accretion compete. Unlike the F ring, material in the ν ring has a mass density of
approximately 1.3 g cm^{-3}. Figure 66 shows the resulting distribution of the ring. Moonlet
belts arise at sizes m= 225m$_0$ and m~10^{6}m$_0$. From this distribution, one can predict the
probability of observing moons of certain sizes given the specifics of an observing
campaign as the current observational limit is ~5 km (Showalter and Lissauer 2006). In
turn, this can be a consistency check on the lack of an observed moonlet belt.
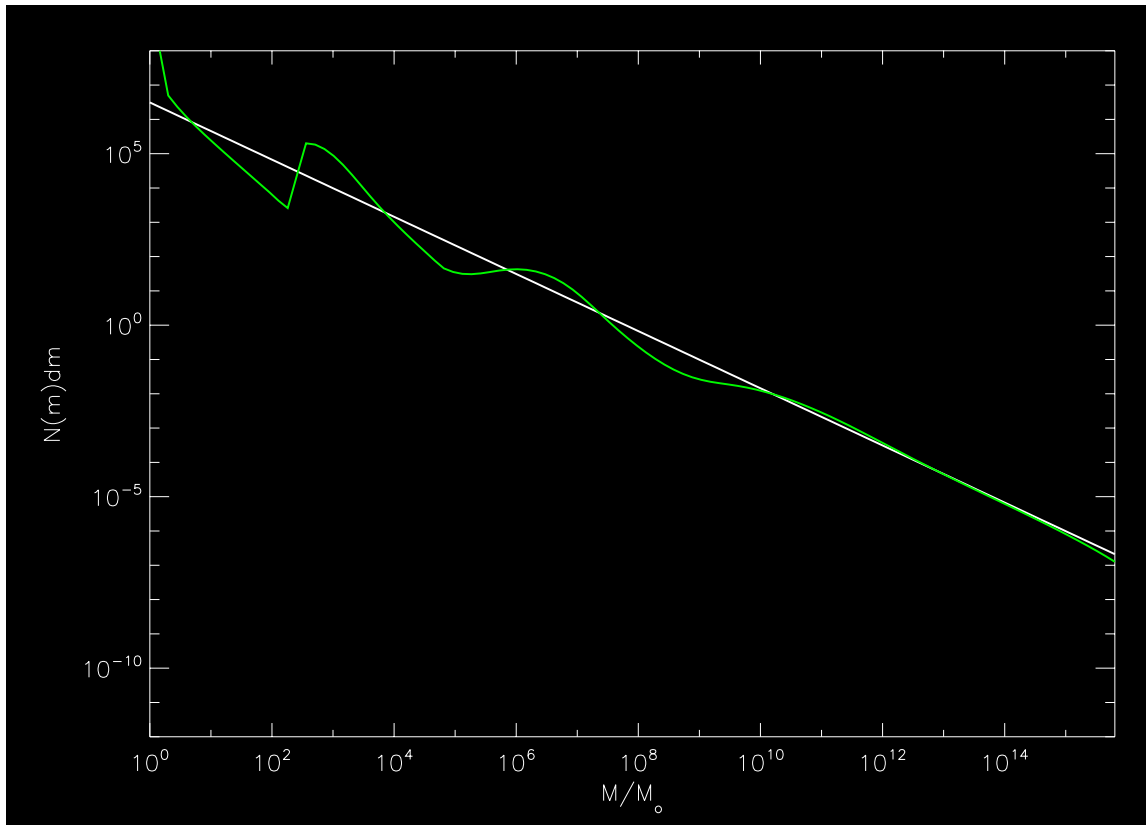
Figure 66. Modeled distribution of the ν ring. Moonlet belts arise at sizes m= 225m$_0$ and
m~10^{6}m$_0$. White continuous power law is the initial distribution of the system, and green
is the quasi-steady state to which it evolves.

The other outer ring I modeled is the μ ring, in which the moon Mab is embedded.
Currently, Mab is speculated to be the largest of an unobserved moonlet belt spanning the
17,000 km width of the ring. Mab's orbit is the center of the μ ring, but, at a$_{\mu\ ring}$= 97736
km, μ$_{crit}$~ 1 (Canup and Esposito 1995). A critical mass ratio of unity should result in all

mass quickly accreting into one body as this ring is well outside Uranus' Roche limit, and

my model is consistent with that prediction (Figure 67). The μ ring appears blue in Keck

observations, which implies it is composed of mostly micron-sized water ice particles

(dePater et al. 2006). The model results, when considered with the composition, semi-

major axis, and width of the ring, suggest that the μ ring has more in common with Saturn's

E ring, where Enceladus is a continuous source of ring particles, than the F ring.
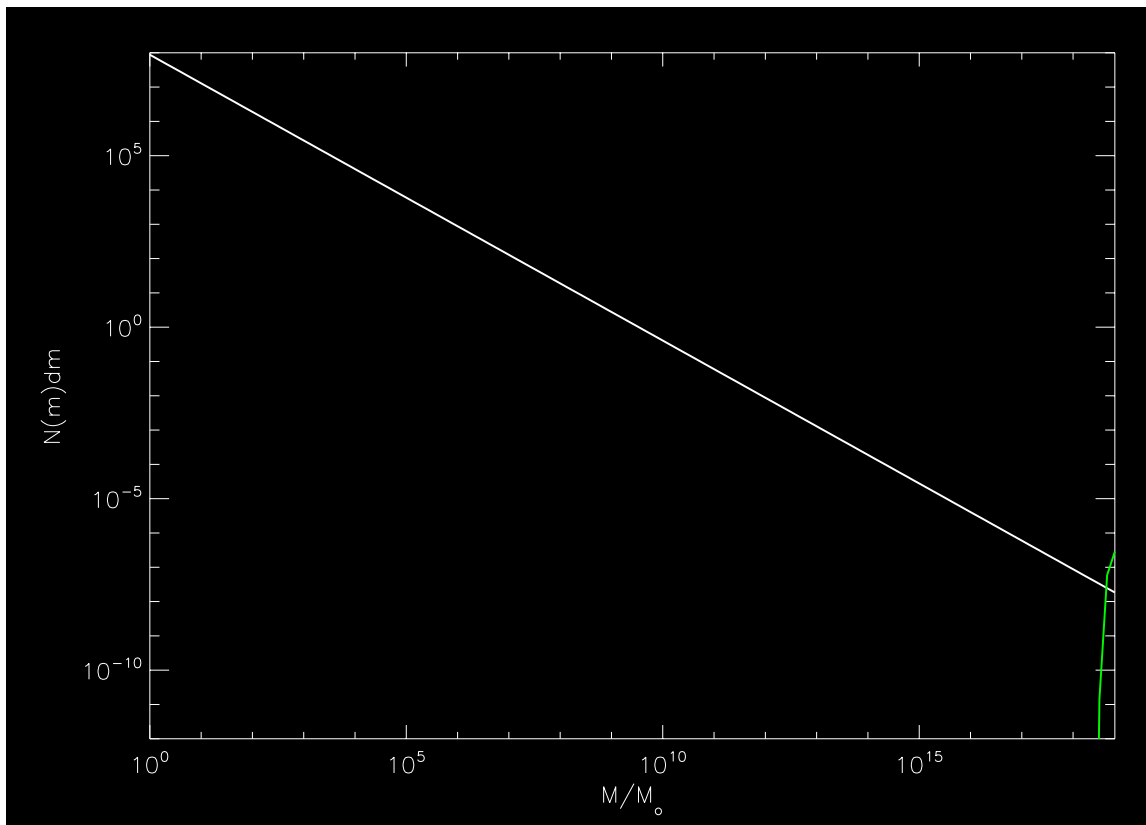
Figure 67. Modeled μ ring, in which the moon Mab is embedded. Ring is far outside
Uranus' Roche limit ($a_{\mu\,ring}$= 97736 km), so μ_{crit}~ 1 (Canup and Esposito 1995). A critical
mass ratio of unity should result in all mass quickly accreting into one body. My model
evolves to a state (green curve) that is consistent with complete accretion into one body
from an initial power law distribution (white).

Many other collisional systems exist, from asteroids to protoplanetary disks. All of

these show a "bump" in their size distributions at ~100 km, which Sheppard and Trujillo

(2010) speculate is due to similar small body reservoirs. Many populations of asteroids

exist: Main Belt, Trojans, and Near Earth Objects. The current size frequency distribution

of Main Belt asteroids shows an excess of bodies at ~100 km relative to a simple power law

(Morbidelli et al 2009, Fig 1; reproduced here as Figure 68). Davis et al (1985) constrain

the early SFD of the Main Asteroid Belt by arguing that Vesta's crust would only have

survived if the asteroid population was only modestly larger than it is today. Further, the

existence of one impact basin on Vesta is consistent with the presence of ~1000 bodies

with D > 35 km (Morbidelli et al 2009) over the last ~4 Gy. Thus, the early SFD was

shallow in the D~100-1000 km range. Morbidelli et al (2009) argue that bodies in the

D~100-1000 km range accreted from sub-kilometer bodies such that there was no

accretion on intermediate scales. Meanwhile, Weidenschilling (2011) argues bodies <100

m accrete to the current SFD and the "bump" at ~100 km is due to a transition from

dispersion-dominated runaway growth to a Keplerian-shear-dominated regime. Thus, the

asteroid community seeks to resolve whether asteroid were "born big" or "born small."

Also, Ormel et al (2010 a,b) define three stages of accretional growth based on collisional

velocities: super escape ($\frac{dM}{dt} \propto M^{2/3}$), dispersion-dominated ($\frac{dM}{dt} \propto M^{4/3}$), and shear-

dominated ($\frac{dM}{dt} \propto M$). As discussed in my assessment of the multimodal distribution

(Section 3.1.3), Each of these hypotheses for the evolution of the asteroid belt distribution

contains sharp thresholds in the physics of the system. My model can be used to predict

how each of these affects the current distribution and resolve which mechanisms were

most important in its evolution.
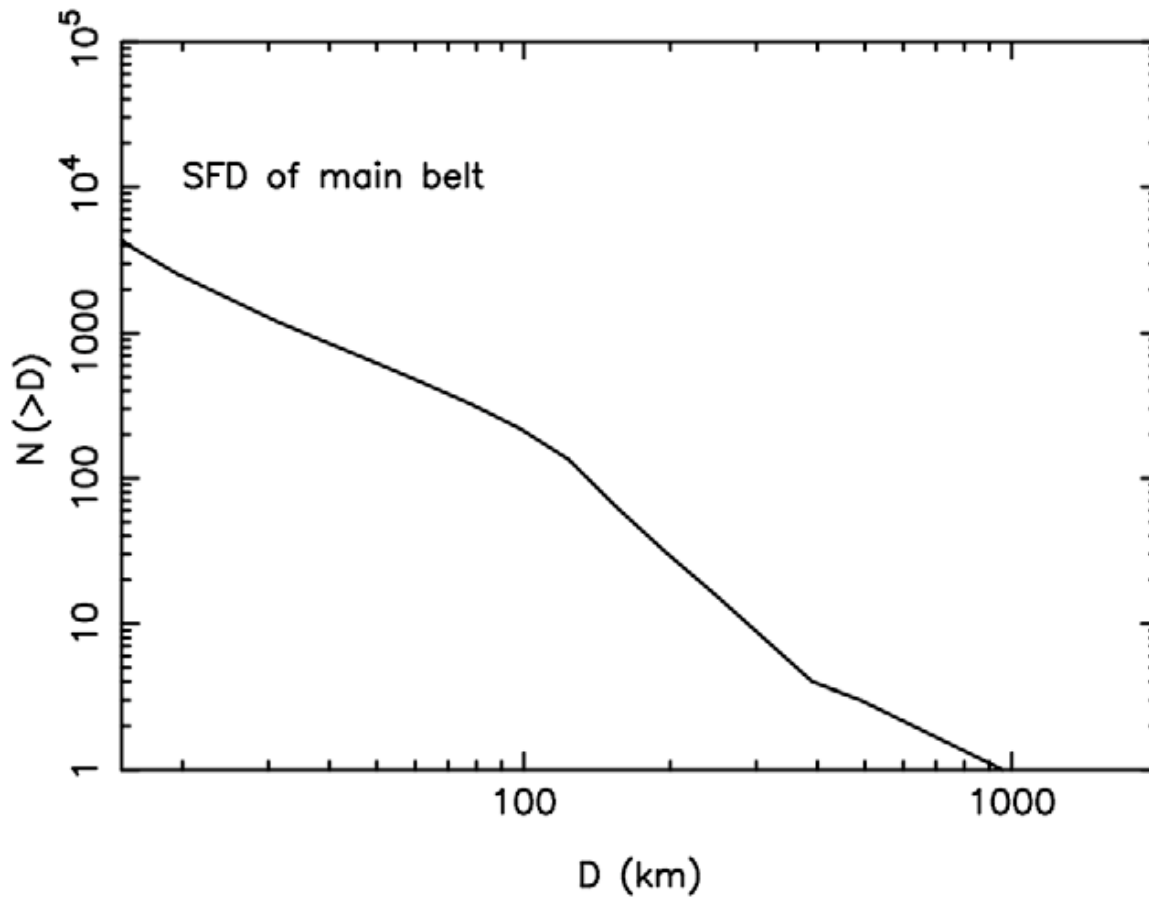
Figure 68. From Morbidelli et al (2009), Figure 1. "The size-frequency distribution (SFD) of main belt asteroids for D > 15 km, assuming, for simplicity, an albedo of p_v =1/4 0:092 for all asteroids. According to Jedicke et al. (2002), D > 15 km is a conservative limit for observational completeness." An excess or "bump" occurs at D~100 km.

The observed mass distribution of the Kuiper belt is $N(R) \propto R^{-4.8\pm0.3}$ for the largest

KBOs (Fraser and Kavelaars 2009, Fuentes and Holman 2008, Bernstein et al. 2004). The

power law index is smaller for smaller, collisionally-dominated KBOs, but the overall SFD is

continuous rather than bimodal. Ormel et al. (2010b) use the SFD shape to rule out

oligarchic growth as a plausible growth mechanism in the Kuiper belt. Application of my

model to the Kuiper belt would be inappropriate because the bodies in the Kuiper belt do

not appear to be completely collisionally evolved.

Another astrophysical collisional system is a protoplanetary disk. This is a burgeoning field rich with opportunities to model accretion and fragmentation. Evolution of protoplanetary bodies provides insight into primordial populations in our own Solar system, including the asteroid belt and Kuiper belt. Protoplanetary disks are systems with some very different conditions than the F ring. They include large quantities of gas, magnetic fields, and radiative heating, all of which do not play a significant role in the F ring's evolution. After early attempts to model protoplanetary disks, the scientific community encountered issues similar to my attempts to match the observations. As I have included a production term to change the overall shape of the distribution, so did the protoplanetary disk modelers introduce other physical mechanisms to boost localized accretion of bodies to build planetary cores quickly enough. Among mechanisms introduced is turbulence, like magneto-rotational instabilities (Balbus and Hawley, 1998), which allows small particles to concentrate in overdense regions. Eventually, oligarchy supersedes runaway growth in these isolated regions for bodies larger than some threshold size (Ormel et al 2010a). This then allows planetesimals to grow to planet-sized bodies. Thus, both protoplanetary disks and the F ring require the addition of a production term. Few systems can be realistically described using a simple binary-accretion model.

In conclusion, the Main Asteroid Belt is a collisionally-evolved system. My model could help resolve the current debate of whether we are we observing the post-accretion population or a primordial one. The Kuiper Belt is primordial, not collisionally-evolved enough for my model to apply. The protoplanetary disk community has been stymied by a lack of quick accretion in basic models. The problem in these models is basically the same as in my model without a production term. Plausible physical mechanisms employed to

increase accretion of objects >1 m include turbulence, magneto-rotational instabilities, and gravitational collapse. Addition of a production term is needed for both systems because few systems can be realistically described using a simple binary-collision accretion model. The expansion of my model using a production term could expand the applicability of the model to other systems like protoplanetary disks.

4. Discussion

Saturn's F ring is a key natural laboratory for observations of accretion and disruption processes. The ring contains transient phenomena such as clumps, azimuthal asymmetries, and moon-induced structure. The F ring is located in an ideal location for direct observation, of which researchers have taken advantage over the last three decades. The wealth of observations allows modelers to develop more sophisticated models of the ring to constrain the physical processes affecting the system. This dissertation investigates accretion and disruption. It is motivated by observations of the F ring and complemented with a model. Then the model is adjusted to be consistent with the observations. Finally, I apply the model to another ring system and suggest where it could have further applications.

Stellar occultations show features in Saturn's F ring that indicate azimuthally-elongated clumping of ring material. Classification of such significant features demonstrates that while clumping may be a common process, consolidation into an opaque object, like a Moonlet, is not. The location of clumps is correlated to their relative distance from Prometheus, indicating that perturbations from Prometheus may stimulate clumping.

Because the F ring is in the Roche zone where accretion and fragmentation compete, I use a binary collision model to numerically track the evolution of the size distribution of bodies in the F ring as they collide. A multimodal distribution results, the general trend of which follows the Dohnanyi-predicted $q=11/6$ power law for a collisionally-evolved system. Upon investigation, I discovered the separation of successive modes is dependent on the critical mass ratio of colliding bodies that determines whether a collision results in complete accretion or fragmentation. Examination of similar previous models revealed

168

that multimodal distributions are ubiquitous for modeled collisional systems. The BE02 results shows that the trough in the BE02 quasi-equilibrium distribution (Figure 22) occurs where $m/m_0 = \mu_{crit}$. Fraser (2009) derives an analytic expression for the size at which a "divot" occurs in his modeled distribution of the Kuiper belt, which is dependent on the energy threshold for disruption and the strength parameters of colliding material. Campo Bagatin et al. (1994) report a "wavy pattern" that they argue is caused by a small-size cutoff of their distribution. This dissertation is the first work that carefully investigates and characterizes the multimodal behavior. Further, this dissertation argues that sharp physical thresholds are responsible for the multimodal behavior, which is why it is seen in different systems and has been linked to multiple physical mechanisms.

The binary accretion model of the F ring does not reproduce the UVIS-observed distribution of clumps. Upon focused study of the inconsistency, the principal way to match the power-law slope of the model result to the shallow slope of the observed distribution is to increase the accretion coefficient of the coagulation equation by a factor of 1000. No plausible physical mechanisms or combination thereof support this best-fit model, however. Gravitational focusing and Hill radii do not increase the accretion anywhere near a thousand-fold. Furthermore, while consistent with UVIS observations, it is inconsistent with Imaging results. If there was, in fact, a mode at $m/m_0 = 10^9$ (corresponds to r~few km), then ISS would have seen many moonlets because this size is above their detection threshold. To create a physically-plausible model that is consistent with observations, we must include an additional term that specifically accounts for the production of large bodies

One physically-plausible mechanism that allows for the increase in the number of large bodies and thus the "flattening" of the modeled distribution's slope is an enhanced growth region. In this scenario, the largest bodies in the system experience increased accretion in the high-density regions created by Prometheus because gravitational instabilities form around them. The numbers of the smallest bodies decrease as the larger bodies sweep them up. This "flattens" the distribution by preferentially removing small bodies. Thus, the significant features that UVIS sees may themselves be swept up by even larger moonlets (e.g. S/2004 S 6).

Additionally, I expand the binary accretion model to account for compaction of clumps; thus, I allow the model to evolve in size and density. The result is that bodies size-segregate by porosity. That is to say, the largest bodies are the densest and the smallest are the most porous. This is consistent with the observations reported in Section 2: solid Moonlets are an order of magnitude less abundant than loosely-bound Icicles. Upon examination of each density state independently I find that each has a multimodal shape, and when coadded by size ($n(r)$ over all densities), I recover the same distribution as from the constant density model, $n(m,t)$ (Figure 63). Consequently, modeling the distribution of F ring clumps by allowing for compaction does not match the observed distribution. Thus, the effect of enhanced accretion in a high-density region is the only method yet tested that results in a model consistent with observations. Allowing the model to vary in density and size opens up a wide range of applications. With different physics governing the collisional outcomes for different density states, one can use this model to predict the probability of creating a solid, coherent object like a moon. Further, one might introduce a high-density seed to the model in order to stimulate growth. In this way, this expansion can be used for

170

other systems of bodies where compaction is also important, such as asteroids and planetesimals.

Studies of ring systems in our Solar system can provide insight into other astrophysical disks, both far away and long ago. For example, the number of extrasolar planets observed has grown from a handful to over 700 in the last decade (Schneider 2011). A large fraction of those planets are gas or ice giants that may host ring systems. Furthermore, observations of the protoplanetary disks from which they form are of increasing resolution and number. Synergy among these studies of flattened orbital systems can tell us about moon and planet formation, collisional fragmentation, disk structures, and the like. This in turn can tell us about the history of our own Solar system.

Bibliography

Acuna, M. H., and Ness, N.F., 1976. The main magnetic field of Jupiter, J. Geophys Res., 81, 2917-2922.

Albers, N. et al., 2009. Classifying Saturn's F ring strands. DPS meeting #41, #22.05.

Albers, N., et al., 2012. Saturn's F Ring as seen by Cassini UVIS: Kinematics and Statistics. Icarus, in press.

Balbus, S. A., & Hawley, J. F. 1998, RMP, 70, 1.

Barbara, J. and Esposito, L.W., 2002. Moonlet Collisions and the Effects of Tidally Modified Accretion in Saturn's F Ring. Icarus 160, 161-171.

Beurle, K., et al., 2010. Direct evidence for gravitational instability and moonlet formation in Saturn's rings. ApJL 718, L176-L180.

Bernstein, G. M.; Trilling, D. E.; Allen, R. L.; Brown, K. E.; Holman, M.; Malhotra, R. 2004. The size distribution of transneptunian bodies. AJ 128, 1364–1390.

Bosh, A.S. & Rivkin, A.S., 1996. Observations of Saturn's inner satellites during the May 1995 ring-plane crossing. Science 272, 518-521.

Bosh, A. S., Olkin, C.B., French, R.G., and Nicholson, P.D., 2002. Saturn's F ring: Kinematics and particle sizes from stellar occultation studies, Icarus 157, 57-75.

Brophy, T.G., Stewart, G.R., Esposito, L.W., 1990. A phase-space fluid simulation of a two-component narrow planetary ring: particle size segregation, edge formation, and spreading rates. Icarus 83, 133-155.

Brown, R. H., et al., 2003. Observations with the Visual and Infrared Mapping Spectrometer (VIMS) during Cassini's Flyby of Jupiter. Icarus 164, 461–470.

Burns, J. A., Schafer, L.E., Greenberg, R. J., and Showalter, M. R., 1985. Lorentz resonances and the structure of the Jovian ring, Nature 316, 115-119.

Burns, J. A., M. R. Showalter, D. P. Hamilton, P. D. Nicholson, I. de Pater, M. E. Ockert Bell, and P. C. Thomas, 1999. The formation of Jupiter's faint rings, Science, 284, 1146-1150.

Burns, J. A., D. P. Simonelli, M. R. Showalter, D. P. Hamilton, C. D. Porco, H. Throop, and L. W. Esposito, 2004. Jupiter's ring-moon system, in Jupiter: The Planet, Satellites and Magnetosphere, edited by Bagenal, F., Dowling, T. E., & McKinnon, W. B., 241-262, Cambridge Univ. Press, Cambridge.

Campo Bagatin, et al., 1994. Wavy size distributions for collisional systems with a small-size cutoff. Planet. Space Sci. 42, 1079-1092.

Canup, R. and Esposito, L.W., 1995. Accretion in the Roche zone: Coexistence of rings and ringmoons. Icarus 113, 331-352.

Ceplecha, Z., 1992. Influx of interplanetary bodies onto Earth. AA 263, 361-366.

Chapman, C. R., Merline, W. J. & Thomas, P., 1999. Cratering on Mathilde. Icarus 140, 28-33.

Charnoz, S. et al., 2005. Cassini discovers a kinematic spiral ring around Saturn. Science 310, 1300-1304.

Charnoz, S. et al., 2007. The Equatorial Ridges of Pan and Atlas: Terminal Accretionary Ornaments? Science 318, 1622–1624.

Charnoz, S., 2009. Physical collisions of moonlets and clumps with the Saturn's F ring core. Icarus 201, 1101-197.

Charnoz, S., et al., 2009. Origin and evolution of Saturn's ring system, in Saturn from Cassini-Huygens, edited by M. Dougherty, L. Esposito, and S. M. Krimigis, pp. 537-575, Springer-Verlag, Dordrecht.

Colombo, G., Goldreich, P., and Harris, A.W., 1976. Spiral structure as an explanation for the asymmetric brightness of Saturn's A ring, Nature 264, 344-345.

Colwell, J.E. et al., 1990. Voyager photopolarimeter observations of uranian ring occultations. Icarus 83, 102-127.

Colwell, J.E., Esposito, L.W., Sremcevic, M., 2006. Gravitational wakes in Saturn's A ring measiured by stellar occulations from Cassini. Geophys. Rev. Lett. 33. L07201.

Colwell, J.E. et al., 2007. Self-gravity wakes and radial structure of Saturn's B ring. Icarus 190, 127-144.

Colwell, J. E., et al., 2009. The structure of Saturn's rings, in Saturn from Cassini Huygens, edited by M. Dougherty, L. Esposito, and S. M. Krimigis, pp. 375 412, Springer-Verlag, Dordrecht.

Colwell, et al., 2010. Cassini UVIS Stellar Occultation Observations of Saturn's Rings. AJ 140, 1569-1578.

Cuzzi, J. N. & Scargle, J.D., 1985. Wavy edges suggest moonlet in Encke's gap, ApJ 292, 276-290.

Cuzzi, J.N. & Burns, J.A., 1988. Charged particle depletion surrounding Saturn's F
        ring: Evidence for a moonlet belt? Icarus 74, 284-324.

Cuzzi, J., R., et al., 2009. Ring particle composition and size distribution, in Saturn
        from Cassini-Huygens, edited by M. Dougherty, L. Esposito, and S. M.
        Krimigis, pp. 459{509, Springer-Verlag, Dordrecht.

Cuzzi, J. N., et al., 2010. An evolving view of Saturn's dynamic rings, Science 327,
        1470-1475.

Davis, D., 1999. The Collisional History of Asteroid 253 Mathilde. Icarus 140, 49-52.

Davis, D., Farinella, P., & Weidenschilling, S., 1999. Accretion of a massive
        Edgeworth-Kuiper belt. LPSC XXX.

Davis, D. R., Chapman, C. R., Weidenschilling, S. J. and Greenberg,
        R., 1985. Collisional history of asteroids : evidence from Vesta and the Hirayama
        families. Icarus 62,30-53.

de Pater, I., et al., 1999. Keck Infrared Observations of Jupiter's Ring System near
        Earth's 1997 Ring Plane Crossing. Icarus 138, 214–223.

dePater, I., Hammel, H. B., Gibbard, S. G., Showalter, M. R., 2006.
        New Dust Belts of Uranus: One Ring, Two Ring, Red Ring, Blue Ring. Science 312,
        92–94.

de Pater, I., Gibbard, S.G., Lebofsky, Hammel, H.B., 2006. Evolution of the dusty rings
        of Uranus. Icarus 180, 186–200.

Dohnanyi, J. W., 1969. Collisional model of asteroids and their debris. JGR 74, 2531-
        2554.

Drake, S. Galileo at Work: His Scientific Biography. Chicago, IL: New York: Dover,
        1995.

Duncan, M. & Lissauer, J., 1997. Orbital Stability of the Uranian Satellite System.
        Icarus 125, 1-12.

Elliot, J.L., Dunham, E., Mink, D., 1977. The Occultation of SAO – 15 86687 by the
        Uranian Satellite Belt. IAU, Circular No. 3051.

Elliot, J.L., Dunham, E., and Mink, D., 1977. The rings of Uranus. Nature 267, 328
        330.

Esposito, L. W., 2010. Composition, structure, dynamics, and evolution of Saturn's

rings, Ann. Rev. Earth Planet. Sci., 38, 383-410.

Esposito, L. W., Brahic, A., Burns, J. A., and Marouf, E. A., 1991. Particle properties and processes in Uranus' rings, in Uranus, edited by J. T. Bergstralh, E. D. Miner, and M. S. Matthews, pp. 410-465, Univ. Arizona Press, Tucson.

Esposito, L.W., Colwell, J.E., McClintock, W.E., 1998. Cassini UVIS observations of Saturn's rings. Planet. Space Sci. 46, 1221-1235.

Esposito, L. W., 2002. "Planetary rings". Reports on Progress in Physics 65, 1741–1783.

Esposito, L.W. et al., 2004. The Cassini Ultraviolet Imaging Spectrograph investigation. Space Sci. Rev.. 115, 294-361.

Esposito, L.W. et al., 2005. Ultra-violet imaging spectroscopy shows an active Saturn system. Science 307, 1271-1275.

Esposito, L.W. et al., 2008. Moonlets and clumps in Saturn's F ring. Icarus 194, 278-289.

Esposito, L.W. et al., 2012. A predator-prey model for moon-triggered clumping in Saturn's rings. Icarus 217, 103-114.

Fillius, R. W., McIlwain, C.E., and Mogro-Campero, A., 1975. Radiation belts of Jupiter: A second look, Science, 188, 465-467.

Fraser, W. & Kavelaars, J., 2009. The size distribution of Kuiper belt objects for D≥10 km. Astron. J 137, 72-82.

French, R., et al., 2003. Saturn's wayward shepherds: the peregrinations of Prometheus and Pandora. Icarus 162, 143-170.

French, R., et al., 2006. Ring Orbits from Multiple Occultation Observations. In Bulletin of the American Astronomical Society, Volume 38, 559.

French, R. G., Nicholson, P.D., Porco, C.C., and Marouf, E.A., 1991. Dynamics and structure of the Uranian rings, in Uranus, edited by J. T. Bergstralh, E. D. Miner, and M. S. Matthews, pp. 327-409, Univ. Arizona Press, Tucson.

French, R. & Showalter, M., 2011. Cupid is Doomed: An Analysis of the Stability of the Inner Uranian Satellites. AAS, DDA 42, #6.02; BAAS 43.

Fuentes, C. & Holman, M., 2008. A Subaru archival search for faint trans-Neptunian objects. Astron. J 136, 83-97.

Gehrels, T. et al., 1980. Imaging photopolarimeter on Pioneer Saturn. Science 207, 434-439.

Hansen, C.J. et al., 2006. Enceladus' Water Vapor Plume. Science 311,1422 – 1427.

Hedman, M.M. et al., 2007. Self-gravity wake structures in Saturn's A ring revealed by Cassini-VIMS. Astron. J. 133, 2624-2629.

Hedman, M. M., et al. , 2010a. The architecture of the Cassini Division, AJ, 139, 228 251.

Hedman, M. M., Nicholson, P.D., Showalter, M.R., and Cassini VIMS Team, 2010b. Spectroscopic identifcation of clumps in the F ring, AAS DPS Meeting Abstracts, 42, 22.01.

Hedman, M.M., et al., 2011. The Christiansen Effect in Saturn's narrow dusty rings and the spectral identification of clumps in the F ring. Icarus 215, 695-711.

Hog et al., 2000. Letter to the Editor - The Tycho-2 catalogue of the 2.5 million brightest stars. AA 363, 385.

Horanyi, M., et al., 2009. Diffuse Rings, in Saturn from Cassini-Huygens, edited by M. Dougherty, L. Esposito, and S. M. Krimigis, pp. 511-536, Springer-Verlag, Dordrecht.

Housen, K., Holsapple, K., & Voss, M., 1999. Compaction as the origin of the unusual craters on the asteroid Mathilde. Nature 402, 155-157.

Jedicke, R., Larsen, J., Spahr, T., 2002. Observational selection effects in asteroid surveys. Asteroids III, 71–87.

Karjalainen R and Salo H.. 2004. Gravitational accretion of particles in Saturn's rings. Icarus 172, 328-48.

Karkoshka, E., 1997. Rings and Satellites of Uranus: Colorful and Not So Dark. Icarus 125, 348–363.

Kolvoord, R.A., Burns, J.A., Showalter, M.R., 1990. Periodic features in Saturn's F ring - Evidence for nearby moonlets. Nature 345, 695-697.

Krivov, A.V., et al., 2005. Evolution of a Keplerian disk of colliding and fragmenting particles: a kinetic model with application to the Edgeworth Kuiper belt. Icarus 174, 105-134.

Lane, A.L. et al., 1982. Photopolaritmetry from Voyager 2: Preliminary results on Saturn, Titan, and the rings. Science 215, 537-543.

Lewis, M.C. & Stewart, G.R., 2009. Features around embedded moonlets in Saturn's rings: The role of self-gravity and particle size distributions. Icarus 199, 387-412.

Longaretti, P-Y., 1989. Saturn's main ring particle size distribution - an analytic approach. Icarus 81, 51-73.

Love, S.G., Hoerz, F., & Brownlee, D.E., 1993. Target Porosity Effects in Impact Cratering and Collisional Disruption. Icarus 105, 216-224.

Meier, R., et al., 1999. Near Infrared Photometry of the Jovian Ring and Adrastea. Icarus **141**, 253–262.

Meinke, et al. 2012. Classification of F ring features observed in Cassini UVIS occultations. Icarus 218, 545-554.

Millis, R.L., Wasserman, L.H., Birch, P.V., 1977. Detection of rings around Uranus. Nature 267, 330-331.

Miner, E. D., Wessen, R.R., Cuzzi, J. N., 2007. The discovery of the Neptune ring system. Planetary Ring Systems. Springer Praxis Books.

Morbidelli, A., et al., 2009. Asteroids were born big. Icarus 204, 558-573.

Murray, C.D., 1992. Wandering on a leash. Nature 357, 542-543.

Murray, C.D., Gordon, M.K., Giuliatti-Winter, S.M., 1997. Unraveling the strands of Saturn's F ring. Icarus 129, 304-316.

Murray, C. D., and Dermott, S.F., 1999. Solar System Dynamics, Cambridge Univ. Press, Cambridge.

Murray, C.D. et al., 2005. How Prometheus creates structure in Saturn's F ring. Nature 437, 1326-1329.

Murray, C.D., 2007. Saturn's dynamical rings. Phys. Today 60, 74.

Murray, C.D. et al., 2008. The determination of the structure of Saturn's F ring by nearby moonlets. Nature 453, 739-744.

Namouni, F. & Porco, C.C., 2002. The confinement of Neptune's ring arcs by the moon Galatea, Nature 417, 45-47.

NASA's Hubble Discovers New Rings and Moons Around Uranus. News Release Number: STScI-2005-33, 22 Dec. 2005.

Nicholson, P.D., et al., 1996. Observations of Saturn's ring-plane crossing in August and November. Science 272, 509-516.

Nicholson, P. D. & Hedman, M.M., 2010. Self-gravity wake parameters in Saturn's A and B rings, Icarus, 206, 410-423.

Null, G.W., et al., 1980. Saturn gravity results obtained from Pioneer Saturn spacecraft tracking data and earth-based Saturn satellite data. BAAS 12, 742.

Ockert, M. E., Cuzzi, J.N., Porco, C.C., and Johnson, T.V., 1987. Uranian ring photometry: Results from Voyager 2. Journal of Geophysical Research 92, 969–78.

Ockert-Bell, M. E., et al., 1999. The Structure of Jupiter's Ring System as Revealed by the Galileo Imaging Experiment. Icarus 138,188–213.

Ohtsuki, K. 1993. Capture probability of colliding planetesimals: Dynamical constraints on accretion of planets, satellites, and ring particles. Icarus 106, 228–246.

O'Keefe, J.A., 1976. Tektites and Their Origin. Elsevier.

Öpik, E.J., 1951. Collision probabilities with the planets and the distribution of interplanetary matter. Proc. Roy. Irish Acad. 54, 165–199.

Ormel, C.W., Dullemond, C.P., & Spaans, M., 2010. Accretion among preplanetary bodies: The many faces of runaway growth. Icarus 210, 507-538.

Ormel, C.W., Dullemond, C.P., & Spaans, M., 2010. A new condition for the transition from runaway to oligarchic growth. ApJL 714, L103-L107.

Owen, T., G. E. Danielson, A. F. Cook, C. Hansen, V. L. Hall, and T. C. Duxbury, 1979. Jupiter's rings, Nature 281, 442-446.

Paddack, S.J., 1969. Rotational bursting of small celestial bodies: Effects of radiation pressure, J. Geophys. Res. 74, 4379–4381.

Porco, C.C., 1991. An Explanation for Neptune's Ring Arcs. Science 253, 995–1001.

Porco, C.C., et al., 1995. Neptune's ring system, in Neptune and Triton, edited by D. P. Cruikshank, pp. 703{804, Univ. Arizona Press, Tucson.

Porco, C.C., et al., 2004. Cassini Imaging Science: Instrument Characteristics and Anticipated Scientific Investigations At Saturn. SSR 115, 363-497.

Porco, C.C., et al., 2005. Cassini Imaging Science: Initial results on Saturn's rings and

small satellites. Science 307, 1226-1236.

Porco, C.C., et al., 2007. Saturn's Small Inner Satellites: Clues to Their Origins. Science 318, 1602–1607.

Poulet, F. et al., 2000. Saturn's Ring Plane Crossings of August and November 1995: A Model for the New F-Ring Objects. Icarus 144, 135-148.

Poynting, J. H., 1903. Radiation in the solar system: its Effect on Temperature and its Pressure on Small Bodies. MNRAS 64, A1–A5.

Robertson, H.P., 1937. Dynamical effects of radiation in the solar system. MNRAS 97, 423–438.

Robbins, S.J., et al., 2010. Estimating the masses of Saturn's A and B rings from high optical depth N-body simulations and stellar occultations. Icarus 206, 431-445.

Radzievskii, V. V., 1954. A mechanism for the disintegration of asteroids and   meteorites. Doklady Akademii Nauk SSSR 97, 49–52.

Salo, H., 1995. Simulations of dense planetary rings. III. Self-gravitating identical particles. Icarus 117, 287-312.

Salo, H. & Hanninen, J., 1998. Neptune's Partial Rings: Action of Galatea on Self Gravitating Arc Particles. Science 282, 1102–1104.

Salo, H and Schmidt, J. 2010. N-body simulations of viscous instability of planetary rings. Icarus 206, 390-409.

Schmidt, J., et al., 2009. Dynamics of Saturn's Dense Rings, in Saturn from Cassini Huygens, edited by M. Dougherty, L. Esposito, and S. M. Krimigis, pp. 413-458, Springer-Verlag, Dordrecht.

Schneider, Jean (10 September 2011). "Interactive Extra-solar Planets Catalog". The Extrasolar Planets Encyclopedia. Retrieved 2012-01-04.

Seiβ, M., Spahn, F., Sremcevic, M., and Salo, H., 2005. Structures induced by small moonlets in Saturn's rings: Implications for the Cassini mission, Geophys. Res. Lett. 32, L11, 205.

Sheppard, S.S. & Trujillo, C.A., 2010. The size distribution of the Neptune Trojans and the missing intermediate-sized planetesimals. ApJL 723, L233-L237.

Showalter, M. R., Cuzzi, J.N., Marouf, E. A., and Esposito, L. W., 1986. Satellite wakes and the orbit of the Encke Gap moonlet, Icarus, 66, 297-323.

Showalter, M. R., Burns, J. A., Cuzzi, J. N., & Pollack, J.B., 1987. Jupiter's Ring System: New Results on Structure and Particle Properties. Icarus 69, 458–498.

Showalter, M. R., 1991. Visual detection of 1981S13, Saturn's eighteenth satellite, and its role in the Encke gap, Nature 351, 709-713.

Showalter, M.R., 1998. Detection of Centimeter-Sized Meteoroid Impact Events in Saturn's F Ring. Science 282, 1099.

Showalter, M.R., 2004. Disentangling Saturn's F ring. I. Clump orbits and lifetimes. Icarus 171, 356-371.

Showalter, M.R. & Lissauer, J.J., 2006. The Second Ring-Moon System of Uranus: Discovery and Dynamics. Science 311, 973–977.

Showalter, M. R., et al., 2007. Clump Detections and Limits on Moons in Jupiter's Ring System. Science 318, 232–234.

Shu, F.H., Stewart, G.R., 1985. The collisional dynamics of particulate disks. Icarus 62, 360-383.

Silk and Takahashi. 1979. A statistical model for the initial stellar mass function. ApJ 229. 242-256.

Smith, B. A. et al., 1981. Encounter with Saturn - Voyager 1 imaging science results. Science 212, 163-1101.

Smith, B. A. et al., 1982. A new look at the Saturn system - The Voyager 2 images. Science 215, 504-537.

Smith, B. A., 1986. Satellites and Rings of Uranus. IAU Circular 4168.

Smith, B. A., et al.,1986. Voyager 2 in the Uranian System: Imaging Science Results. Science 233, 97–102.

Smith, B. A., et al., 1989. Voyager 2 at Neptune: Imaging Science Results. Science 246, 1422–1449.

Smoluchowski, M.V., 1916. Drei Vortrage uber Diffusion, Brownsche Bewegung und Koagulation von Kolloidteilchen. Z. Phys. 17, 557-585.

Spahn, F. & Sremcevic, M., 2000. Density patterns induced by small moonlets in Saturn's rings? A&A, 358, 368-372.

Spahn, F., Albers, N., Sremcevic, M., Thornton, C., 2004. Kinetic description of coagulation and fragmentation in dilute granular particle ensembles Europhys.

Lett. 67, 545–551.

Spitale, J. N., and C. C. Porco, 2010. Detection of free unstable modes and massive bodies in Saturn's outer B ring, AJ, 140, 1747-1757.

Sremcevic, M., Spahn, F., and Duschl, W.J., 2002. Density structures in perturbed thin cold discs. MNRAS 337, 1139-1152.

Sremcevic, M., et al., 2007. A belt of moonlets in Saturn's A ring, Nature 449, 1019-1021.

Stewart, S.T. & Ahrens, T.J., 1999. Porosity Effects on Impact Processes in Solar System Materials. LPSC XXX. Abs 2020.

Tanaka, H., Inaba, S., & Nakazawa, K., 1996. Steady-state size distribution for the self-similar collision cascade. Icarus 123, 450-455.

Taylor, J., 1997. Introduction to Error Analysis. University Science Bookes. Appendix C.

Tiscareno, M. S., et al., 2006. 100-metre-diameter moonlets in Saturn's A Ring from observations of propeller structures, Nature 440, 648-650.

Tiscareno, M. S., et al., 2007. Cassini imaging of Saturn's rings II. A wavelet technique for analysis of density waves and other radial structure in the rings, Icarus 189, 14-34.

Tiscareno, M.S. et al., 2008. The Population of propellers in Saturn's A ring. Astron. J. 135, 1083-10101.

Tiscareno, et al., 2010. Physical Characteristics and Non-Keplerian Orbital Motion of "Propeller" Moons Embedded in Saturn's Rings. ApJ 718, L92-L96.

Veverka, J. et al., 1997. NEAR's flyby of 253 Mathilde: Images of a C asteroid. Science 278, 2109-2112.

Veverka, J. et al., 1999. NEAR Encounter with asteroid 253 Mathilde: Overview. Icarus 140, 3-16.

Weidenschilling, S.J., 2011. Initial sizes of planetesimals and accretion of the asteroids. Icarus 214, 671-684.

West, R., et al., 2010. In-flight calibration of the Cassini imaging science sub-system cameras. Planet. Space Sci.

Zacharias et al., 2004. The Second US Naval Observatory CCD Astrograph Catalog

(UCAC2). ApJ 127, 3043-3059.